IDENTIFYING POTENTIAL COLLAPSE FEATURES UNDER HIGHWAYS

by

Wolfe, P. J. (Principal Investigator),

Hauser, E. C. (Co-Principal Investigator),

and Richard, B. H. (Original Principal Investigator)

Department of Geological Sciences, Wright State University

Additional Contributors

Hick, J. and Greer, M., Wright State University

Luke, B. A., University of Nevada Las Vegas

Zoghi, M., University of Dayton

Prepared in cooperation with the Ohio Department of Transportation and
the U.S. Department of Transportation, Federal Highway Administration

ACKNOWLEDGEMENTS

The authors would like to express our appreciation to Wright State University student Steve Roberts and University of Nevada Las Vegas student Burcin Avar for their efforts. The authors thank the Ohio Department of Transportation, particularly Mr. Rick Ruegsegger, for support of this work by suggestions, providing maps and information, site visits, and discussions. We thank Dr. Doug Green of the Department of Geological Sciences of Ohio University for loaning us resistivity equipment.

Table of Contents

List of Figures

List of Tables

I. INTRODUCTION

In 1994, subsidence features were identified on Interstate 70 in eastern Ohio. These features were caused by collapse of old mine workings beneath the highway. An attempt was made to delineate these features using geophysical methods with no avail. The geophysical methods that were tried comprised ground penetrating radar, seismic refraction, and electromagnetics. Subsequently, drilling was employed as the primary technique to delineate the voids. The collapse was believed to be caused by active mine subsidence which was exacerbated by the dewatering of adjacent abandoned mine workings. It is postulated that there was too much overburden for the radar to penetrate to the mined interval at the designated site. The tunnels were too deep to be detected by the electromagnetic technique utilized, and the seismic refraction method lacked adequate resolution to delineate the voids.

In view of the above discussion, it is imperative to know if there is a geophysical technique that will focus on areas of possible future collapse? There exist many miles of highway that have been built over shallow coal seams, mined in the late 1800's and early 1900's. Generally, the voids left by mining were not adequately mapped. Therefore, there are numerous sites susceptible to future collapse. Drilling would be prohibitively expensive as a searching tool. This study tested various geophysical methods to economically locate areas of possible future highway collapse, which should receive detailed study. The geophysical tools investigated in this study consisted of ground penetrating radar (GPR), gravity, P-wave and S-wave seismic refraction, seismic reflection, and surface wave studies. In 1998, in accordance with the recommendation of the Ohio Department of Transportation (ODOT) personnel, one site was selected in Jackson County and another in Vinton County. Both sites were located along Ohio Route 32. At these sites coal mines were known to exist beneath the highway and there was some evidence to suggest current failure. Phase I of this project intended to identify the capabilities and effectiveness of various geophysical techniques for detecting mine voids under highways. Subsequently, the most successful method(s) would be employed for use during the Phase II. In 1999 a Phase II test site was chosen in Perry County, Ohio. At this location, coal mines were also known to exist, but there was no surface evidence

to suggest that mine collapse had or would occur. Only two of the Phase I methods were tested during Phase II. These two methods were seismic refraction and dipole-dipole resistivity.

II. RESEARCH OBJECTIVES

The study consisted of two phases with distinct but related objectives.

A. Phase I

We tested several geophysical methods at a site with known collapse potential to determine which method or combination of methods would be most viable to detect and provide subsurface information on the problem zone. An important study goal was to identify a geophysical method that could be used on long sections of highway at an acceptable cost. The study's intent was not to develop detailed mapping of the sites. The methods tested were:

a) seismic refraction with compressional waves,
b) seismic refraction with shear waves,
c) fixed offset seismic reflection,
d) gravity,
e) 2D resistivity imaging,
f) ground penetrating radar (GPR), and
g) spectral analysis of surface waves (SASW).
h) Surface wave profiling (constant offset)

The seismic refraction investigations included tests of several seismic energy sources. These methods were studied to evaluate their ability to develop pertinent data while suppressing the effects of traffic noise.

Experience from past studies had revealed that a combination of gravity and seismic refraction with compressional waves was effective in studying the bedrock surface and identifying zones of incompetent rocks. In this study, we utilized the elastic wave generator (EWG III) as an impulsive source of seismic energy. Our previous experience studying fractured rock, has shown that shear wave refraction was even more sensitive to fractures than compressional wave refraction. A swept frequency vibrator, the Minivib, was an alternate seismic source, which we felt should be tested for this purpose because it might produce a signal which could be better separated from traffic noise. The same situation might also be true for SASW, using the Minivib as a wave source. The 2D-resistivity imaging would be nearly immune to the effects of traffic vibrations. It might,

however, be ineffective in areas with nearby fences and guardrails. The data were analyzed to determine the experimental designs to pursue for Phase II.

B. Phase II

The objective for Phase II was to test the techniques developed in Phase I along a 4.5-km section of highway. This test section was selected in consultation with ODOT personnel. The section was overlying several mapped abandoned underground mines. The selected geophysical techniques and data analysis designs from Phase I were implemented with improvements subsequently identified. Conditions that were likely to influence geophysical data, which were likely to be common in the highway margin environment, were to be identified.

After the geophysical data were processed and interpreted, zones underlain by competent, intact rock and zones of potential problems underlain by less competent, broken rock would be identified. Subsequently, test locations would be identified for ODOT to conduct borings. The results of these borings would be interpreted jointly by project scientists and collaborators and by ODOT personnel to determine the success of the geophysical surveys in locating problem zones.

III. GENERAL DESCRIPTION OF THE RESEARCH

This section of the report is divided into 3 subsections, one for each of the 3 sites. Figure 1 is a map showing the locations of the 3 sites. The first subsection contains the most details. Many aspects of the studies at the other two sites are similar. In the second and third subsections only significantly different aspects are discussed in detail.

A. Jackson County, Ohio – Phase I

a. Local Geology and Mining History

Southeastern Ohio is dominated by Carboniferous stratigraphy. Classification of the region's stratigraphy was completed as a result of early resource exploration for coal in southeastern Ohio, as documented by Crowell (1991). Coal was first discovered in 1799 and during the subsequent years several economic coal seams (Clarion, Brookville, Middle Kittanning, and Winters) were discovered. The discovered sites were extensively mined from shallow coal mines during the period from 1874 to 1923. As a result, the removal of the coal left structural voids. Given the near-surface location of the abandoned mine workings, it was necessary to determine the local geology and which coal seam, or seams, were located at a depth interval of 5 to 20 feet beneath the surface at the field site.

To aid in the interpretation of the geophysical field data, it was necessary to determine the near-surface geology and the absence or presence of coal below the site. The test site, which was recommended by ODOT, is shown on the map in Figure 1. ODOT conducted an extensive subsurface investigation in November 1998, drilling at 27 stations along the north and south sides of westbound State Route 32 (Figure 2). The compilation of the drilling data revealed that the coal seam beneath the field site is the Clarion coal seam or coal number 4A. The Clarion coal lies in the Clarion member of

Figure 1. Map of southeastern Ohio with the study sites noted.

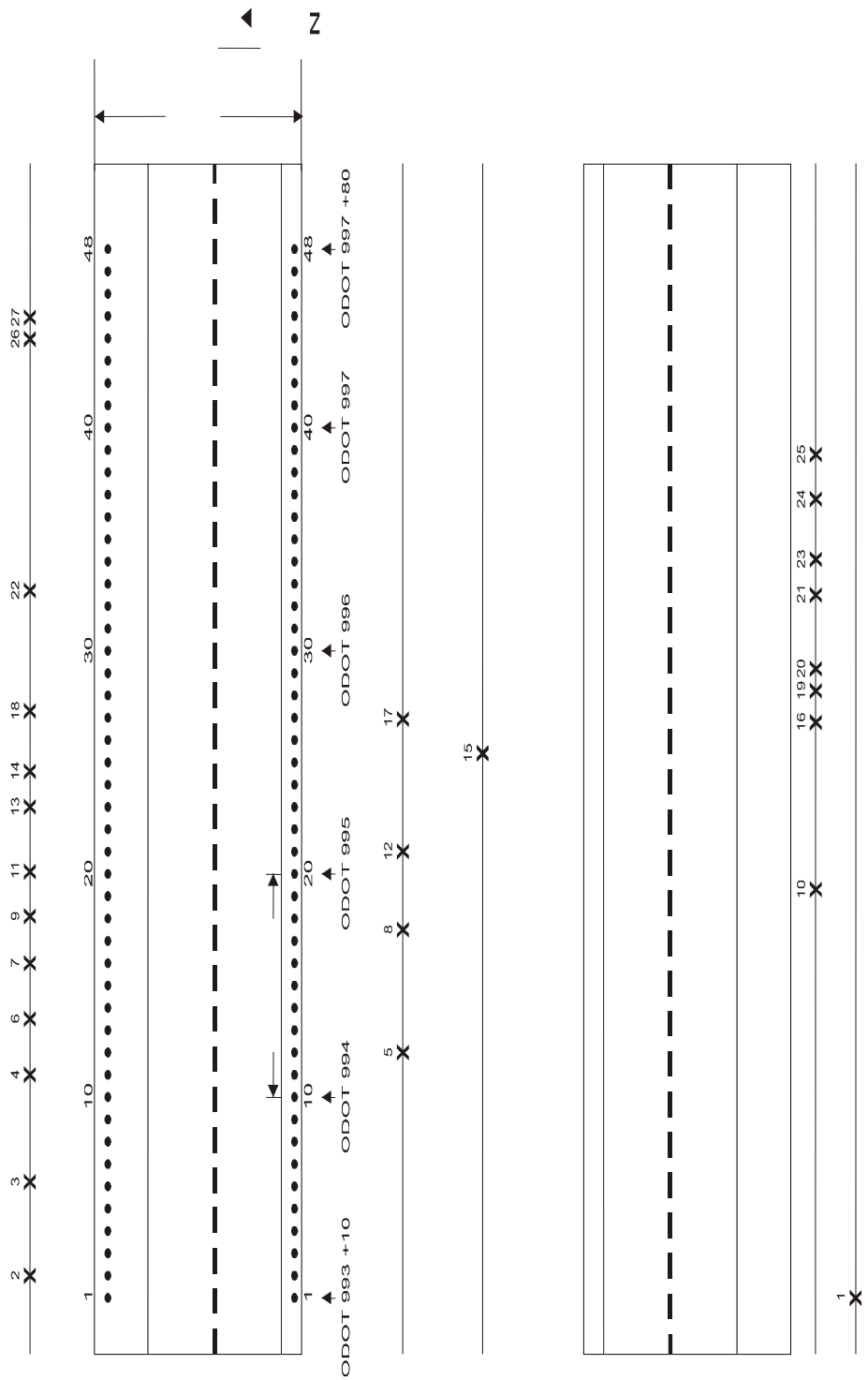

Figure 2. Diagram of the Jackson County site. X marks ODOT test borings. • marks geophysical test stations.

the Alleghany Formation of the Pennsylvanian System. The drilling data placed the top of the coal horizon at a depth between 1.5 and 4.6 m (5 to 15 feet) with an average depth of 2.7 m (9 feet) below the road surface (Figures 3 and 4). The range in depths is related

to the extensive mining of the coal and resulting collapse features due to its removal in the area.

Alleghany Formation

The Allegheny Formation is the middle formation of the strata represented from the Pennsylvanian System within the region. This formation overlies the Pottsville Formation and is partially overlain, in some areas, by the Conemaugh Formation. The Allegheny Formation is recognized as one of the region's most valuable formations, as it contains economic deposits of coal, clay, and limestone (Stout, 1927). Figure 5 is a generalized stratigraphic section of the Alleghany Formation as it exists in Vinton County, defined by Stout in 1927. The section is taken from Vinton County, which is approximately 5 miles east from the field site. Vinton County's stratigraphic information is used as the model for the area since the stratigraphy of Jackson County has not been extensively investigated at this point. This formation has an average thickness of approximately 236 feet and is comprised of limestones, shales, clays, sandstones, flint and numerous coal seams. The near surface location of the Clarion coal and the focus of this study constrain the relevant geology of the site to include the Vanport, Scrubgrass, Clarion, and Winters Members of the Allegheny Formation.

The Vanport Member has an average thickness of 7 feet and is comprised of two distinct lithologies, a gray fossiliferous limestone that varies in thickness from 1.2 to 3 m (4 to 10 feet) and a dark carbonaceous shale that has an average thickness of 0.6 m (2 feet). Underlying the Vanport Member is the Scrubgrass member. The Scrubgrass Member has an average thickness of 1.8 m (6 feet) and contains coal and shale lithologies.

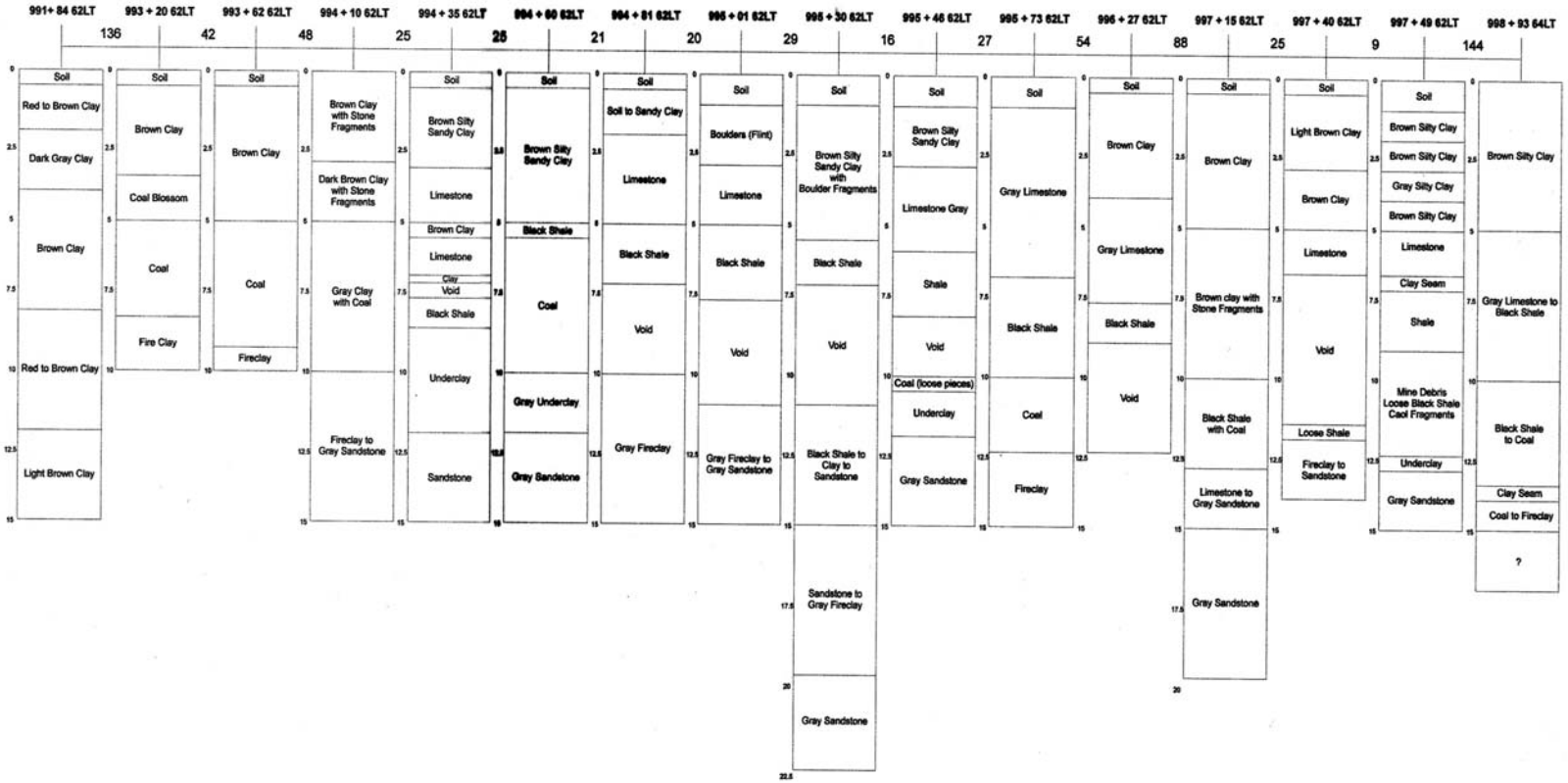
991+ 84 62LT
136
Soil
Red to Brown Clay
Dark Gray Clay
Brown Clay
Red to Brown Clay
Light Brown Clay
993 + 20 62LT
42
Soil
Brown Clay
Coal Blossom
Coal
Fire Clay
993 + 62 62LT
48
Soil
Brown Clay
Coal
Fireclay
994 + 10 62LT
25
Brown Clay with Stone Fragments
Dark Brown Clay with Stone Fragments
Gray Clay with Coal
Fireclay to Gray Sandstone
994 + 35 62LT
25
Soil
Brown Silty Sandy Clay
Limestone
Brown Clay
Limestone
Clay
Void
Black Shale
Underclay
Sandstone
994 + 60 62LT
21
Soil
Brown Silty Sandy Clay
Black Shale
Coal
Gray Underclay
Gray Sandstone
994 + 81 62LT
20
Soil
Soil to Sandy Clay
Limestone
Black Shale
Void
Gray Fireclay
995 + 01 62LT
29
Soil
Boulders (Flint)
Limestone
Black Shale
Void
Gray Fireclay to Gray Sandstone
995 + 30 62LT
16
Soil
Brown Silty Sandy Clay with Boulder Fragments
Black Shale
Void
Black Shale to Clay to Sandstone
Sandstone to Gray Fireclay
Gray Sandstone
995 + 46 62LT
27
Soil
Brown Silty Sandy Clay
Limestone Gray
Shale
Void
Coal (loose pieces)
Underclay
Gray Sandstone
995 + 73 62LT
54
Soil
Gray Limestone
Black Shale
Coal
Fireclay
996 + 27 62LT
88
Soil
Brown Clay
Gray Limestone
Black Shale
Void
997 + 15 62LT
25
Soil
Brown Clay
Brown clay with Stone Fragments
Black Shale with Coal
Limestone to Gray Sandstone
Gray Sandstone
997 + 40 62LT
9
Soil
Light Brown Clay
Brown Clay
Limestone
Void
Loose Shale
Fireclay to Sandstone
997 + 49 62LT
144
Soil
Brown Silty Clay
Brown Silty Clay
Gray Silty Clay
Brown Silty Clay
Limestone
Clay Seam
Shale
Mine Debris Loose Black Shale Coal Fragments
Underclay
Gray Sandstone
998 + 93 64LT
Brown Silty Clay
Gray Limestone to Black Shale
Black Shale to Coal
Clay Seam
Coal to Fireclay
?

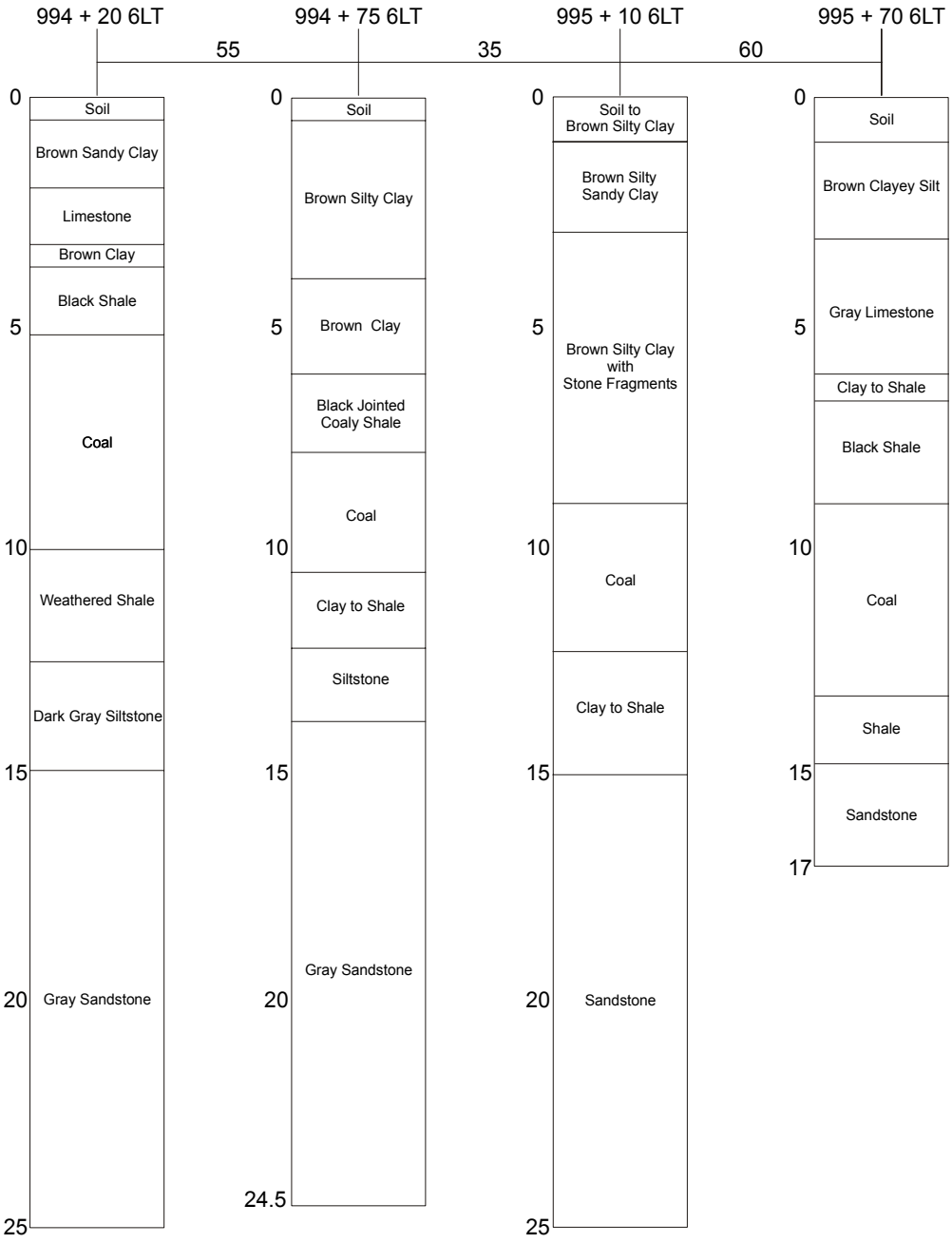

Figure 4. Lithologic interpretation of drilling logs on the south side of State Route 32 in Jackson County (provided by ODOT).

System	Formation	Member	General Description	Thickness	
				Ft.	In.
Pennsylvanian	Allegheny	Upper Freeport	Coal (generally thin, often absent)	1	0
			Clay	5	0
			Shale, gray	2	6
			Limestone (nodular)		5
		Unamed	Coal (thin, often absent)		1
		Bolivar	Clay, flint (irregular)	6	0
			Shale, gray	9	9
		Upper Freeport	Sandstone (largely replaced by shale)	18	0
		Lower Freeport	Coal (occasionally present)		3
			Clay	6	0
			Shale, gray (siliceous)	12	0
			Limestone (nodular)		6
			Sandstone (often replaced by shale)	30	0
			Shale gray (siliceous)	5	0
		Middle Kittanning	Coal (persistent)	2	6
			Clay, shale	2	0
			Shale and sandstone	22	0
		Strasburg	Coal (local and thin)		2
		Oak Hill	Clay, flint (irregular)	4	0
		Hamden	Ore (local)	3	0
			Shale, gray (siliceous)	5	2
		Lower Kittanning	Coal (persistent)	1	10
			Clay	7	0
			Shale and sandstone	22	6
		Vanport or Ferriferous	Ore (locally present)		5
		Vanport	Limestone, gray (fossiliferous)	4	7
			Shale, dark (carbonaceous)	2	2
		Scrubgrass	Coal (locally present)		11
			Shale, black (carbonaceous)	4	9
		Clarion	Coal (persistent)	3	2
			Clay, flint (locally well developed)	6	0
			Sandstone (only locally well developed)	10	0
			Shale, gray (siliceous)	4	0
		Winters	Coal (locally with good thickness)	2	3
			Clay	3	7
		Zaleski	Flint, gray to black (calcareous)	1	2
			Shale, dark (siliceous)	1	0
		Ogan	Coal (generally thin, often absent)		10
			Clay	2	8
			Shale and sandstone	16	4
		Putnam Hill	Limestone and shale (fossiliferous)	2	9
		Brookville	Coal (locally of value)	2	5
			Total	235	8

Figure 5. Generalized stratigraphic section of the Allegheny Formation in nearby Vinton County. (Stout, 1927)

The Scrubgrass coal is characterized as a thin shaly coal that has an average thickness of 0.28 m (11 inches) and is only locally present. The lower portion of the Scrubgrass is recognized by the black carbonaceous shale that has an average thickness of 1.5 m (5 feet). The Scrubgrass Member is underlain by the Clarion Member.

The Clarion Member has an average thickness of 7 m (23 feet) and is subdivided into four lithologies. The top of the Clarion is recognized by the Clarion coal or coal 4A. It is persistent and normally developed and its thickness ranges from 0.3 to 1.8 m (1 to 6 feet). The coal is underlain by a clay that is distinguished by its plastic character and ranges in thickness from 0.6 to 4.9 m (2 to 16 feet). Underlying the clay is sandstone that ranges in thickness from 1.5 to 7.6 m (5 to 25 feet) and is characterized as a massive loosely cemented micaceous sandstone. At the base of the Clarion Member is a gray siliceous shale that has an average thickness of 1.2 m (4 feet). Underlying the Clarion Member is the Winters Member.

The Winters Member has two distinct lithologies, coal and clay. The Winters coal has an average thickness of 1.8 m (6 feet) and is comprised of a coal whose composition varies from pure to shaly with a range in thickness from centimeters to 1.2 m (4 feet) (Stout, 1927). Beneath the coal is a clay that is described as plastic and varies in thickness from 1.8 to 30 m (6 to 10 feet). Figure 6 shows two measured sections (section 4192 & 16191) of stratigraphy obtained by the Ohio Division of Geological Survey.

The two sections and the geology described are located within a mile radius of the field site. Both sections show that the Clarion coal member does exist, with a slight variance in thickness. Section 4192 shows the Clarion overlain by the Lower Kittanning Shale, Vanport ore, limestone, and shale and the Scrubgrass shale. Section 4192 also shows the Clarion underlain by the Winters coal and clay. The members present below the Winters have not been identified. The geology present in Section 16191 agrees with that shown in Section 4192, exhibiting the Clarion overlain once again by the Vanport Limestone and shale, and the Scrubgrass shale.

Measured section 4192 SW 1/4 section 8 to SW 1/4 section 9 Milton Township, Jackson County			Measured section 16191 NW 1/4 section 16 Milton Township, Jackson County		
Interpreted Member	Lithology Present	Thickness (m)	Interpreted Member	Lithology Present	Thickness (m)
Lower Kittanning	Shale	0.10	Vanport	Vanport	0.46
Vanport	Ore	0.10		Shale	1.17
	Limestone	1.52	Scrubgrass	Shale, black	0.51
	Shale, gray	0.23	Clarion	Clarion coal	1.47
Scrubgrass	Shale, black	0.51			
Clarion	Clarion coal	1.45			
	Clay and covered	3.96			
	Sandstone	4.27			
	Covered	3.66			
Winters	Coal	0.15			
	Clay	1.07			
?	Sandstone	2.13			
	Covered	8.23			
	Sandstone	3.96			
	Ore and covered	0.61			
	Clay	0.91			
	Sandstone and covered	6.10			

Figure 6. Two measured sections of the geologic formations in the zone of interest in Jackson County. (Ohio Division of Geological Survey)

Figure 6. Two measured sections of the geologic formations in the zone of interest in Jackson County. (Ohio Division of Geological Survey)

The geology of these two sections is representative of the geology recorded during ODOT's onsite drilling investigation and the generalized stratigraphic section of the Allegheny Formation. With the geology determined, models could be produced using the geological information to aid in the interpretation of the geophysical results gathered at the field site.

b. Methods and Acquisition

Six types of geophysical methods were employed to locate potential collapse areas. The methods consist of compressional (P) and shear (S) wave seismic refraction, P wave reflection, resistivity, gravity, ground penetrating radar (GPR), and seismic surface

waves. Each method has proven to be useful in previous studies of the subsurface of the earth (Burger, 1992; Reynold, 1997).

Seismic Refraction

Seismic refraction studies are useful in determining depth to bedrock and lateral changes in velocities, indicating changes in the subsurface material and, more importantly, potential collapse features. Two types of seismic refraction data were collected at the site, P and S wave refraction. Once collected, a comparison of the P and S wave data was completed to detect any variations in bedrock competence above the abandoned coal mine tunnels. The P and S wave refraction data were collected using a 36 channel Strataview engineering seismograph with 30 hertz geophones. A 146-m (480-foot) line with a geophone station spacing of 3.048 m (10 feet) was employed on both the north and south side of west bound State Route 32. The line geometry for both the P and S wave surveys was the same and can be seen in Figure 7 along with the locations of the energy source (shot points). Each line runs parallel to the road and has an offset of 2.4 m (8 feet) from the pavement. The P wave data were gathered using a Bison elastic wave generator as an energy source. The S wave data were gathered using a metal box that was orientated 90 degrees to the seismic line. Each end of the box was then struck at ± 90 degrees from the line. By striking the box in this manner, the polarity of the data was reversed in one direction and adding these together effectively canceled out the P waves, leaving only S waves. Elevations of each geophone's position were surveyed using a theodolite to correct the arrival times of each geophone trace.

The collected refraction data were saved into data (DAT) files and imported into two interpretation software packages, SIP by Rimrock Geophysics and Promax by Landmark Graphics Corporation. Travel time curves, bedrock depth models and seismic velocities for both the P and S wave surveys were generated using SIP. Individual seismic records for both surveys were generated by Promax to visually show any variations in amplitude that indicate lateral changes in the composition or competence of bedrock material. The velocity data generated by SIP along with the travel time curves were searched for anomalies that indicate potential collapse areas in the bedrock.

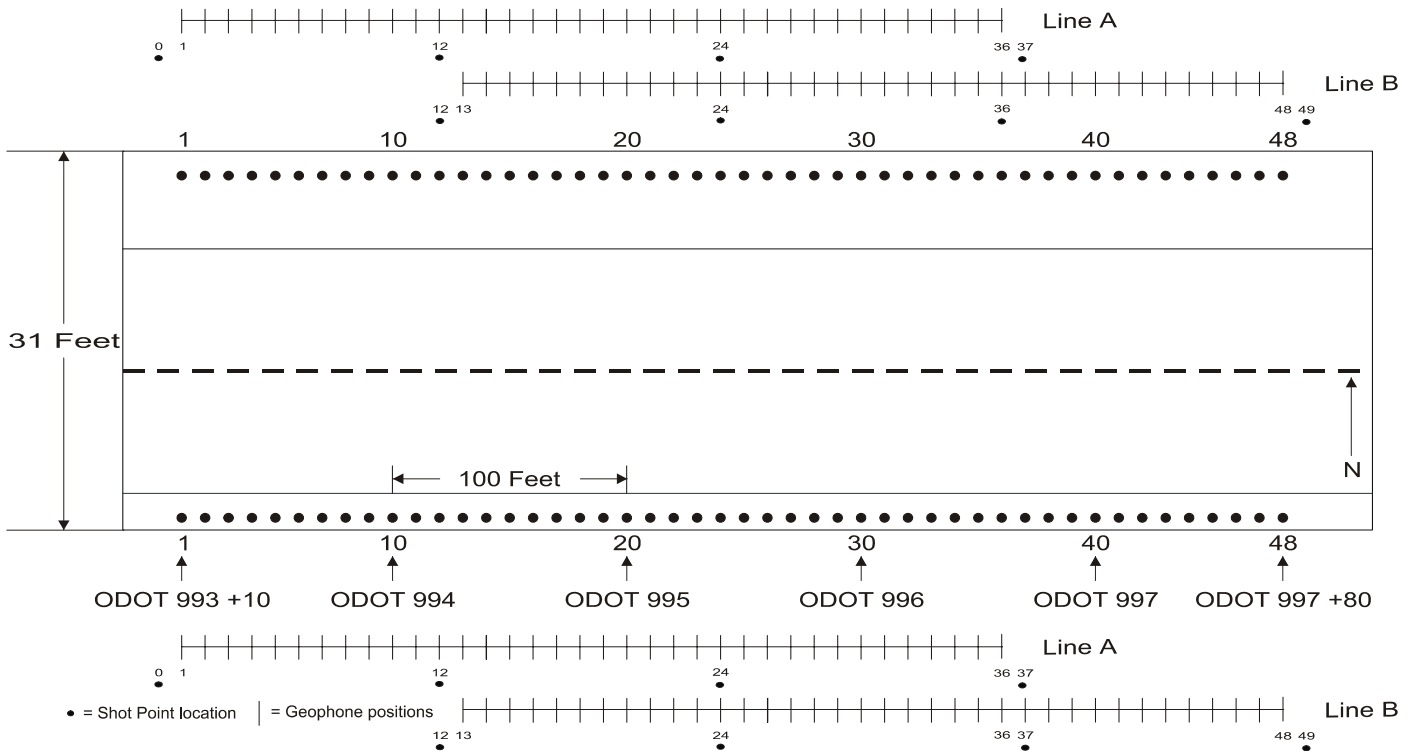

Figure 7. Layout diagram for seismic lines. Lines A and B are colinear but are shown displaced for clarity.

Seismic Reflection

Seismic reflection methods are commonly employed by the hydrocarbon industry and are useful in imaging boundaries in the subsurface, such as bedding, faults, and potentially voids. At boundaries where the seismic velocity and/or density of the rock changes, such as the margins of voids, some of the seismic energy is reflected back toward the surface. At the Jackson County site, a P-wave seismic reflection profile was collected both along the median and along the margin of the north shoulder to the west-bound lanes. These data were collected using an IVI-minivibe sweeping 8 seconds from 40Hz to 250Hz. Four sweeps were summed at each station. A single, 30 Hz geophone was located at each station at a 3.048 meter (10 foot) spacing, and 36 stations were simultaneously recorded using a 36-channel StrataView recording system. These data (saved as *.DAT files on the StrataView) were imported and processed using the ProMax seismic processing system at Wright State University. The voids at the Jackson County site were known to be very shallow (~3 meters) from some drill holes, which poses a challenge for seismic reflection methods.

Resistivity

Resistivity data collected in the dipole-dipole configuration were used to generate 2-dimensional models indicating areas of resistivity highs and lows corresponding to potential collapse features. Resistivity surveys measure the ability of a geologic material to resist the flow of electrical current. Resistivity surveys are used extensively in the environmental industry to locate buried metal drums, depth to freshwater-saltwater interface, subsurface cavities, and mine shafts. Resistivity data collected in this survey were used to locate subsurface anomalies that correspond to cavities and mine tunnels. Both the cavities and mine tunnels may yield extremely high or low resistivity values depending on the condition of voids (the amount of collapse and fill material within it) and whether the spaces are filled with water or air.

Resistivity data were acquired using the Sting/Swift R1 resistivity meter, consisting of 28 active nodes attached to metallic spikes. Resistivity values are obtained by driving the metallic spikes into the ground, and fastening the nodes to them. Current is generated

between a pair of the electrodes and potential is measured between another pair in a dipole-dipole configuration. The system automatically sequences through all reasonable dipole-dipole configurations of the 28 electrodes. For each configuration it calculates the apparent resistivity. The resistivity measurement is then stored for later modeling and interpretation. Data were gathered along two 146 m (480-foot) profiles on the north and south sides of westbound State Route 32. The north side of the road had an electrode spacing of 1.5 m (5 feet), whereas the south side had an electrode spacing of 3 m (10 feet). The differing electrode spacing allowed for the determination of which spacing gave the best resolution of the subsurface to be made. The collected resistivity data were downloaded into a two-dimensional modeling program Res2dinv (Loke, 1999) from Advanced Geosciences, Inc. Models were generated and interpreted. While the models themselves show areas of high and low resistivity values, their causes are non-unique. The resistivity signature of the mine tunnels could appear either as a high, low or both. If the mine tunnels are filled with water or have moisture present, they will produce a resistivity low; whereas, if they are filled with air, they will produce a resistivity high. Given that the present condition of the mine is not known, there exists the possibility that the mine tunnels could be fully to partially water or air filled. Ultimately the condition of the mine tunnels and causes of the resistivity anomalies were determined through prior site knowledge, drilling or excavation.

Gravity

Gravity surveys detect density variations in the subsurface. The density anomalies indicate lateral changes in subsurface units, which may indicate areas of potential collapse features. Gravity surveys measure variations in the Earth's gravitational field caused by changes in the density of subsurface material. Gravity surveys have been used extensively in hydrocarbon exploration, regional geologic studies, detection of buried valleys, and mineral deposit detection. With the advance of technology, very small changes in density can now be measured. In order to find these small changes, a micro-gravity survey method is used to gain adequate detail of the density variations. Micro-gravity surveys are conducted on a very small scale and are capable of detecting sub-

surface cavities as small as 1 m (3 feet) in diameter within 4.5 m (15 feet) of the surface. These dimensions are similar to those expected for a mine tunnel.

Gravity data were acquired using a Lacoste and Romberg gravimeter. Gravity readings were taken at 48 stations (Figure 8), spaced at an interval of 3m (10 feet) on the north and south sides of west bound State Route 32. A base station was established at station 25 on the north side of the road. Readings at the base station were taken at the beginning of the survey, every hour thereafter, and at the end of the survey. Base station readings were taken to correct for instrument drift and tidal variation as a function of time. Two readings were taken at each station, with the corresponding time of each station reading recorded, additional readings were taken if the first two readings did not agree. Elevations of the stations were taken using a theodolite to ensure accurate elevation control. The gravity data have a precision of ± 0.01 mGals, if the relative elevations are known to within 3 cm and the relative latitude of each station is known to within 12 m, which is achievable given the technology used.

After the acquisition of the gravity data, several corrections must be applied. The data must first be corrected for instrument drift and tidal variation as a function of time. The rates of instrument drift between the readings taken at the base station at intervals throughout the day were calculated and applied to each survey station's gravity reading. This yields a drift corrected gravity reading for each station. The drift corrected reading was then multiplied by the gravimeter instrument calibration constant to obtain an uncorrected relative gravity reading in milligals (mGals). Next, the free-air, Bouguer and latitude corrections are applied to the uncorrected gravity readings. The free-air and Bouguer corrections depend on knowing the relative elevation of each station. The relative elevation of each station was determined to an accuracy of ± 1cm by surveying with a theodolite. The latitude correction relies on knowing the latitude position of each station. Given that the orientation of State Route 32 at the site is east-west and the north and south sides of the road are separated by approximately 30 feet, the

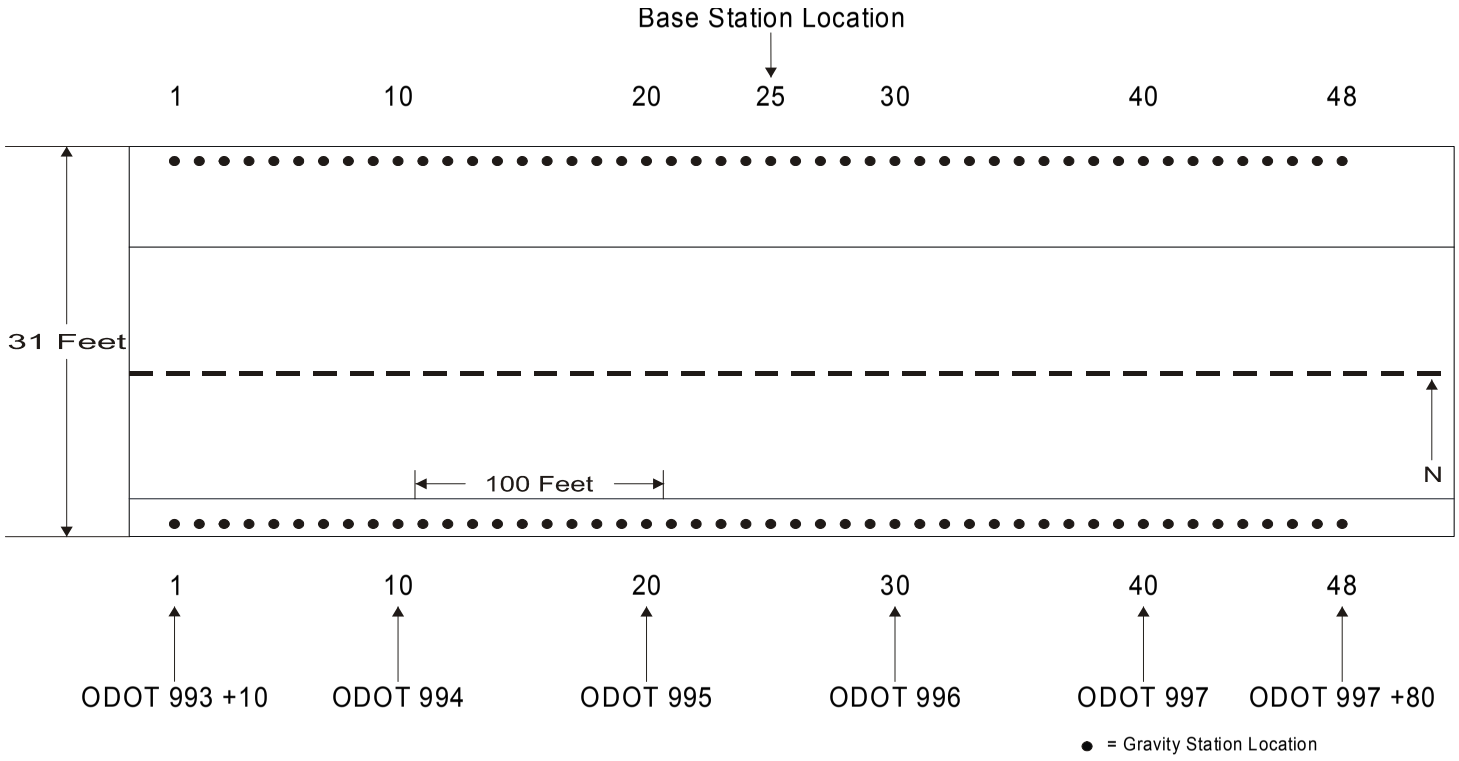
Base Station Location
1
10
20
25
30
40
48
31 Feet
100 Feet
N
1
10
20
30
40
48
ODOT 993 +10
ODOT 994
ODOT 995
ODOT 996
ODOT 997
ODOT 997 +80
● = Gravity Station Location

latitude correction was effectively removed when the regional gravity trend of the area is removed from the gravity data. The free-air correction is the difference between gravity measured at sea level and at a station elevation above sea level, with no rock in between. The correction was added to the gravity reading. The Bouguer correction calculates the extra gravitational pull by a infinite slab of rock with a thickness equal to the elevation of the station above sea level. This correction was subtracted. The resulting gravity value after performing these corrections is called the Bouguer anomaly.

The Bouguer anomaly can be calculated using the following formula:

$$g_B = g_r + (0.3086)(e_r) - (0.0419)(\rho)(e_r)$$

where g_B = Bouguer anomaly (mGal)

g_r = drift corrected value (mGal)

e_r = relative elevation (m)

ρ = density of subsurface material (g/cm^3).

The density (ρ) used in this survey was 2.0 g/cm^3.

The Bouguer anomaly values for all of the stations, on each side of the highway were then imported into Microsoft Excel™, where it was graphed so that changes in subsurface density could be observed. Ultimately the lateral variations in density cannot be uniquely determined from the Bouguer anomaly. Supplementary information from drilling, excavation, and knowledge of the site's geology is necessary to constrain the interpretation of the gravity results.

Ground Penetrating Radar

Ground Penetrating Radar (GPR) was not one of the methods we had proposed to use during this project due to the significant presence of clay in the soil, shale in the underlying bedrock, and the depth of the target (especially the Vinton County site). Later in the course of our investigation, however, we decided to check the effectiveness of the

GPR. We did take the opportunity to test GPR at each site using a GSSI SIR-3 radar system available at Wright State University.

GPR surveys involve sending pulses of radar signals into the ground from an antenna dragged or rolled across the surface. At interfaces in the subsurface where the dielectric properties change (i.e., boundaries where the radar wave transmission velocity changes), part of the radar signal is reflected and may be received by the antenna at the surface. At the boundary of a void, being a boundary between rock material and air or water (either resulting in a significant change in radar velocity), a substantial reflection would be expected to occur. However, the presence of clay and water in the overlying soil and rock can considerably attenuate the radar signal and limit depth penetration. We tested both 80MHz and 300 MHz antennae, the lower frequency used especially because it would potentially give the greatest penetration.

Seismic Surface Wave Investigation

Dr. Luke and B. Avar (Universtiy of Nevada at Las Vegas) investigated seismic surface wave methods at the site. Due to their dispersive nature in layered media and their ease of measurement, surface waves are an attractive choice for developing shear stiffness profiles (Stokoe et al., 1994) and detecting subsurface anomalies, such as cavities (Luke and Chase, 1997) and obstacles (Gucunski et al., 1992; Luke and Brady, 1998). In this study, two approaches were investigated for rapid assessment of potential problem areas,sounding (the SASW method) and profiling (constant-offset method).

Data collection, reduction, and interpretation

Sounding Approach

In the sounding mode, the Spectral-Analysis-of-Surface-Waves (SASW) method was employed to develop shear wave velocity profiles at distinct locations. The SASW method is a non-intrusive, non-destructive site investigation technique that employs seismic surface waves to generate one-dimensional shear wave velocity profiles of the subsurface (Stokoe et al., 1994). This approach is intended to delineate areas of reduced overall stiffness, which might be caused by cavities or collapsed regions above cavities.

Equipment used included:

- Geophones, 2 ea., resonant frequency 4.5 Hz, manufactured by Mark Products
- Dynamic signal analyzer, two channel, Stanford Research Systems model SR-780
- Sledge hammer and various smaller hammers
- Elastic wave generator, Bison EWG-III (property of Wright State University)

Surface wave measurements were collected at multiple receiver spacings using a common center point. The smallest spacing was 0.5 m. The spacing was doubled 6 times until a maximum of 32 m was attained. The spacing refers to the distance between receivers, which is also equal to the source-to-near-receiver distance. For smaller spacings, source energy was generated by dropping or pounding with hammers. An elastic wave generator (EWG) was used for larger spacings.

SASW measurements were conducted with the source placed sequentially on opposite sides of the geophone pair, in forward (waves travelling east) and reverse (waves travelling west) directions. Only the measurements in the direction having superior quality in terms of resolution and coherence were used for shear wave velocity profile calculations. However, we note that such a "loss of quality" might be due to the presence of a cavity and should be considered qualitatively in that sense.

SASW measurements were performed at six locations, designated by letters, at the Jackson County site (Figure 9). The position of each setup is described with respect to linear arrays running from west to east along the median and the north shoulder of the road. The arrays extended 150 m (500 ft), from ODOT Sta. 993 to Sta. 998. (There are 30 m (100 ft) between ODOT stations.) The flagged WSU stations, spaced at 3.0 m (10 ft) intervals, are labeled 0 (corresponding ODOT Sta. 993) through 50 (corresponding ODOT Sta. 998).

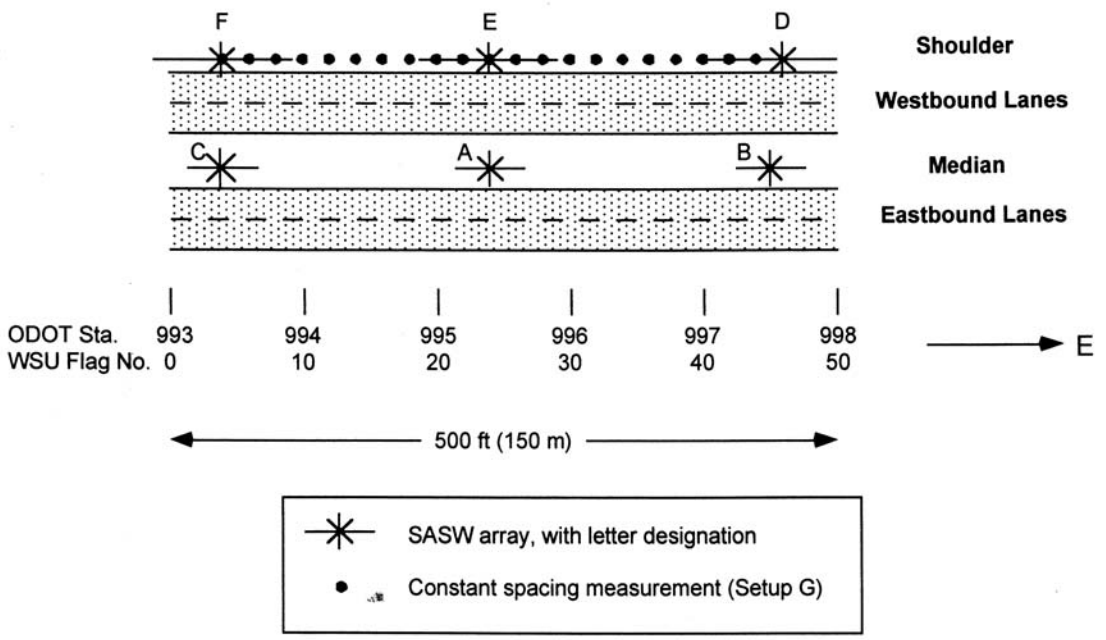

Figure 9. Surface wave study locations at the Jackson County site.

Setups A, B and C were situated in the median. The width of the median is 12 m (40 ft). The SASW arrays are approximately 1.5 - 2 m north of the WSU flags. For all SASW setups on the median, the maximum receiver spacing used was 16 meters.
Setup A is at Sta. 995+40 (WSU Sta. 24), 1.3 m south of the centerline of the median and in line with a patch on the highway marking a repair necessitated by the collapse of an abandoned coal mine. The repaired section extends from Sta. 995+15 to 995+65. (ODOT gives the position of the center of the test pit at Sta. 995+50.) Setup B is at ODOT Sta.. 997+50 (WSU Sta. 45), and approximately 2 m south of the centerline of the median. Setup C is at ODOT Sta. 993+40 (WSU Sta. 4), and approximately 1.5 m south of the centerline of the median. Setups D, E, and F were on the north shoulder, approximately 1.5-2 m north of the pavement edge, and also spaced 60 m (200ft) apart. For all SASW setups on the north shoulder, the maximum receiver spacing used was 32 meters. Setup D is at ODOT Sta. 997+60 (WSU Sta. 46), at the east end of test section. Setup E is approximately at the center of the test section, at ODOT Sta. 995+40 (WSU Sta. 24). Setup F is at the west end of test section, at ODOT Sta. 993+40 (WSU Sta. 4).

In an SASW measurement, shear wave velocity profiles are generated through a data reduction process involving the development of experimental dispersion curves, followed by inversion. Time histories collected at a pair of geophones are processed in real time using the dynamic signal analyzer, to yield cross power spectrum in terms of phase, and coherence. After this initial step, data reduction was completed in the laboratory using the MATLAB computer program.

The process of development of experimental dispersion curves involves:

1. Selection of best-quality phase diagrams among multiple iterations for each receiver spacing
2. Removal of undesirable portions of the record through masking
3. Unwrapping the wrapped phase information
4. Calculating Rayleigh wave velocity as a function of wavelength
5. Combining data from multiple spacings into a composite dispersion curve
6. Condensing the composite dispersion curve to approximately 100 points, but only if unique aspects of the curve are not suppressed by this action. [The scatter in the data may be important for cavity detection.]

In the inversion process, a profile indicating the variation in shear wave velocity with depth is generated by iteratively fitting a theoretical dispersion curve to the experimental curve. This is accomplished using plane wave theory assuming propagation of an elastic, fundamental-mode Rayleigh wave through a layered medium. The layers are characterized by their thickness, shear wave velocity, Poisson's ratio, and density. The curve fit is accomplished through trial and error, by eye.

Since the inversion process is relatively insensitive to reasonable perturbations in density and Poisson's ratio, the same values were used for both soil and rock. Densities and Poisson's ratios used were 1800 kg/m^3 and 0.3, respectively (Munk and Sheet, 1997).

Profiling approach

In the profiling mode, also called the constant-offset approach, measurements are made using paired receivers at constant offset and constant spacing in order to observe magnitudes and spectral content of body wave interference. This approach is geared toward rapid detection of discrete cavities or major weakened zones caused by cavity collapse.

In a profiling measurement, the phase-difference data collected in forward and reverse directions are compared to detect anomalies. Fluctuations in the dispersion curves will be caused by higher mode conversions and reflection of body waves off the cavity. This higher-velocity interference will reduce the amplitude of the phase difference between receivers (Gucunski et al., 1996). The effects of body wave reflections should be stronger in one direction than the other if the stiffness anomaly is closer to one receiver. In addition, fluctuations in measured phase difference should be stronger when the source is closer to the cavity than in the opposite configuration (Luke and Chase, 1997; Luke and Brady, 1998).

The equipment set used for profiling measurements was the same as that used for SASW measurements. Source energy was applied with either a sledgehammer or the EWG. Receiver spacing was selected to target cavities at a depth of 5 to 8 m. For a site lacking significant stiffness contrasts, the sampled depth of the surface wave is one-third to one-half of the wavelength (Vrettos and Prange, 1990). Surface wave measurements generate useable data over the approximate wavelength range of one-half to two times the receiver spacing; thus, the sampled depth is on the order of one-sixth to one times the receiver spacing. The preferred receiver spacing was 8 m, to match the largest depth of cavity expected.

Constant offset (profiling) measurements were performed along a single 125-m (420-ft) long array (Figure 9) using a 6.0 m offset and 8.0 m receiver spacing (Setup G). Source energy was applied with a sledgehammer. This setup was located on the north shoulder, starting from WSU Sta. 4 (ODOT Sta. 993+40) and ending at Sta. 44 (ODOT Sta. 997+40).

Data reduction for profiling measurements was quite straightforward. Phase difference data for each station were unwrapped automatically for the forward and reverse directions using a standard procedure coded into MATLAB. The phase data were then manually adjusted in increments of 2π radians so that they matched at slightly negative values in the range of 15 to 20 Hz. In making the manual correction, we assume that 1) the effective sampling depth for surface wave is approximately one-third of the wavelength, 2) the mines are no deeper than 8 m, 3) the Rayleigh wave velocity of the rock beneath the mines is approximately 100 m/sec, and 4) the earth beneath the mines is homogeneous. Thus, the frequency 20 Hz corresponds to a sampled depth of approximately 16 m, which is well beneath the mines. We applied manual corrections to the phase data after automatic unwrapping so that they match at a value slightly less than zero (approximately –1 radian) at a frequency of 20 Hz. The adjustments, which are necessitated by shortcomings in the automatic unwrapping process, are made in increments of 2π radians. No other corrections are made, although other errors caused by automatic unwrapping may be present. Other errors can be recognized by sudden shifts that are in increments of 2π radians, after which the curves remain parallel. An example of this will be seen later in this report at the 60-Hz frequency of the record collected at Sta. 72 on the shoulder at the Vinton County site (Setup K).

Significant differences in phase between forward and reverse data sets, other than the unwrapping errors described above and the differences at frequencies less than 20 Hz, are assumed to be caused by the presence of cavities or rubble zones between the receivers. Differences at higher frequencies represent shallow features, which may be unrelated to the mines. For example (shown later in this report), the difference between forward and reverse measurements at Sta. 68 on the shoulder at the Vinton County site is large, but the two curves only diverge at frequencies higher than 60 Hz. Assuming a shear wave velocity of 500 m/sec, the effective depth of the anomaly is less than three meters. Adjoining records can be examined to estimate the lateral extent of the anomalies.

Seismic Refraction Results

P-wave Results

SIP models

The SIP software by Rimrock Geophysics was used to read each seismic record and pick their first breaks. Travel time curves were generated from the first break times and the source to geophone distances. We examined linear segments of each curve and assigned a layer number to each point on the curve corresponding to its refraction interface. (Travel time curves are included as Appendix A). To gain an insight into the depth of the interface generating the refraction, the travel times from shot point A, spread A on the north side were imported into Refractsolve, a program that calculates the depth to each refraction interface from travel time data. The resulting model (Appendix B) revealed that the source of the refraction energy (second interface on model) was at an average depth of 3.4 m (11 feet), which (based on the drilling results from ODOT) is the average depth to the base of the coal seam. Depth models for each profile (Figure 10 is the north side and Figure 11 is the south side) were generated by SIP through a process of time delay calculations, 3 iterations of ray path tracing, and adjusting the models based on those results. It should be mentioned that the depth to bedrock on the models generated is in error, given the presence of voids beneath the site that slow the seismic waves and consequently increase the travel times. The most important information is the pattern of peaks and valleys shown on the models. The patterns on the models are the result of the refracted rays taking longer times traveling from the base of the coal back up through the mined out areas than through intact rock. The longer travel time makes the depth in the vicinity of the voids appear deeper than they actually are. The peaks represent more correct depths where the waves pass through intact portions of the coal.

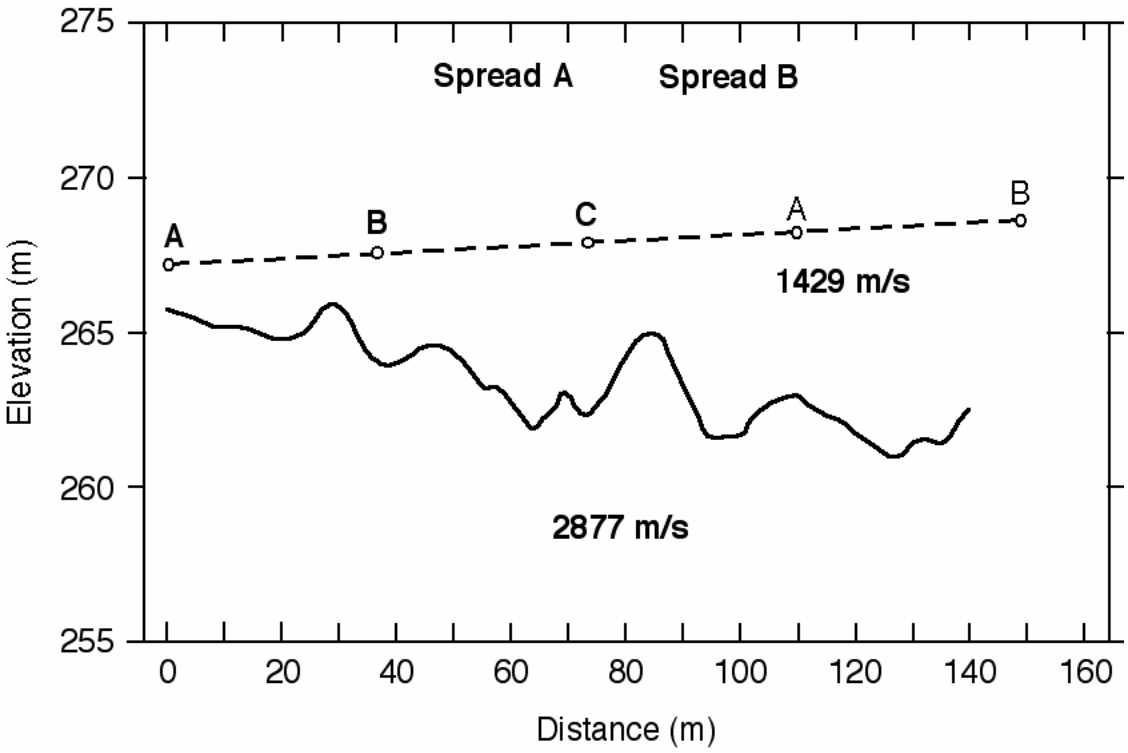

Figure 10. Apparent depth profile along the north side from P-wave seismic refraction.

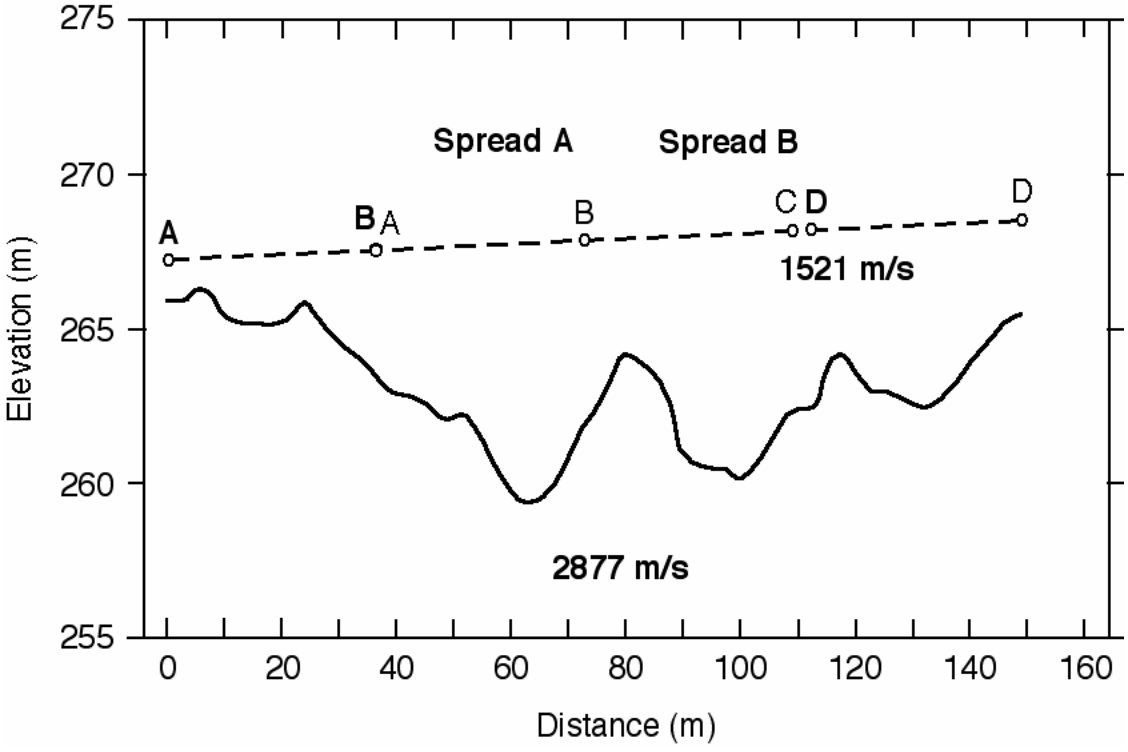

Figure 11. Apparent depth profile along the south side from P-wave seismic refraction

Signal Attenuations

The P wave refraction data collected at the site revealed distinct zones of signal attenuation across both the north and south side profiles, which are readily visible from the trace displays generated by Promax. Figure 12 shows two shot records, from geophone positions 1-36 with different shotpoints, located on the north side of the road. Record 1 has a shot point located at geophone position 12, whereas record 2 has a shotpoint located 3 m (10 feet) west of geophone position 1. The two records displayed in Figure 12 are the raw field data. The records show two distinct zones of signal attenuation detected between individual geophone positions . The first zone shown on both records is between geophone positions 17-24, and the second, recorded between geophone positions 12-15 is visible only in record 2, due to the near proximity of the source to the geophone position in record 1. Records for both spreads (stations 1-36 and 13-48) located on the north and south sides of the road were visually inspected for signal attenuations. The position where the signal attenuations were observed was recorded

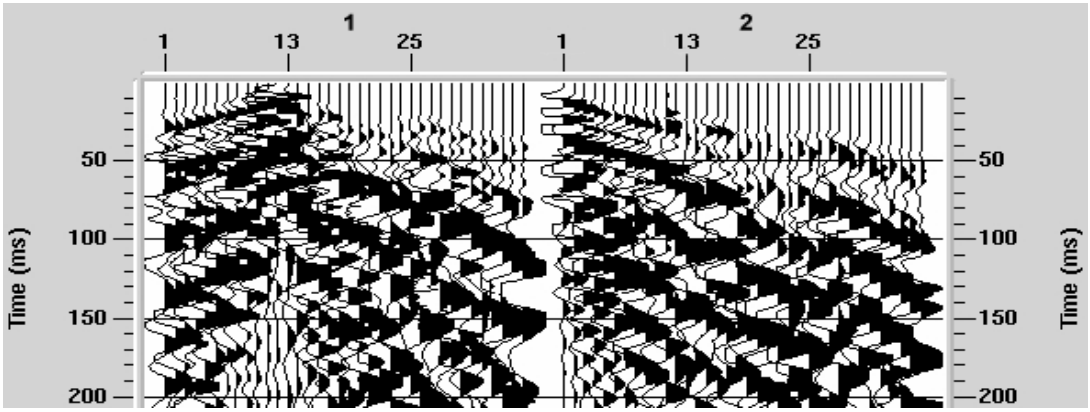

Figure 12. P-wave sesimic data records showing signal attenuation.

and a map showing their locations was made. Figure 13 shows the zones (marked by brackets) where the signal attenuations were seen on individual records. A number besides a bracket indicates more than one record detected signal attenuation within that

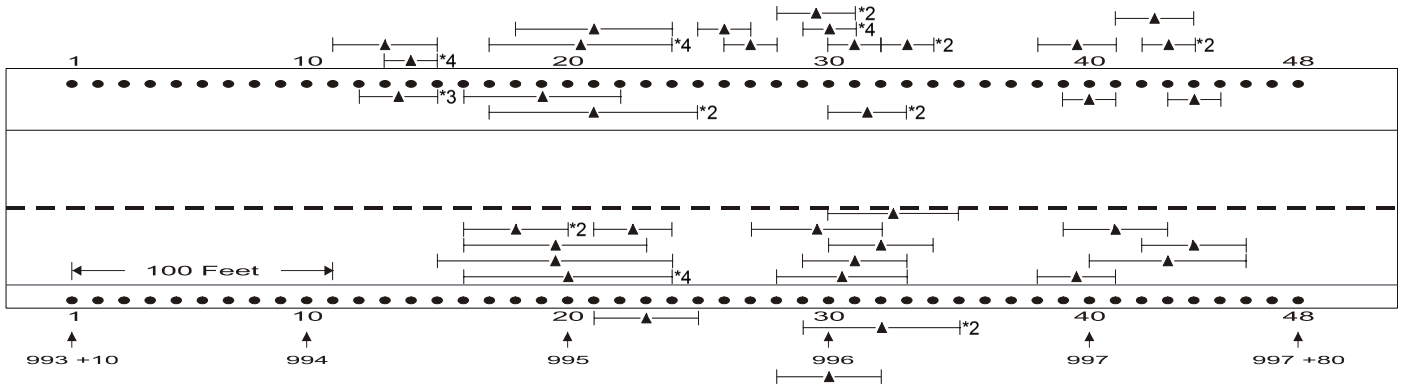

Figure 13. Zones of observed attenuation of P-wave seismic signals. Brackets indicate the extent of the zones. Adjacent numbers show the number of records on which attenuation in that zone was observed.

bracketed zone. Figure 13 shows that there is good correlation between multiple refraction records locating zones of signal attenuation. The correlation indicates that the signal attenuations recorded in both profiles detected the mined out areas of coal, the voids as a result of the coals removal and the intact portions of coal left in place to support the roof. The signal attenuations are likely the result of wave scattering caused by the fractured rock in the mined areas and the high absorption of the energy of the refracted waves traveling from below the coal layer back through the mined out areas or voids to the geophones at the surface.

Shear wave Results

SIP Models

Depth models (Figure 14 is the north side, and Figure 15 is the south side) were generated through the same process as the P wave depth models. We picked the first breaks on the S wave refraction records and generated travel time curves for both the north and south side profiles (Travel time curves are included as Appendix C).

To gain a general idea of the depth to the refracting interface, the travel time data from shotpoint D, spread A was imported into the refraction interpretation program Refractsolve. The model, which is shown in Appendix D, revealed the source of the refraction energy (indicated by the second interface) to be at a depth of approximately 1.5 m (5 feet). This corresponds to the average depth to the base of the Vanport Limestone, based on the drilling results from ODOT. In this case the source of the shear wave refraction was 1.9 m (6.2 feet) above that of the P wave refraction.

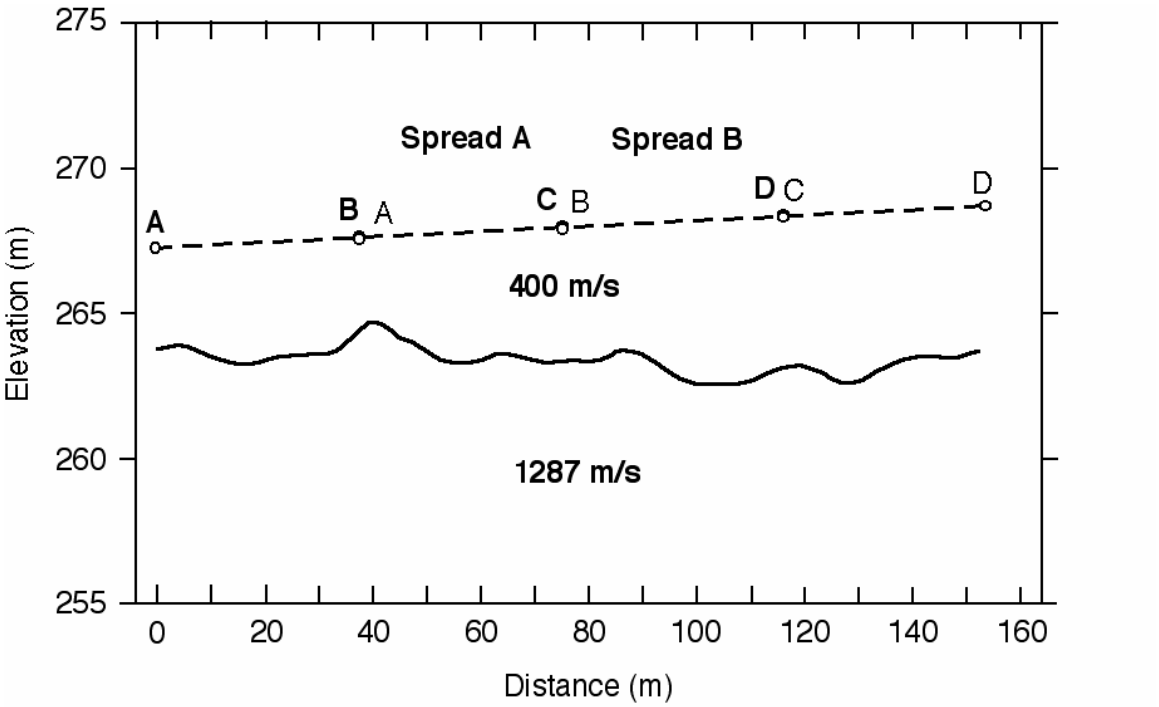

Figure 14. Apparent depth profile along the north side from S-wave seismic refraction

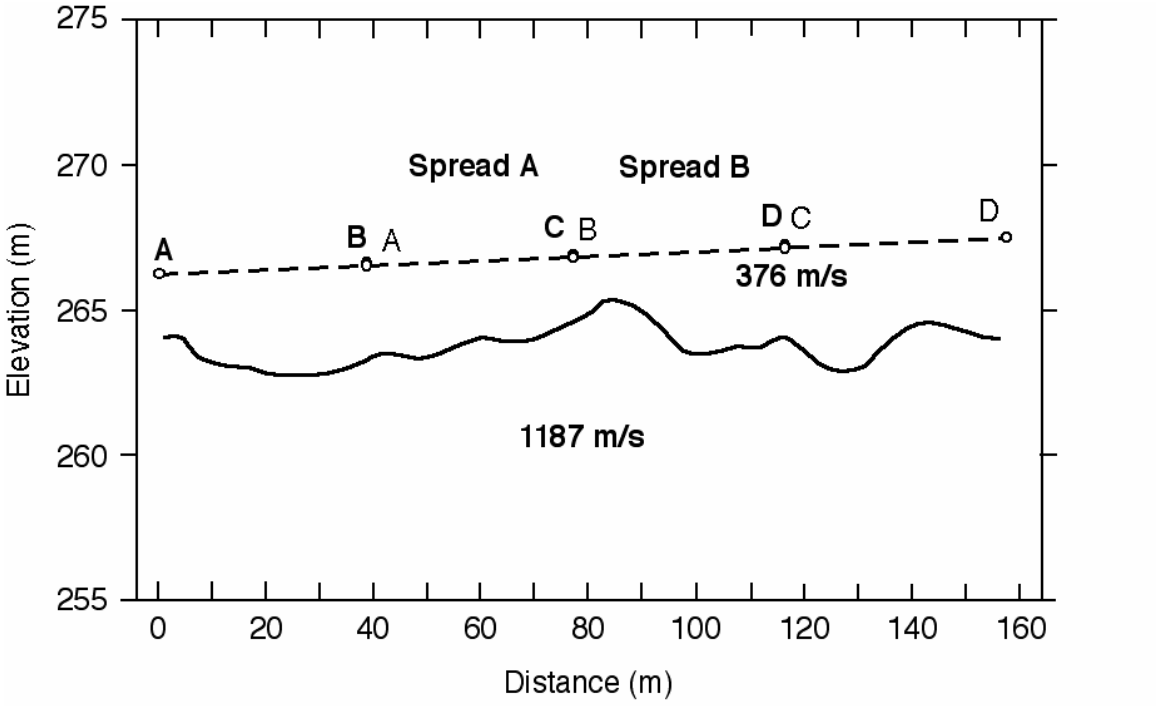

Figure 15. Apparent depth profile along the south side from S-wave seismic refraction

Shear-wave Results

SIP models

Depth models (Figure 14 is the north side, and Figure 15 is the south side) were generated through the same process as the P-wave depth models. We picked the first breaks on the S-wave refraction records and generated travel time curves for both the north and south side profiles (Travel time curves are included as Appendix C).

To gain a general idea of the depth to the refracting interface, the travel time data from shotpoint D, spread A was imported into the refraction interpretation program Refractsolve. The model, which is shown in Appendix D, revealed the source of the refraction energy (indicated by the second interface) to be at a depth of approximately 1.5 m (5 feet). This corresponds to the average depth to the base of the Vanport Limestone, based on the drilling results from ODOT. In this case the source of the shear wave refraction was 1.9 m (6.2 feet) above that of the P-wave refraction.

Once again it should be mentioned that the depth to bedrock shown by the models was most likely representing something other than true depth. The important information is the pattern of peaks and valleys present on the models as a result of the disturbance of the rock layers in the area slowing the wave speed. In both S-wave profiles the depths to bedrock calculated by the program were overall at shallower depths and had a subdued bedrock topography compared with their P-wave counterparts. The peaks present on both profiles are assumed to be representative of the intact portions of bedrock, whereas the dip in depth across the profile or valley patterns are due to incompetent rock above the voids that have slowed the travel times of the refracted rays. There is a subdued correlation between the P-and S-wave depth models and the reason is not clearly understood.

Signal Attenuations

It was initially expected that similar zones of signal attenuation would occur on the S-wave as on the P-wave data, but no distinct zones of signal attenuation were observed in

the S-wave records. Figure 16 shows the S-wave records at the same 2 locations as the previously displayed P wave records in Figure 12.

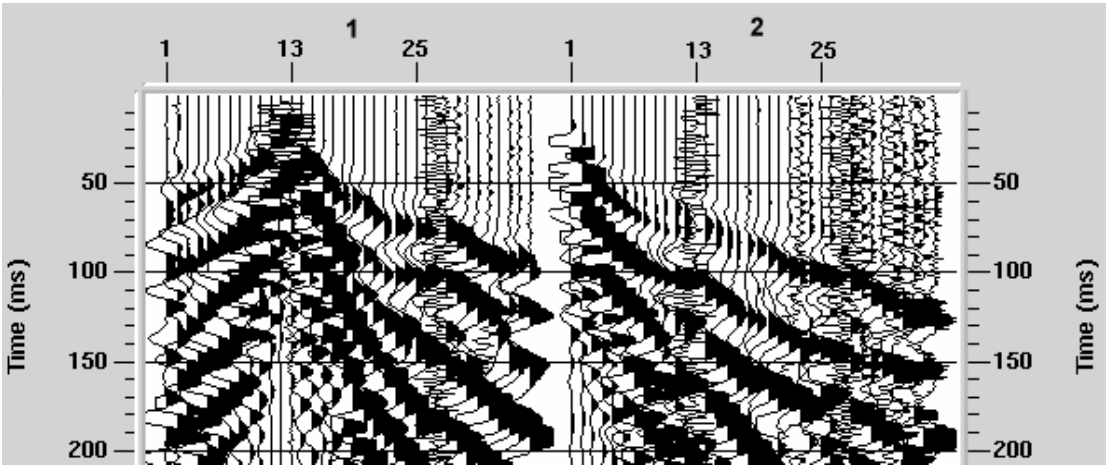

Figure 16. S-wave seismic data records.

Corresponding records had the same geophone and shotpoint geometry. By viewing each record it can be seen that the strength of signal present in the S-wave records remains relatively constant across the spread, in contrast to the P-wave data. The lack of signal attenuation indicates that the S waves did not differentiate as effectively the locations of the mined out areas from areas with coal.

There are three most likely reasons that the known voids in the survey area did not attenuate the signal of the S wave data:

(1) The presence or absence of moisture in the strata below the site will not effect the S wave data but will effect the P wave data, as shear wave velocities are insensitive to moisture content.

(2) The refraction energy for the S waves may be generated in a layer above the coal that is relatively intact and not as fractured as the coal.

(3) The refraction energy for the S waves may be generated in a layer that is too thin for the P wave to effectively propagate.

Resistivity Results

The resistivity data collected at the site were gathered with two different station spacings. The north side of the road had a station spacing of 1.5 m (5 feet), whereas the south side had a station spacing of 3 m (10 feet). Figure 17 shows the apparent resistivity profile and the result of inverting this data to a model for the north side of the road. Figure 18 shows the corresponding results for the south side. There are three parts in each figure. The top section is a pseudosection representation of the measured apparent resistivity. The lowest of the three figures is the 2D model of the true resistivity created by the least-squares inversion technique. The middle figure is the apparent resistivity psuedosection that the model produces. A good fit is when the top and middle figures are very similar. A quantitative measure of the goodness of fit is the RMS error given above the lowest figure. The interpretation is based on the model , i. e., the lowest of the three figures. It can be seen that the depth range on Figure 17 is half that of Figure 18. This is due to the different spacings of the electrodes, 1.5 and 3 m respectively. Both models have two large high resistivity zones that could be due to intact bedrock with unmined coal beds. Overall, the north side profile has better resolution because of the smaller station spacing. Given the near-surface location of the coal, it was expected that the voids present at the site would produce relatively high resistivity values. Without local knowledge of the electrical properties of the mined and unmined zones, it is difficult to identify the mined areas. Fortunately, drilling data were collected by ODOT and using that information it was determined that the high resistivity values are indicative of the coal and the intact bedrock surrounding the mined out areas, whereas the low resistivity values are representative of voids or mined out areas of coal. In general, coal has a large range in resistivity values 1 to 100,00 Ω*m (3 – 300,000 Ω*ft), making it extremely difficult to identify the extent of intact coal on the resistivity section using published values.
In the model resistivity cross sections, areas of intact coal and bedrock are indicated by their higher resistivity values. The typical values of the coal and surrounding bedrock in

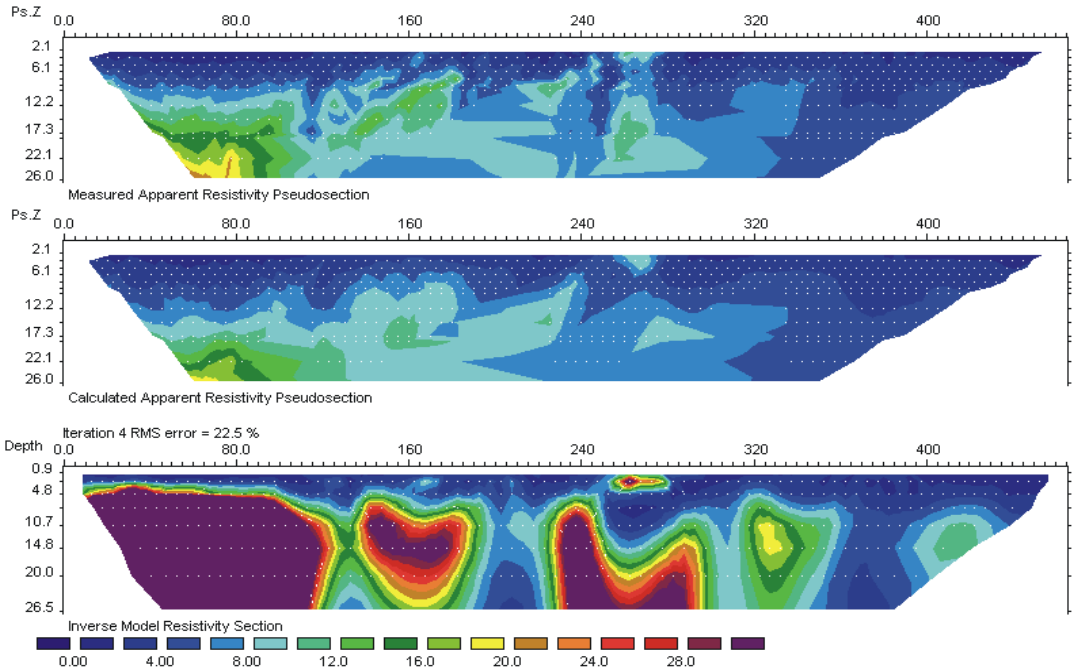

Figure 17. 2D resistivity imaging on the north side. (a) measured apparent resistvity pseudosection. (b) calculated apparent resisitivity pseudosection. (c) Inverse model resistivity section.

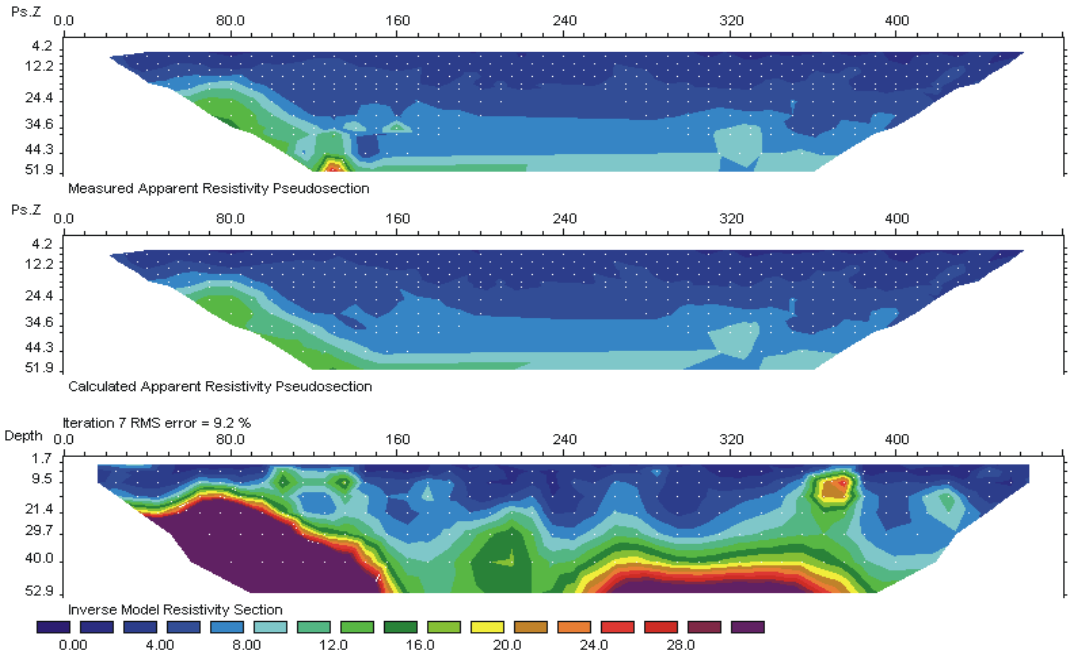

Figure 18. 2D resistivity imaging on the south side.

the model range from 6 to 9 Ω*m (20-30 Ω*ft), whereas the voids' resistivity values range from 0.6 to 5.5 Ω *m (2-18 Ω*ft). The low resistivity values of the mined out areas and voids indicate a high degree of moisture is present within the voids, as air filled voids would yield very high resistivity values.

Gravity Results

The gravity data (Appendix E) collected at the site were corrected for instrument drift as a function of time, and had the free-air and Bouguer corrections applied. The instrument drift from the survey showed a maximum drift of 0.09 milligals, which is acceptable and indicates good quality control. It should be noted that no latitude correction was applied to the data because the maximum north-south range was only 9 m (29 feet). The small latitude effect would be removed when the regional gravity trend was removed. First, a smoothing operation was applied to each gravity stations reading by taking a weighted average with adjacent gravity stations readings to produce a smoothed curve.
The smoothing operation is applied from the following formula:

$$(G_{X-1} * 0.25 + G_X * 0.50 + G_{X+1} * 0.25) = G_{S,X}$$

$G_{S,X}$ = smoothed gravity value at station X

G_{X-1} = gravity reading at station (X-1)

G_X = gravity reading at station X.

G_{X+1} = gravity reading at station (X+1)

The smoothing function is then applied to each station's reading except stations 1 and 48 as there is no station before 1 or after 48. The corrected gravity data can be seen in Figures 19 (north side) and 20 (south side). A regional trend can be observed in the data, sloping from the upper left to lower right, causing the gravity data to look as if it is dipping. The regional gravity was removed from the data by drawing a sloping straight line representing the regional gravity trend and subtracting the gravity value given by this line from the gravity value at each station. The result of removing the regional gravity trend from the data can be seen in Figures 21 (north side) and 22 (south side). The two profiles now appear relatively flat with some noticeable exceptions. The north side

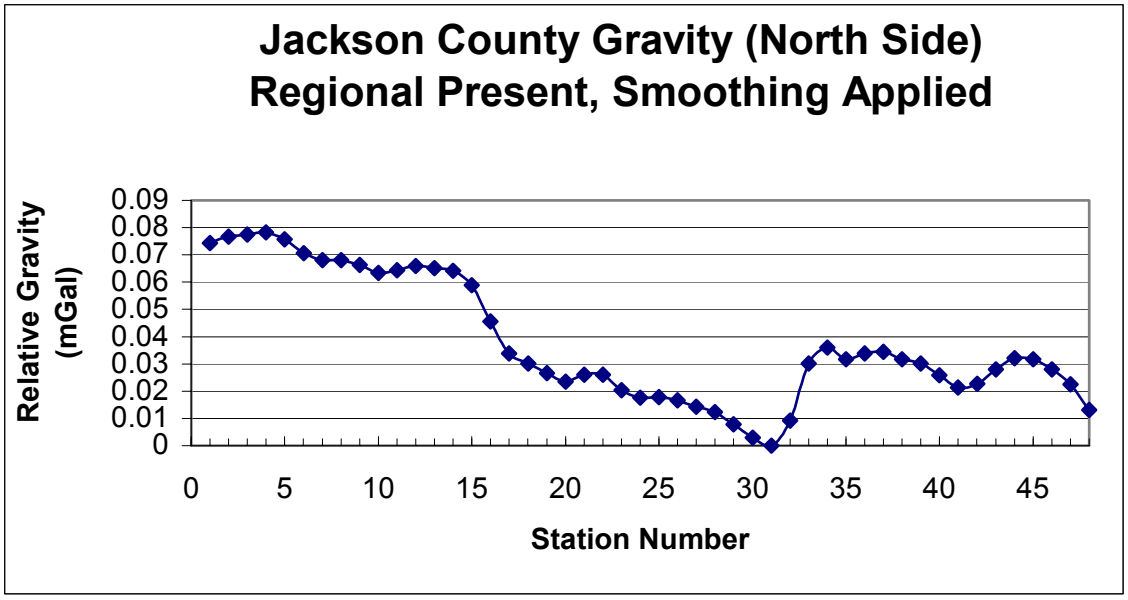

Figure 19. Smoothed gravity data on the north side.

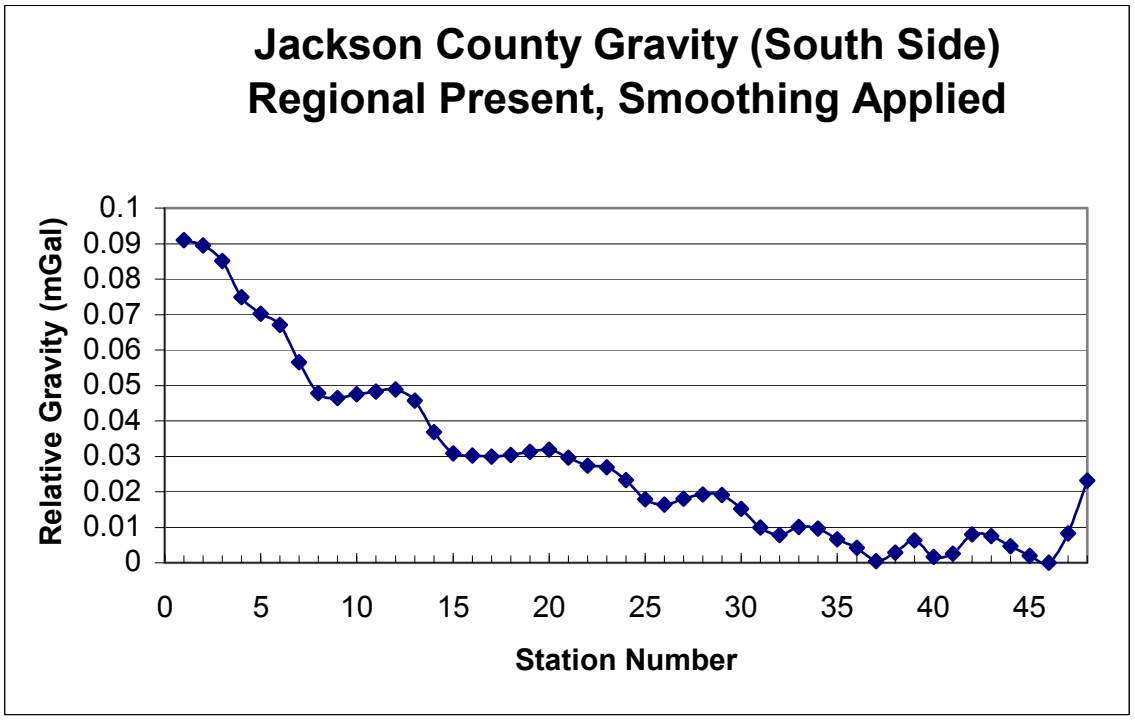

Figure 20. Smoothed gravity data on the south side.

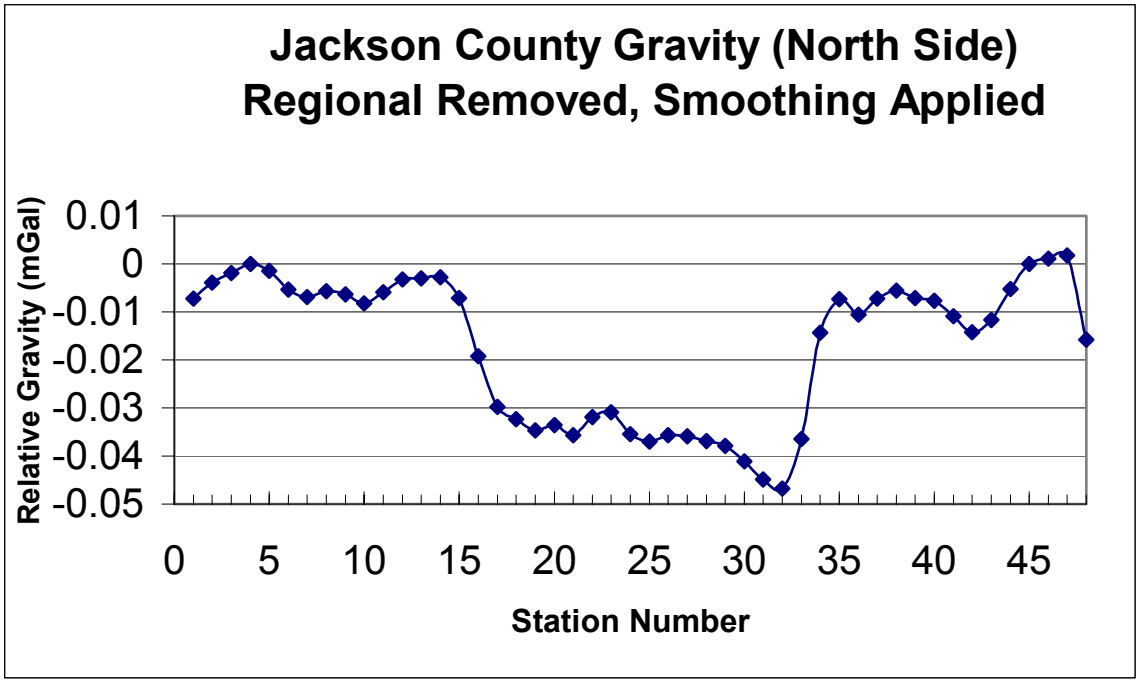

Figure 21. North side gravity profile with regional trend removed.

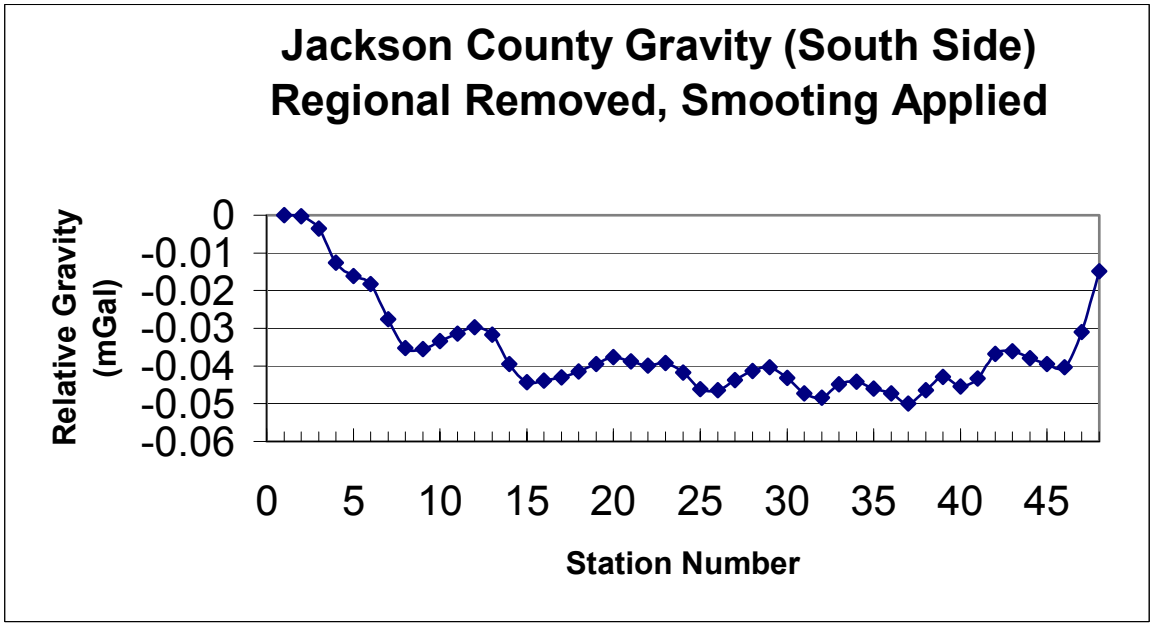

Figure 22. South side gravity profile with regional trend removed

profile shows a gravity low of 0.04 mGals centered in the middle portion of the profile whereas the south side show a gravity low of approximately 0.05 mGals over most of the

profile. Using the observed signal attenuations and drilling results a generalized gravity model of the north (Figure 23) and south sides (Figure 24) was completed using MAGIX XL, by Interprex Limited. Each model has three layers, representing the geology beneath the site and rectangles exhibiting locations of voids found during analysis of geophysical data. The layers have densities of 2.4 (clay), 1.4 (coal) and 2.0 g/cm^3 (sandstone), respectively. The voids have a density value of 1.0 g/cm^3 as it is not known whether they are filled with collapsed roof material or not. The strike direction of the voids are oriented due north, with the profile direction oriented due east. The north side model produced an inverted bell shaped gravity low of 0.03 mGals in the middle of the profile, but the actual gravity data show an abrupt change in readings near the middle of the profile. The abrupt change in gravity readings takes place over 2 stations (16 and 17) where a gravity low is encountered. The gravity low zone continues across the profile until station 32 where the readings increase approximately 0.03 mGals indicating the end of the gravity low detected. The only other notable gravity low can be observed between stations 40 and 45.

The south side model produced a gravity low of 0.03 mGals roughly 0.02 mGals less than recorded in the field data. The trend on the gravity model does not correlate to the profile generated from the collected data. The actual data indicate the presence of a low-density material in the area. The presence of low-density material could have made the density contrast of the known voids in the area very small, making them extremely hard to detect. The low-density material detected could indicate that fill material was used to construct the highway or the voids have collapsed, filling with roof material making their density contrast less and harder to image.

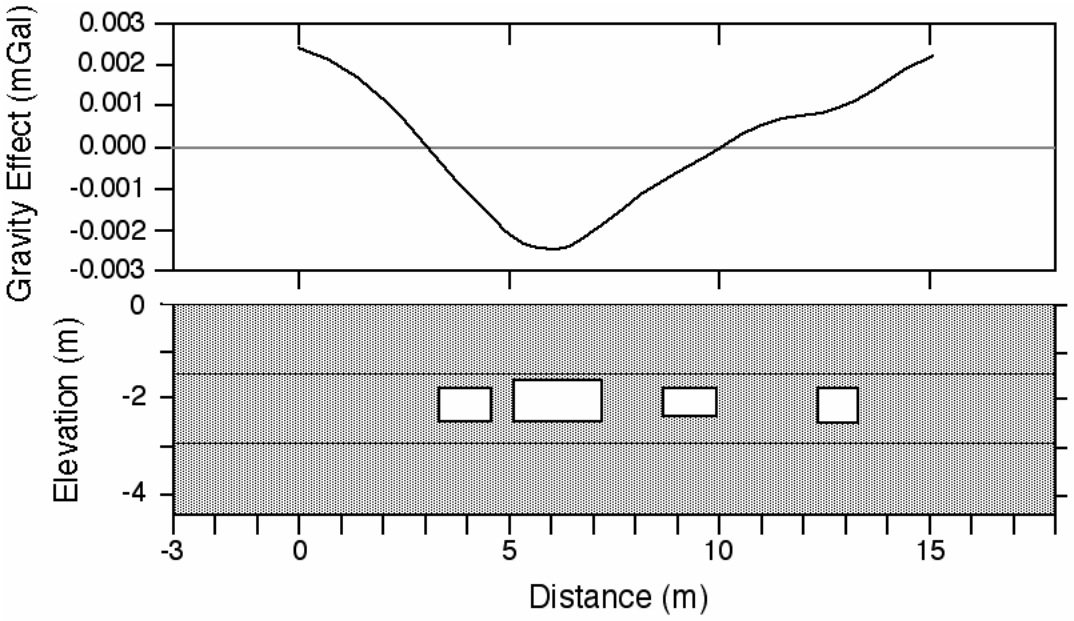

Figure 23. Density model and resulting gravity effect on the north side.

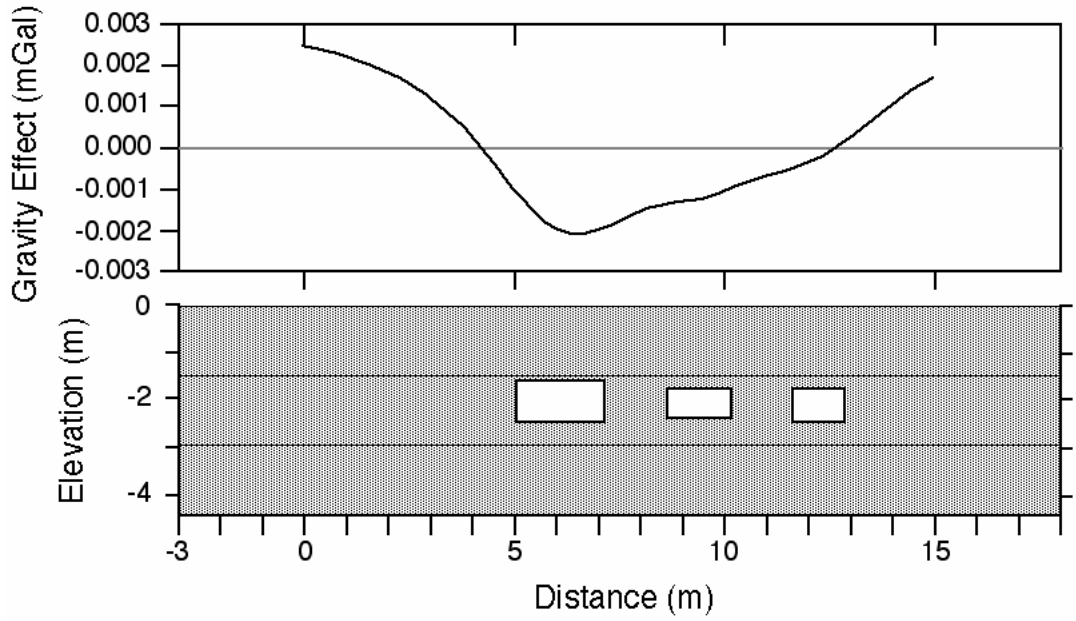

Figure 24. Density model and resulting gravity effect on the south side.

Overall, it is believed that the north side profile did detect some of the voids beneath the site whereas the south side failed to do so. The failure of the south side to detect the voids present beneath the site could be due to the following problems:

1. Lack of sufficient density contrast necessary to detect the voids.
2. The sizes of the voids are smaller on the south side than the north side making them harder to detect.
3. The station spacing was too large to adequately resolve the locations of the smaller voids.

Seismic Reflection Results

Little evidence of voids was revealed by the seismic reflection profiles at the Jackson County site. This was partly due to the extreme shallowness of voids, the spacing of geophones in the survey, and the noise associated with the IVI-minivibe for the closest geophones. Not only did the geophones nearby the vibrator have more spurious engine noise related to the truck-mounted vibrator operation, but these nearby stations are the most important in recording the shallowest reflections before the reflection arrivals merge with refraction energy at farther distances from the energy source. It is possible that for very shallow voids that a smaller and less expensive impact source might prove effective; however, if the depth of potential mine voids is unknown and possibly significantly deeper, the smaller impact or impulsive sources might not have adequate signal penetration. A much closer station spacing than ~3 meters would likely have had a greater chance to image very shallow voids, however, it would have resulted in a significantly greater field effort to profile a given length of roadway at a resulting greater expense. In addition, significant time and effort are involved in processing and analyzing seismic reflection data, which also increases as the station spacing gets smaller and the data volumes get larger. In summary, although one might successfully tune the parameters for seismic reflection profiling at a particular site and potentially image mine voids, it is not likely an economical tool for reconnaissance for voids across large areas.

Ground Penetrating Radar Results

At both sites, the original concerns about radar signal attenuation, resulting in a lack of depth penetration, were confirmed by the tests. The GPR penetration was not significant and reflections from voids were not observed. We tested both 80MHz and 300 MHz antennae, the lower frequency giving the potentially greatest penetration, without indications of subsurface voids in the data. At the Jackson County site the GPR acquisition was also conducted, in part, over a wet ground because a rainstorm terminated the testing. This additional moisture in the clay-rich soil further attenuated the GPR signal and limited penetration. There are conditions where GPR might be used effectively to locate shallow mine voids, but at these clay-rich sites even relatively shallow voids (~3 meters) were not observed.

Surface Wave Results

Sounding Approach

Composite experimental dispersion curves with theoretical fits are shown in Figure 25 for the Jackson site. Resulting shear wave velocity profiles are shown in Figure 26.

Shear wave velocities determined from SASW measurements ranged from 50 m/s, which is appropriate for soft soil, to an imposed maximum of 2200 m/s. The upper-bound shear wave velocity was selected by considering the maximum P-wave velocity measured at the site (2,950 m/s) and a minimum Poisson's ratio that can be considered reasonable for rock (0.1; Goodman, 1980, Table 6.1).

In most cases, interpretation of shear wave velocity profiles was straightforward. However, in one case (Setup E), the composite dispersion curves appeared bifurcated. This was interpreted to indicate that a cavity was likely present. We hypothesized that the cause of this bifurcation is the partitioning of a significant amount of seismic wave energy into a higher-mode response caused by the stiffness contrast presented between the competent host rock and the soft, loose rock surrounding an opening. Of the two

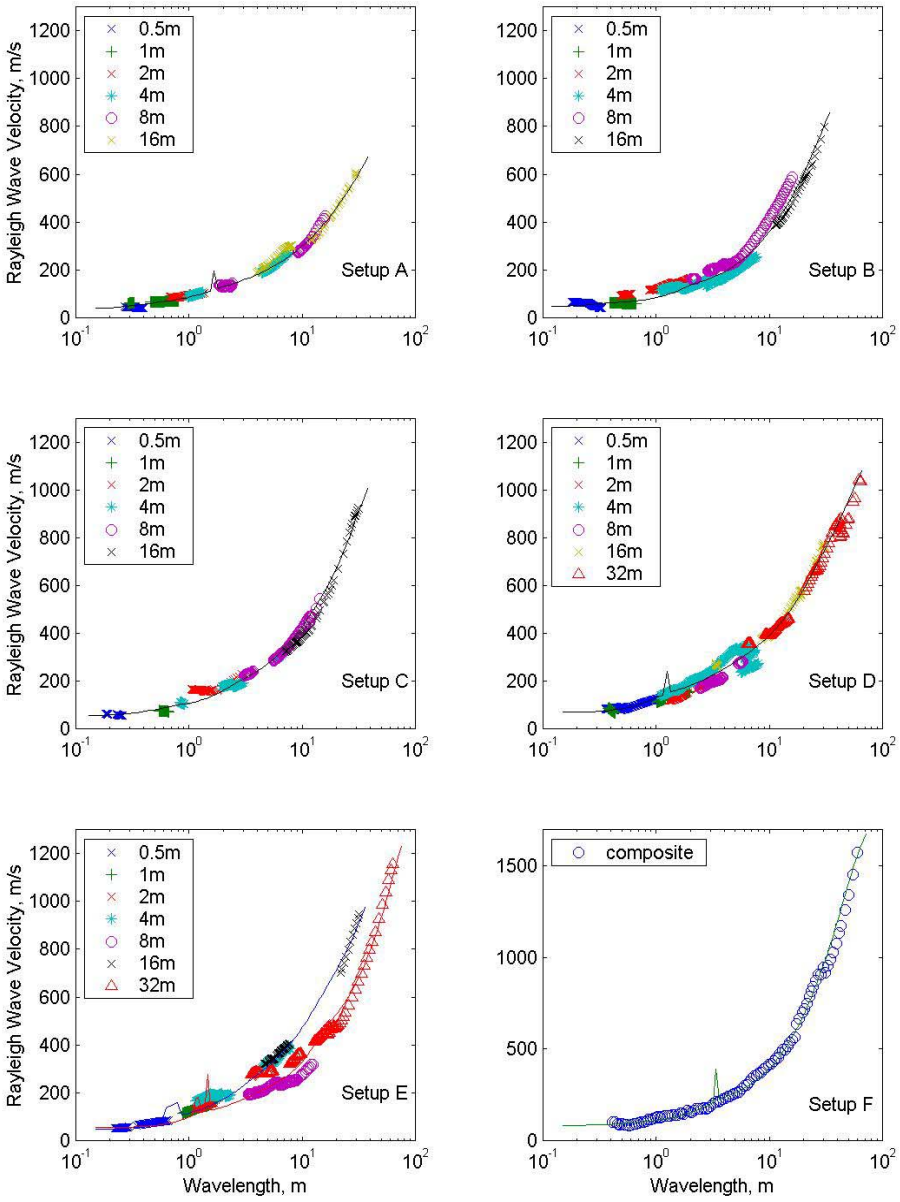

Figure 25. Experimental dispersion curves, with theoretical fits (solid line) for Jackson County site. Different symbols represent SASW measurements at different receiver spacings.

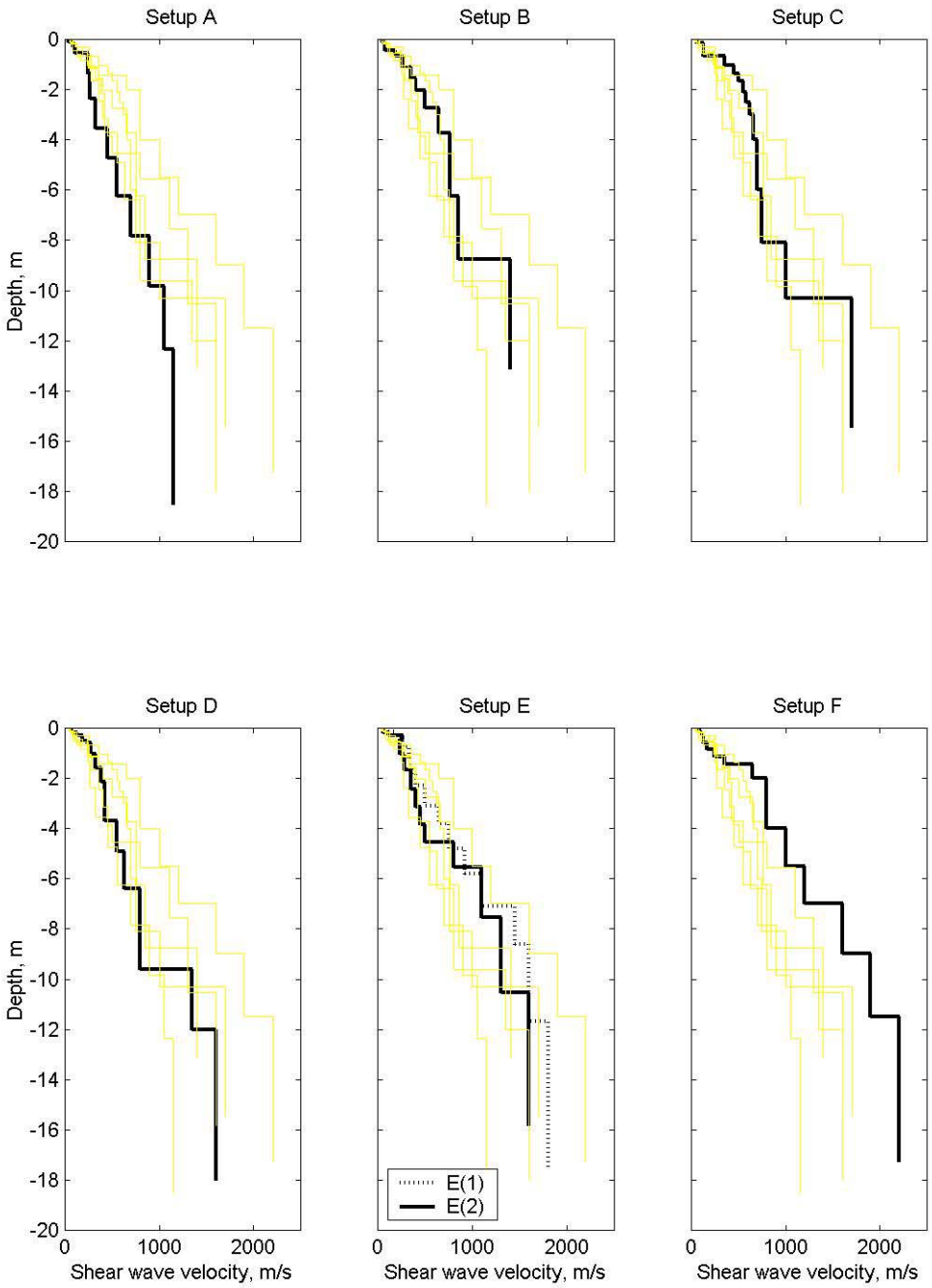

Figure 26. Shear wave velocity profiles for Jackson County site. All profiles are shown, with indicated setup highlighted.

options the lower-velocity solution is the more appropriate for shear wave velocity profiling, since the theoretical model is based on fundamental-mode Rayleigh wave propagation. However, to investigate the difference between solutions for the two forks of the experimental dispersion curves, both were used to develop shear wave velocity profiles.

In most cases, shear wave velocities increased monotonically, and gradually. The shape of the shear wave velocity profile was not diagnostic to indicate the presence of cavities; however, a decreased overall stiffness might be indicative of cavities or loosened zones. To facilitate this comparison, the shear wave velocity profiles (Fig. 26) are shown with others for the same site in the background. At this site, stiffnesses are clearly lower at Setups A and D, and higher at Setup F. Recall that Setup A is over a pavement patch, so the reduced stiffness can be attributed to site disturbance. Setups D and F are at opposite ends of the test section on the shoulder.

Profiling Approach

The unwrapped phase data from the three constant offset measurement arrays are shown in Figure 27. The interpreted anomalies are listed in Table 1, and illustrated in Figure 28. The interpretations presented were developed by Mr. Avar. Dr. Luke performed independent analyses, and reached similar conclusions. Since the interpretation process is subjective, some differences are to be expected. For comparison, anomalies indicated in SASW measurements (discussed earlier) in the same vicinity are also provided in the Table 1.

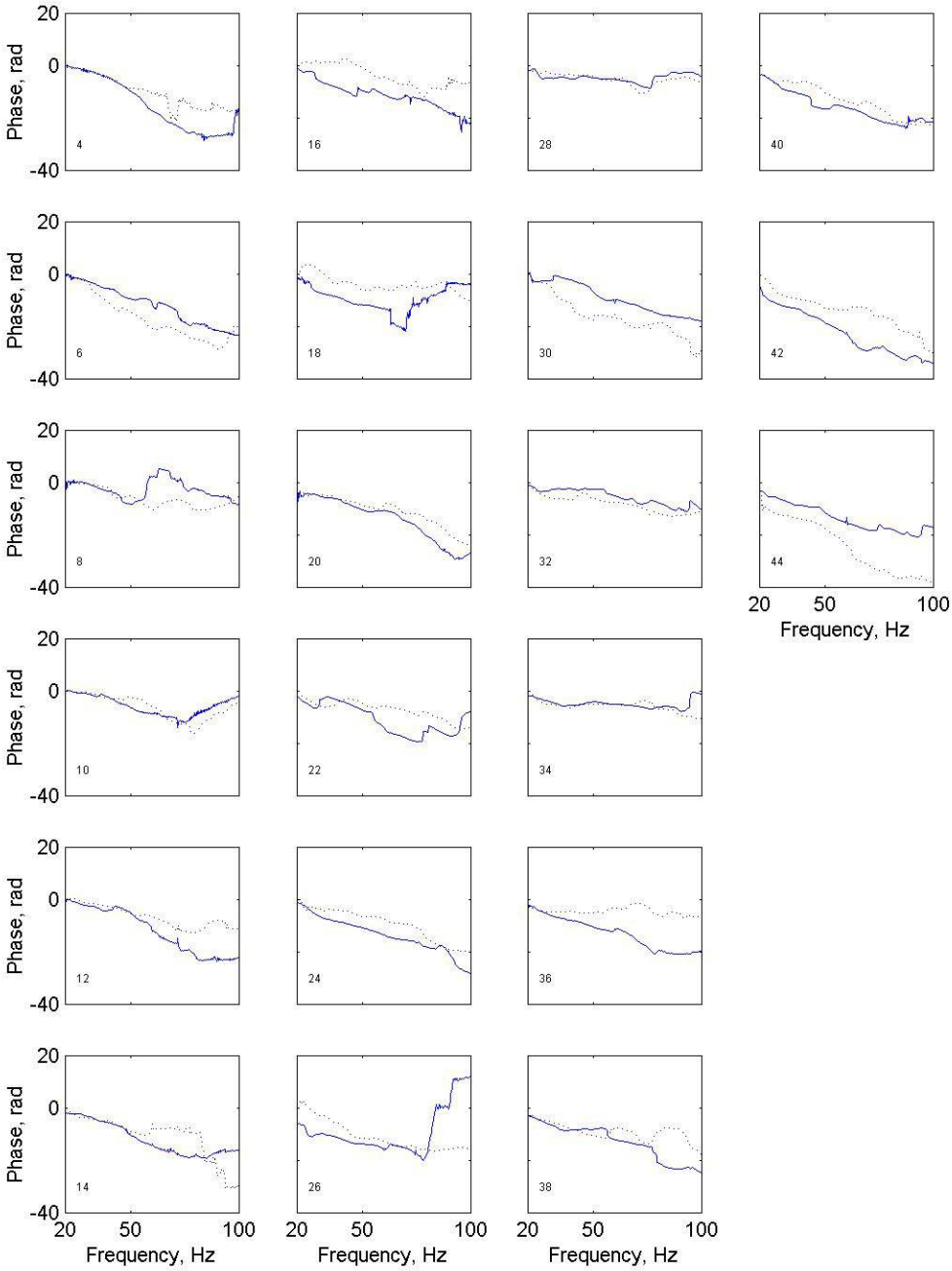

Figure 27. Forward (solid) and reverse (dashed) constant-offset measurements on the shoulder at Jackson County Site (Setup G). Station numbers are indicated.

Table 1. Seismic anomalies determined by surface wave measurements. Rankings are *0* for none, *1* for slight, and *2* for significant. [Profiling was advanced in two station increments. The three SASW surveys were centered at the stations with table entries.]

Jackson County Site – Shoulder Seismic Anomaly Ranking		
WSU Station No.	**Profiling (Setup G)**	**SASW**
4	*1*	*0*
6	*2*	
8	*1*	
10	*0*	
12	*1*	
14	*1*	
16	*2*	
18	*2*	
20	*0*	
22	*1*	
24	*1*	*1*
26	*2*	
28	*0*	
30	*2*	
32	*0*	
34	*0*	
36	*2*	
38	*1*	
40	*2*	
42	*2*	
44	*1*	
46		*2*

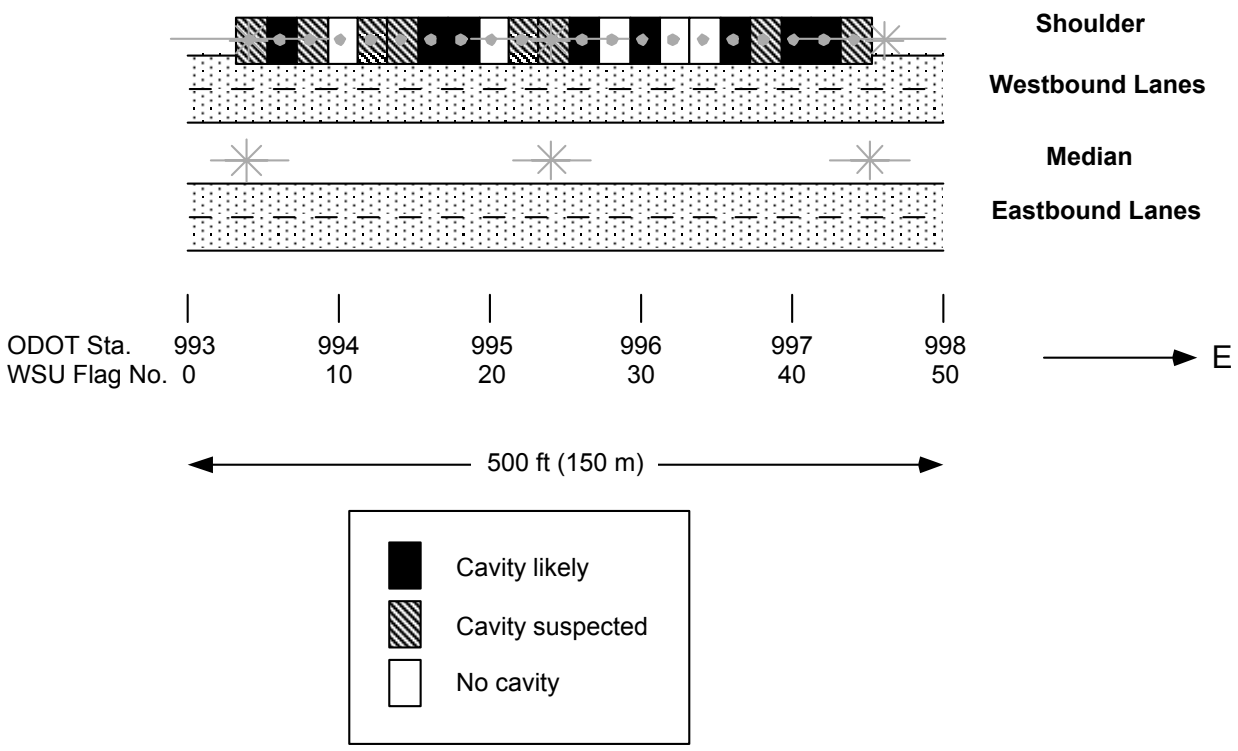

Figure 28. Suspected anomalies indicated by constant-offset measurements for Jackson County site.

Ground Truth and Data Comparison

Upon the completion of the geophysical surveys, we supplied ODOT with locations for borings to test the accuracy of the geophysical interpretations. The results obtained from these borings were compared to the geophysical interpretations and the effectivenesses of the various techniques employed herein were evaluated. As a consequence of the numerous voids encountered during the series of borings, ODOT decided that the road was in danger of collapse, closed the road, and performed extensive excavation and rebuilding. The excavation provided a detailed view of the coal mines. No detailed, surveyed maps were made of the exposed mine tunnels. Rick Ruegsegger of ODOT constructed a map (Figure 29) from his observations of the tunnels during periodic visits to the site. He extrapolated additional tunnel locations based on the anticipated pattern for areas not exposed. The map he drew from his interpretation of his observations is a valuable check on the geophysical results. Although the map may not be quantitatively

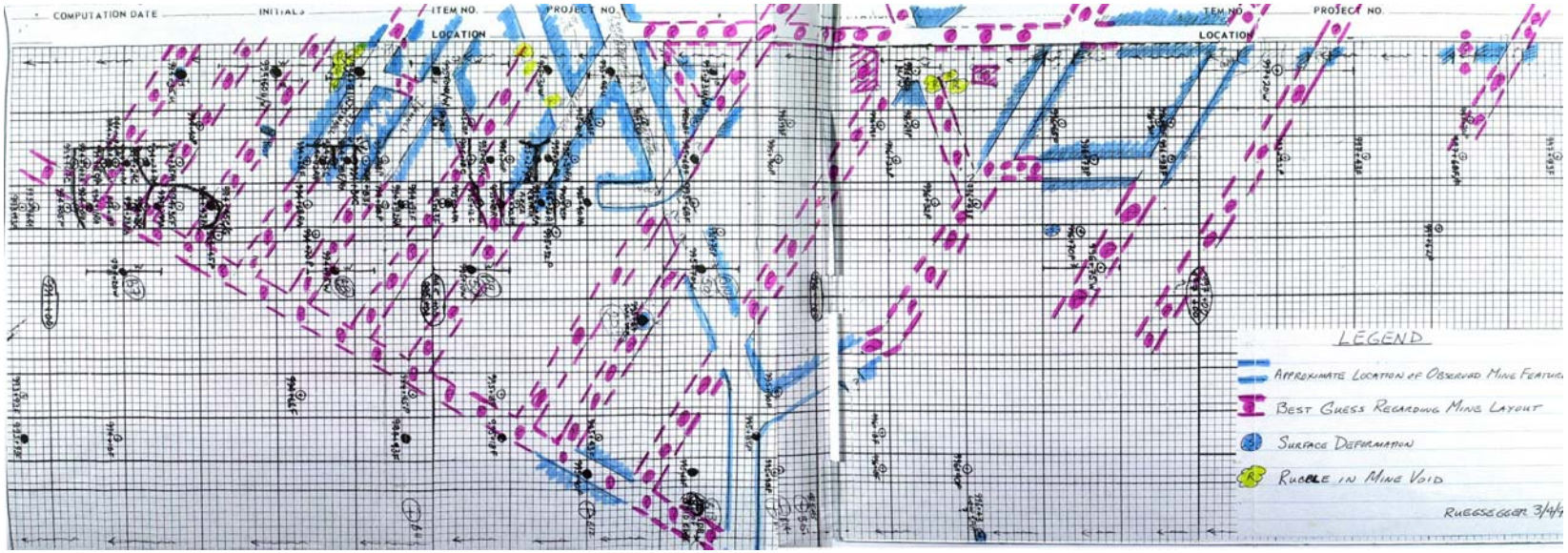

Figure 29. Sketch map of the mine workings interpreted by R. Ruegsegger, ODOT, from his observations at the excavation.

correct, it provides strong guidance for the interpretation The map prepared by Mr. Ruegsegger is an invaluable qualitative source for calibrating the geophysical data interpretation.

The resistivity, P- and S-wave refraction travel time delays, and P-wave signal attenuations correlated well with the known locations of voids determined by the ODOT drilling data. The gravity data produced questionable results, in that only the north side profile produced gravity lows associated with the voids present below the site. Locations of low resistivity values correlated well to locations of P wave signal attenuation. The zones of signal attenuation correlated well with the greater apparent depths to the refraction interface shown on the depth models. The P wave data showed this better than the S wave data did.

Seismic surface wave profiling results compare reasonably well with the excavation results. Some anomalies identified as potential cavities that do not correlate with the excavation results may be due to scattering from discontinuous limestone blocks near the top of bedrock. SASW did not provide adequate resolution to clearly delineate cavities. The seismic reflection and GPR produced no positive results. Figure 30 shows a composite map of (a) gravity, (b) resistivity, (c-e) P and S wave seismic refraction, and (f) surface wave profiling on the north side of the road. Locations of the mine tunnels, approximated from Ruegsegger's map of the excavation, are shown at the bottom of each page of the Figure 30(g).

The P-and S-wave depth models were expected to resemble one another, but in this case they do not. There are two possible explanations for this:

(1) The percent void space present has affected the velocity of the P waves slowing them down, but has had no effect on the S waves.

(2) The refraction for the P wave survey came from below the coal, whereas the S wave refraction came from above the coal.

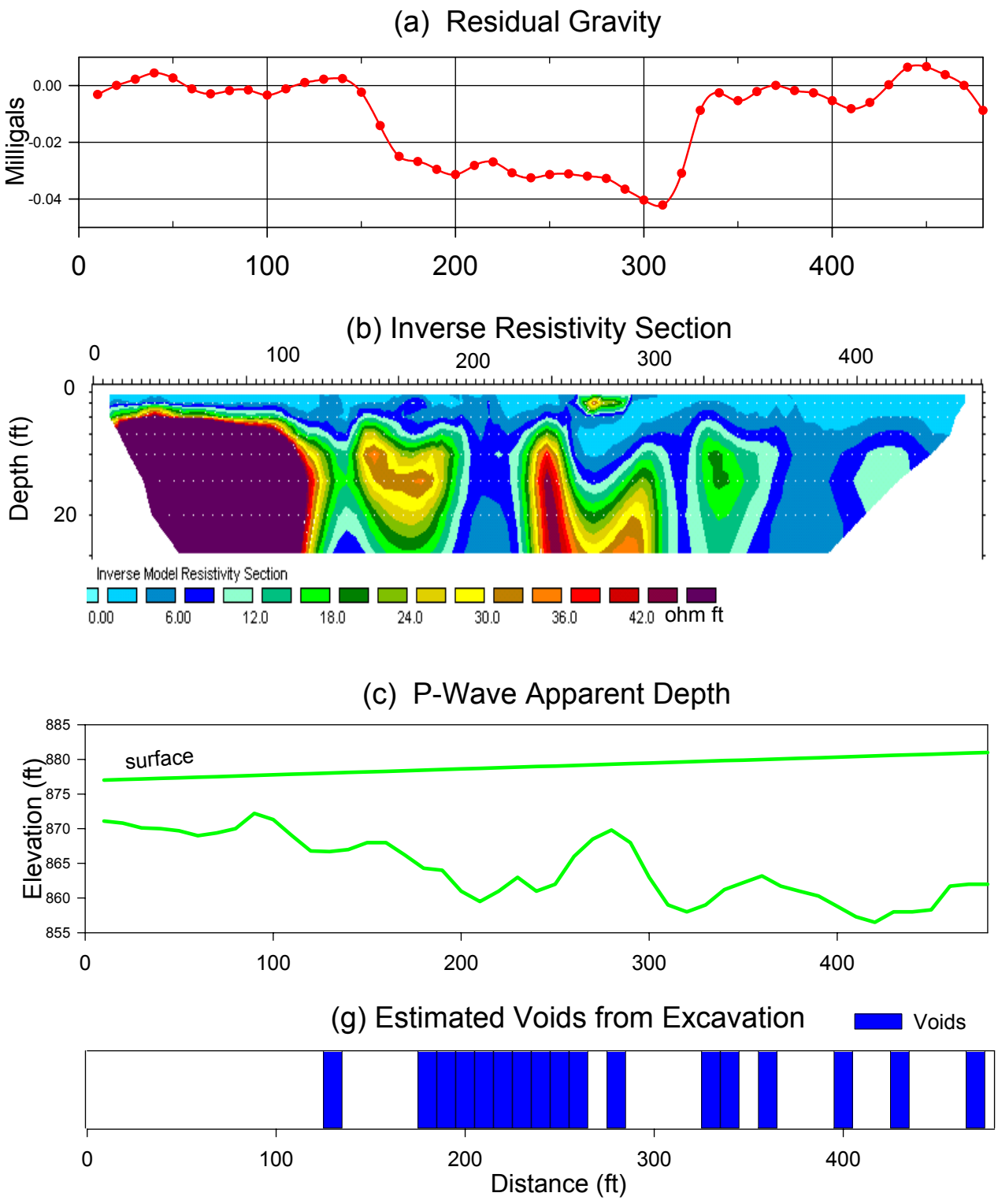

Figure 30, Part1. Composite of results and interpretation on the North side. a) Residual Gravity, b) Inverse resistivity section, c) P-wave apparent depth, and g) Boring and excavation interpretation.

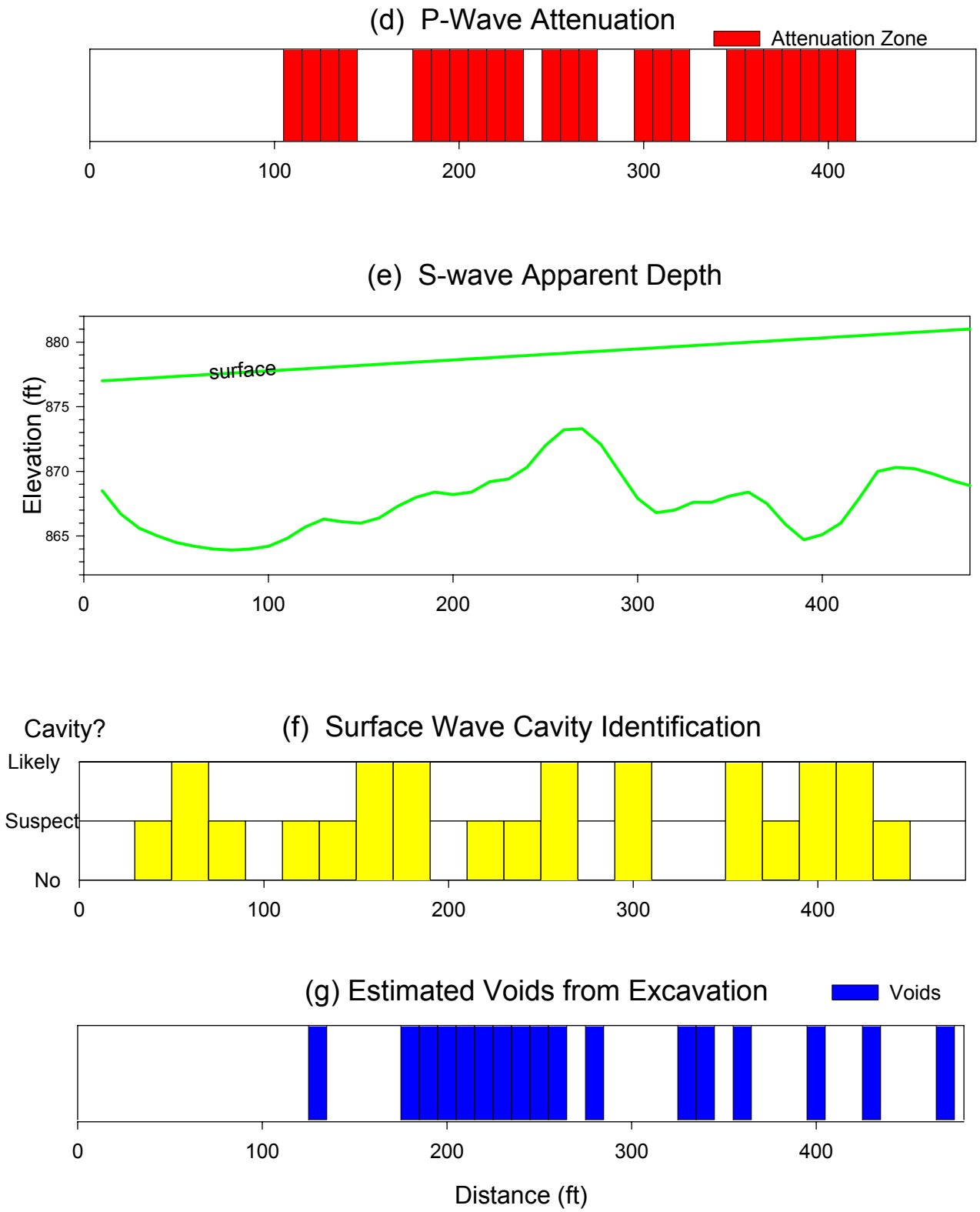

Figure 30, Part 2. Composite of results and interpretation on the North side.
d) P-wave attenuation, e) S-wave apparent depth, f) Surface-wave cavity identification,
g) Boring and excavation interpretation.

Given the presence of moisture within the voids from the resistivity data, it is believed that the refraction surface in the P wave survey came from the base of the coal. The source of the S wave refraction appeared to be above the coal and it is currently not understood why this is. The increased presence of voids would greatly slow the velocity of the P wave data in the vicinity of the void areas, whereas the S waves would not be effected, which would account for the subdued topography present on the S wave depth model.

The gravity data collected on the north side of the road correlated fairly well with the known location of the beginning of voids along the west end of the profile but did not correlate well on the east end. The broad gravity low detected in the middle of the profile is likely due to a series of voids present between stations 15-33. The only other low present on the profile is centered on station 40 and is likely the result of a void known to exist at that location. The south side's gravity model shows a broad gravity low across the entire profile. The lack of any distinct gravity anomalies indicates that the voids were not detected. There are three possible explanations for this:

(1) The gravity low across the profile suggests that the mine tunnels may be collapsed. The collapse of roof material into the mine tunnels would make the density contrast of the tunnels small and hard to detect in an area where a gravity low already exists.

(2) The station spacing used in the survey may have been too large to detect the voids.

(3) The gravity anomaly produced by the voids may have been obscured by the presence of a low-density fill material used to construct the highway.

d. Conclusions from Phase I and Recommendations for Phase II

Several geophysical methods were employed to acquire data for the purpose of locating voids or potential collapse features at the field site in Jackson County, Ohio. The broader goal is to determine which techniques efficiently define the subsurface beneath such sites. The methods consisted of P and S wave seismic refraction, resistivity, gravity, surface wave profiling, spectral analysis of surface waves, seismic reflection, and ground penetrating radar. The first 3 methods produced favorable results, gravity showed effects less clearly, surface wave profiling produced encouraging results, while spectral ananysis of surface waves, seismic reflection, and ground penetrating radar were ineffective at this site.

The resistivity, the P-, and S-wave seismic data accurately detected the voids and intact portions of coal present beneath the site. Two station spacings were used in the collection of the resistivity data, 1.5 m (5 ft) and 3 m (10 ft). The 1.5-m station spacing used to collect the north side's resistivity data displayed a better resolution of the subsurface and should be used in future investigations. Although the seismic data detected the voids at the site, changing the station spacing to 1.5 m would increase the resolution of the data, and better define the void locations. The gravity surveys were expected to be marginal for detecting voids at this site because of their low-density contrast. It was rather surprising that the north side profile did detect the voids. Site investigation by surface wave sounding provided stiffness profiles at discrete points and established the variability of stiffness in intact and weakened zones. Complex dispersion characteristics appear to be indicative of the presence of cavities; however, the limited lateral resolution and the data acquisistion time suggest that it is not likely to be a useful technique for tunnel detection. The profiling method indicated potential cavities at the site. This method is much more efficient than sounding for covering large areas.

Future studies having similar goals of locating near-surface potential collapse features should use resistivity and P and S wave seismic refraction, because these methods

accurately detected the voids, data can be acquired relatively quickly and they are relatively inexpensive. The recommendations to be made that would increase the quality of the data would be:

(1) Make the station spacing of the resistivity and geophone positions 1.5 m. The smaller station spacing would give the data a better resolution of the subsurface.

(2) Know the subsurface geology of the area prior to conducting the survey to insure you can get the desired results from each method used.

The surface wave profiling method is recommended to detect shallow mine-related cavities beneath highway sections. In order to cover long distances, both the data collection and interpretation processes could be automated. Where unexpected, abrupt changes in conditions are encountered in profiling mode, the sounding method might be applied for better understanding of the subsurface profile.

B. Vinton County Site – Phase I

The test site is along Ohio Route 32, 700 feet west of the Racoon Creek Bridge (Figure 1). Data were collected on the north side of the road and in the median. Geophysical methods employed consisted of seismic refraction, seismic reflection, seismic surface wave profiling, SASW, 2D-resistivity imaging, gravity and GPR. These were the same methods that were used at the Jackson County site.

a. Geology and Data Acquisition

The Vinton County site had similar geology to the Jackson County site but it is more highly variable as seen in the ODNR drilling logs. In this area, five boreholes had been previously drilled. One boring at the eastern end, closest to the highway bridge, encountered air-filled voids at depths of 5.4 to 6 m (18 to 20 ft) and 6.3 to 7.8 m (21 to 26 ft), with a total vertical void height of 2.1 m (7 ft). Three other borings drilled on the shoulder yielded profiles consisting of silty sand, followed by sandstone, then limestone, and shale. The coal seam was encountered in only one of the borings. A borehole in the median penetrated 4.5 m (15 ft) of fill material, followed by clay. None of the borings encountered any groundwater.

The seismic refraction and 2D-resistivity imaging were determined to be the most successful techniques based on our previous experience at the Jac kson County site. Therefore we primarily focused on these methods to assess the Vinton County site. The data acquisition methods and parameters were the same as at the previous site, unless noted otherwise. For seismic surface wave acquisition, two arrays were positioned at the site, one on the north shoulder, and the other in the median. Arrays were marked with flags placed at a 3.0-m (10- ft) interval. The station numbers referenced in this study were collocated with the flags. The Vinton County test strip is 240 m (800 ft) in length and abuts a bridge (Figure 31).

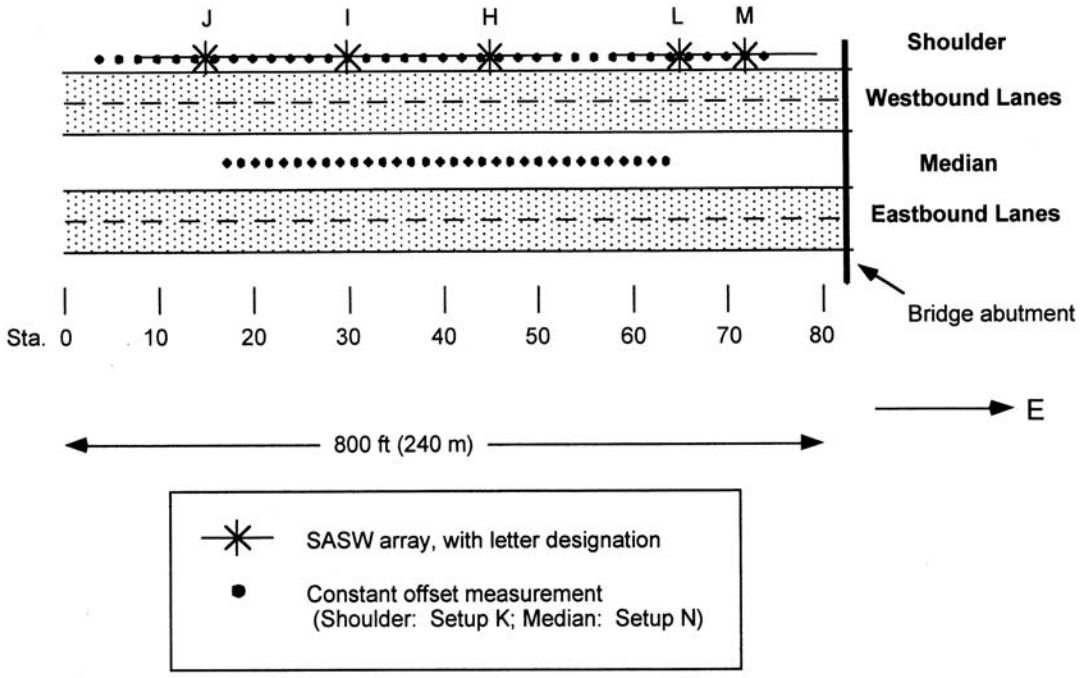

Figure 31. Diagram of the Vinton County test site with station numbers and surface wave test locations.

b. Results

For both the median and north berm sites the P- and S-wave models do not correspond to the bedrock depth. When compared to borehole data the S-wave models seem to more

accurately reflect depth to bedrock. The general trend of the survey site is that bedrock shallows from west to east. According to the S-wave models (Figs.32 and 33) the minimum depth to bedrock is 1.2 m (4 feet) below the north berm and 1 m (3 feet) below the median. P-wave models (Figs. 34 and 35) show the minimum depth to bedrock to be approximately 2.7 m (9 feet) below the surface at both locations. At the western end of the line, S-wave models indicate that bedrock depth drops to 12 m (40 feet) below the surface at the median and 16 m (54 feet) below the north berm. P-wave models show significantly shallower occurrences of bedrock of 7.9 m (26 feet) below the median and 10.6 m (35 feet) below the north berm. No evidence of collapse or problem zones is apparent.

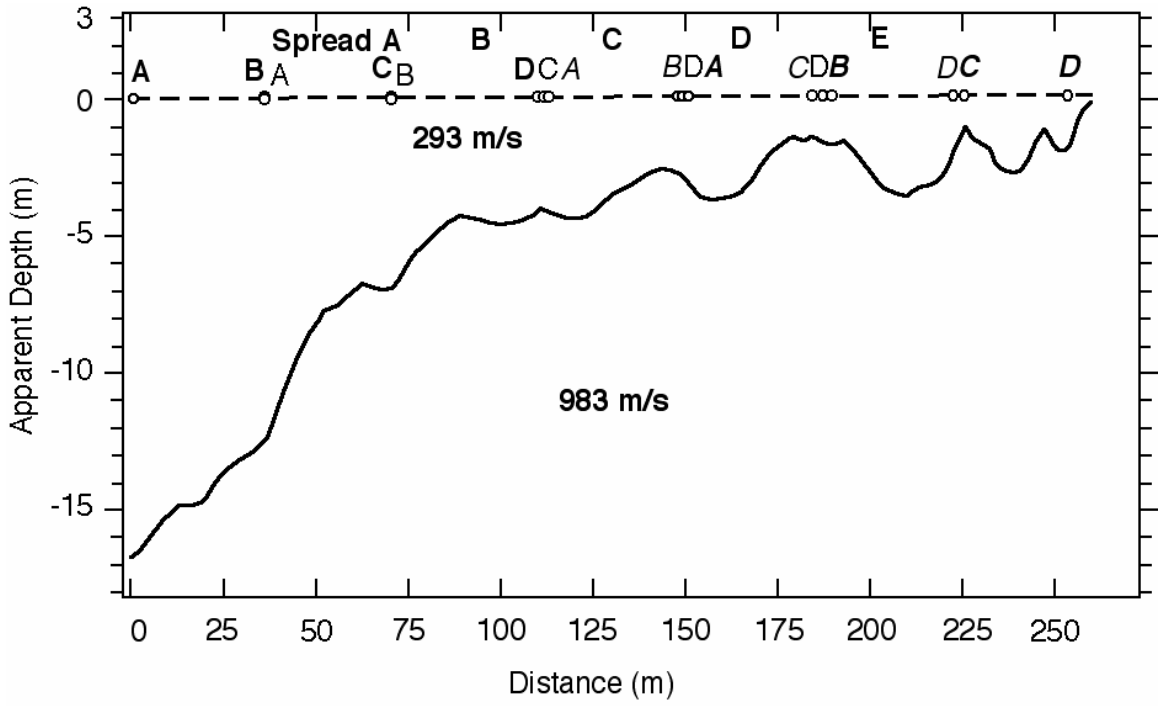

Figure 32. Apparent depth to bedrock from S-wave seismic refraction on the north side of Vinton County site.

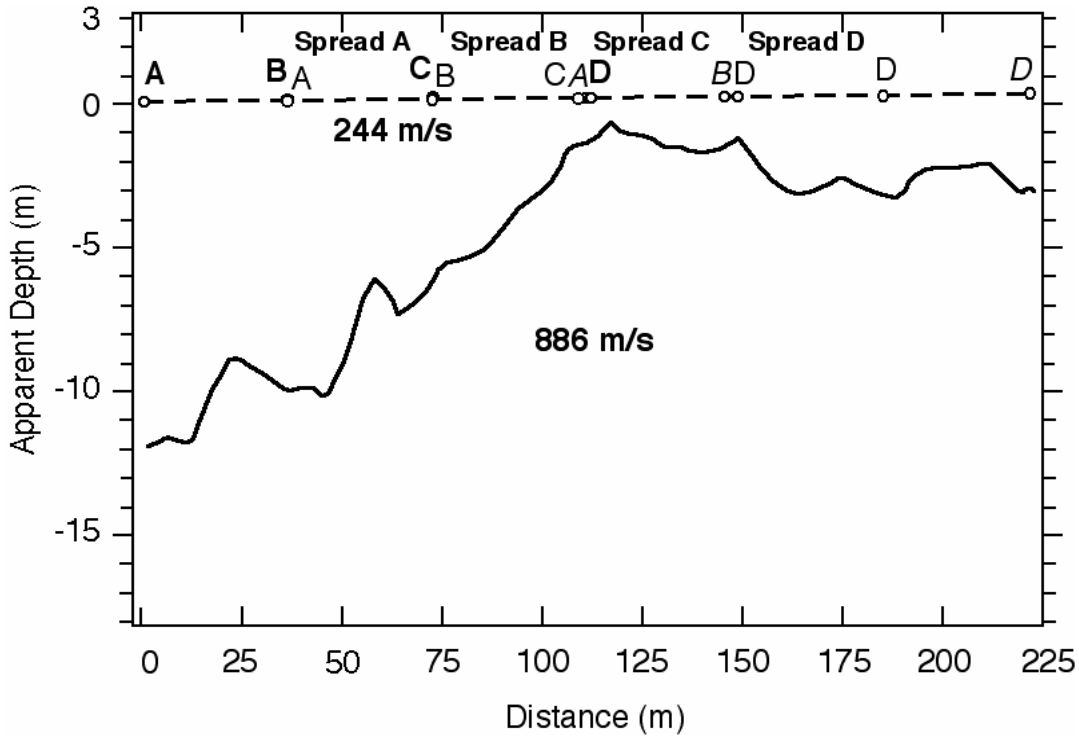

Figure 33. Apparent depth to bedrock from S-wave seismic refraction in the median at the Vinton County site.

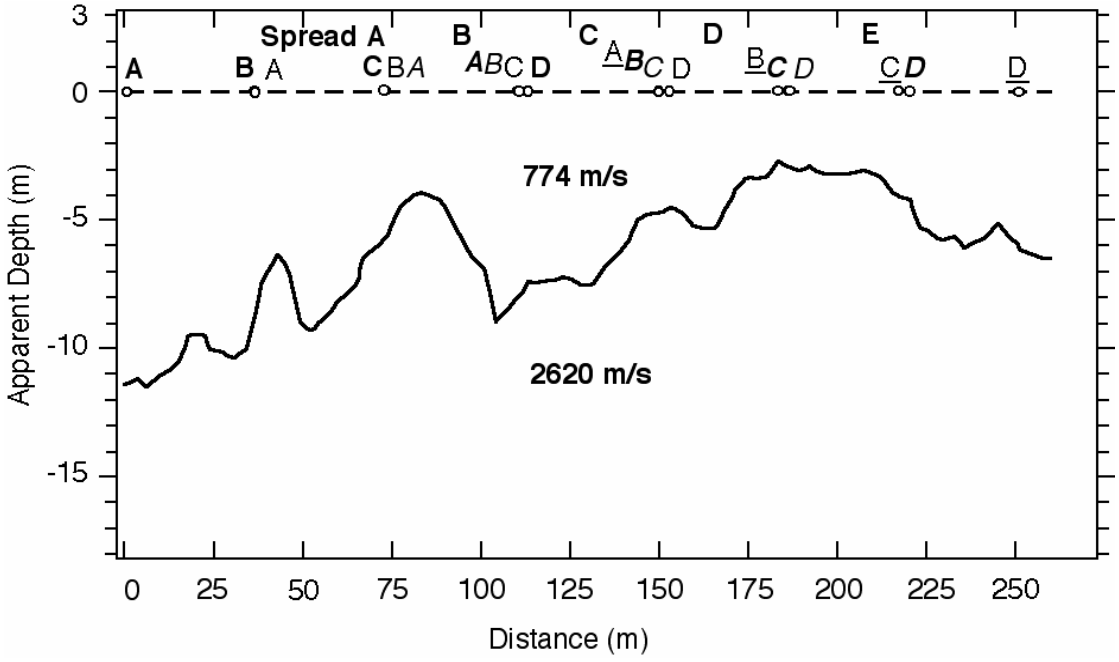

Figure 34. Apparent depth to bedrock from P-wave seismic refraction on the north side at the Vinton County site.

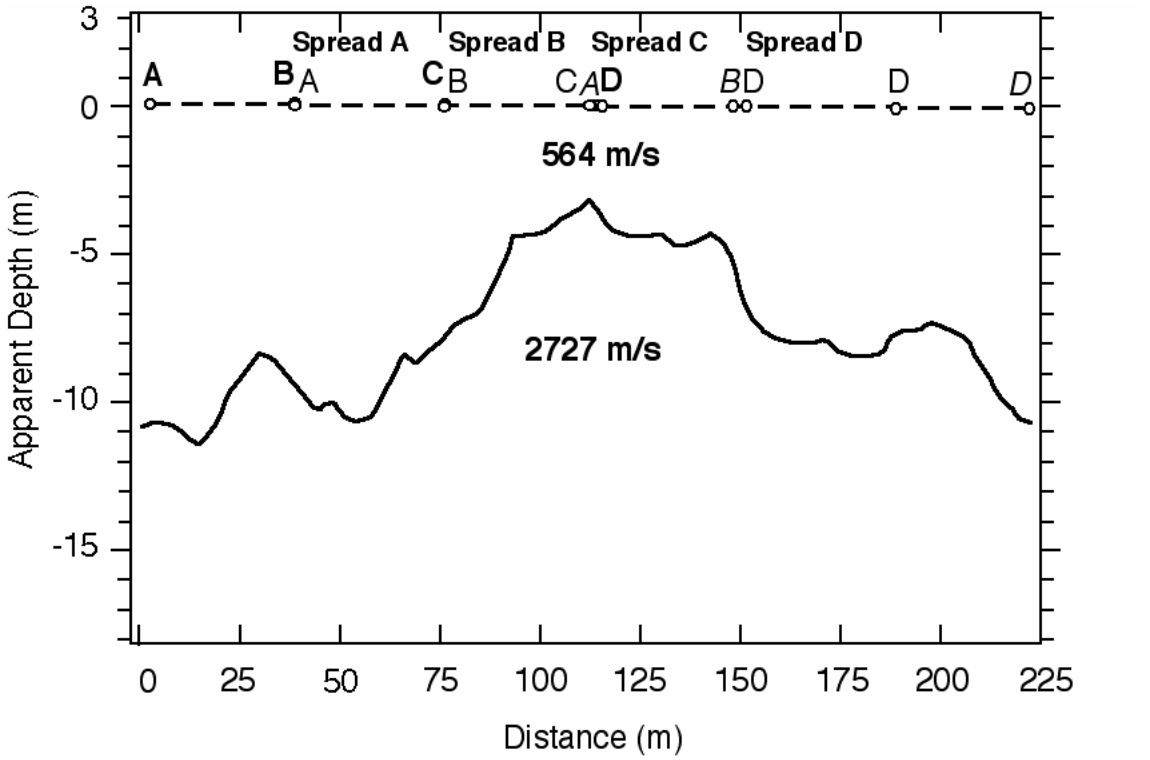

Figure 35. Apparent depth to bedrock from P-wave seismic refraction in the median at Vinton County site.

At this location the shallow mines are expected to be air filled, thus producing a higher resistivity than the surrounding rock material. Resistivity below the median (Fig.36a) is low, averaging 1.8 to 6 Ω*m (6 to 20 Ω*ft). There are no indications of prior mining activity at this location. Resistivity along the north berm (Fig.36b) is also low, averaging 4.9 Ω*m (16 Ω*ft). One apparent anomaly is present at survey location 152 to 183 m (500 to 600 feet) [133+22.5 to 134+23.8] along the survey line. This anomaly has an average apparent resistivity value of 30 Ω*m (100 Ω*ft) at a depth of 8.8 m (29 feet). This does correspond to nearby mining locations indicated by a map supplied by ODOT. The depth of this void is roughly equivalent to the void encountered in borehole B1. Gravity data at the median location (Fig.37) follows the same bedrock trend as seen in the refraction models, bedrock shallows from west to east. No evidence of mining is apparent. Gravity data from the berm location (Fig. 38) shows a gravity high at the

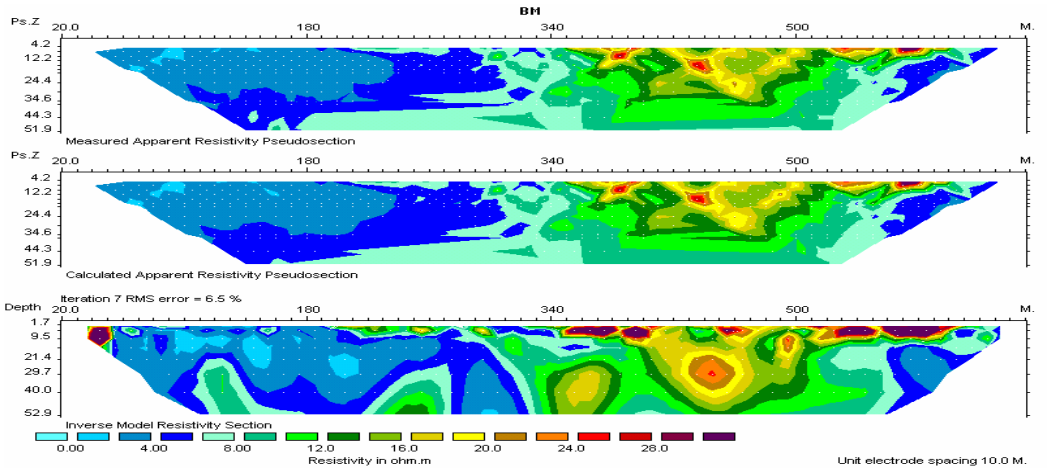

(a) Median

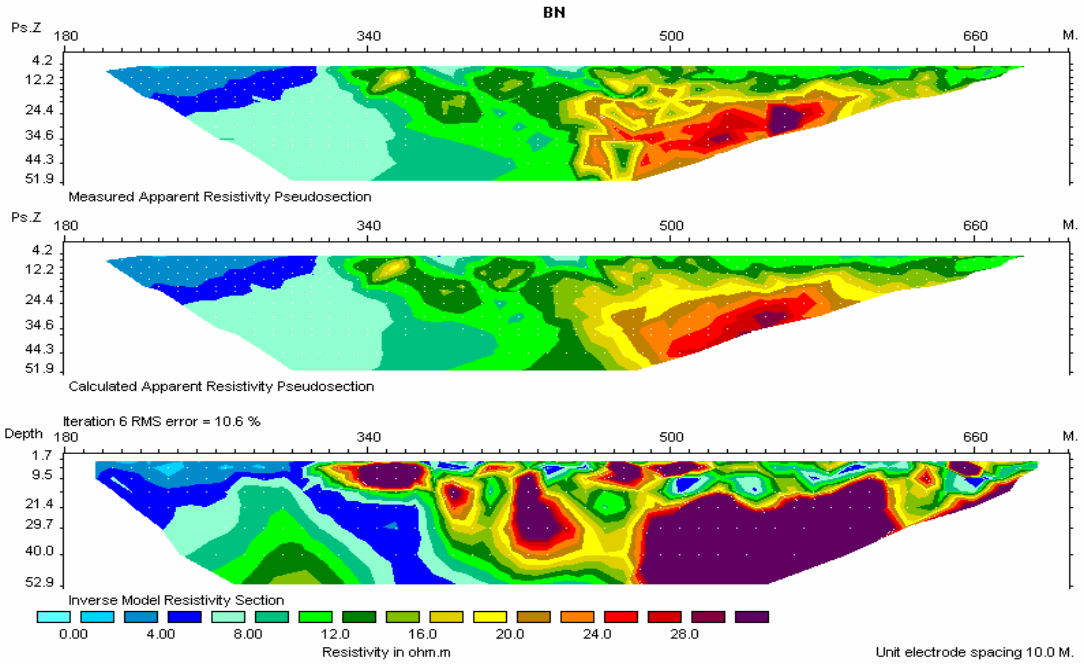

(b) North berm

Figure 36. 2D resistivity imaging of the Vinton County site. (a) median, (b) north side.
Top: measured apparent resistvity pseudosection.
Middle: calculated apparent resisitivity pseudosection.
Bottom: Inverse model resistivity section.

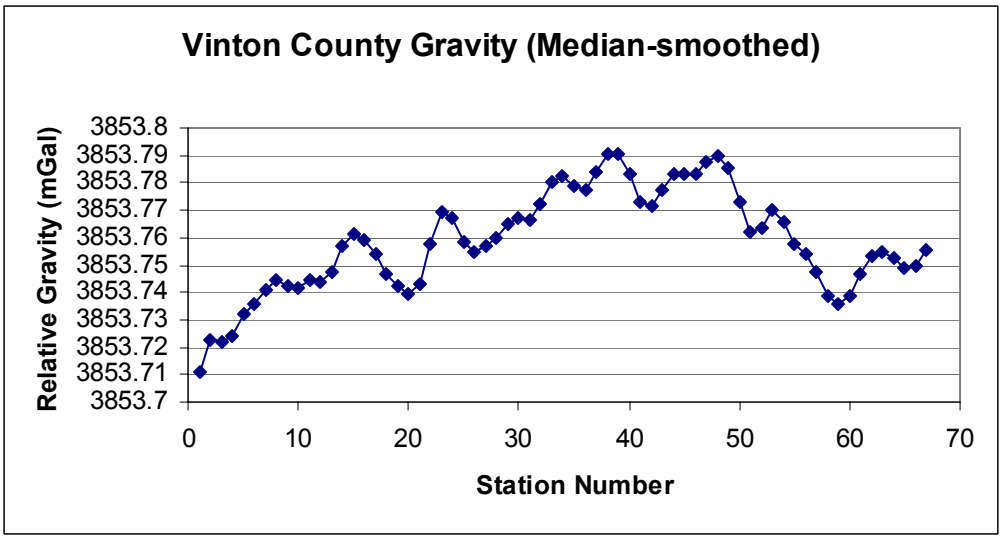

Figure 37. Smoothed gravity profile along the median.

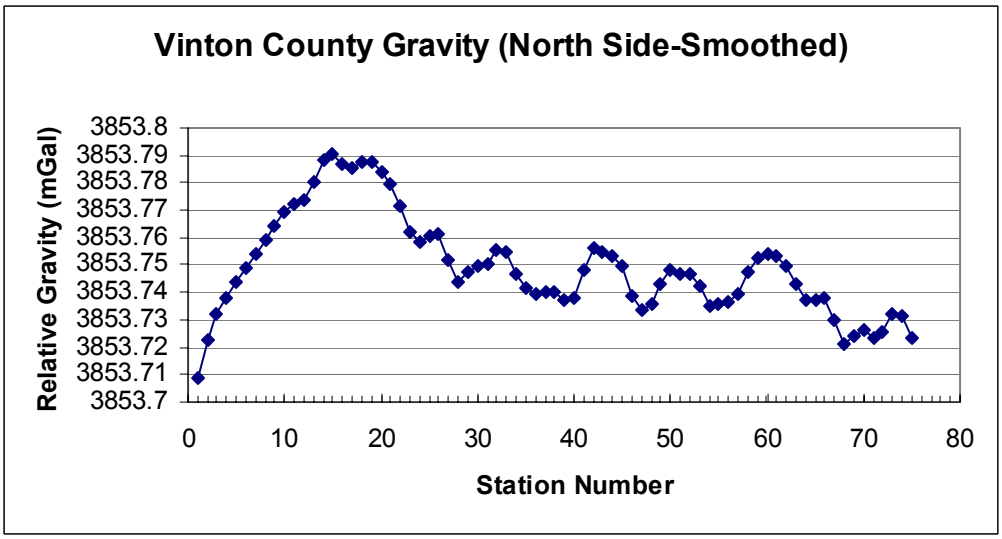

Figure 38. Smoothed gravity profile along the north berm.

western end of the line which quickly decreases. These data seem to be abnormal from what we expected to see, which may be the result of a deeper regional trend. No evidence of mining is apparent at this location.

SASW composite experimental dispersion curves with theoretical fits are shown in Figure 39, and the resulting shear wave velocity profiles are shown in Figure 40. Shear

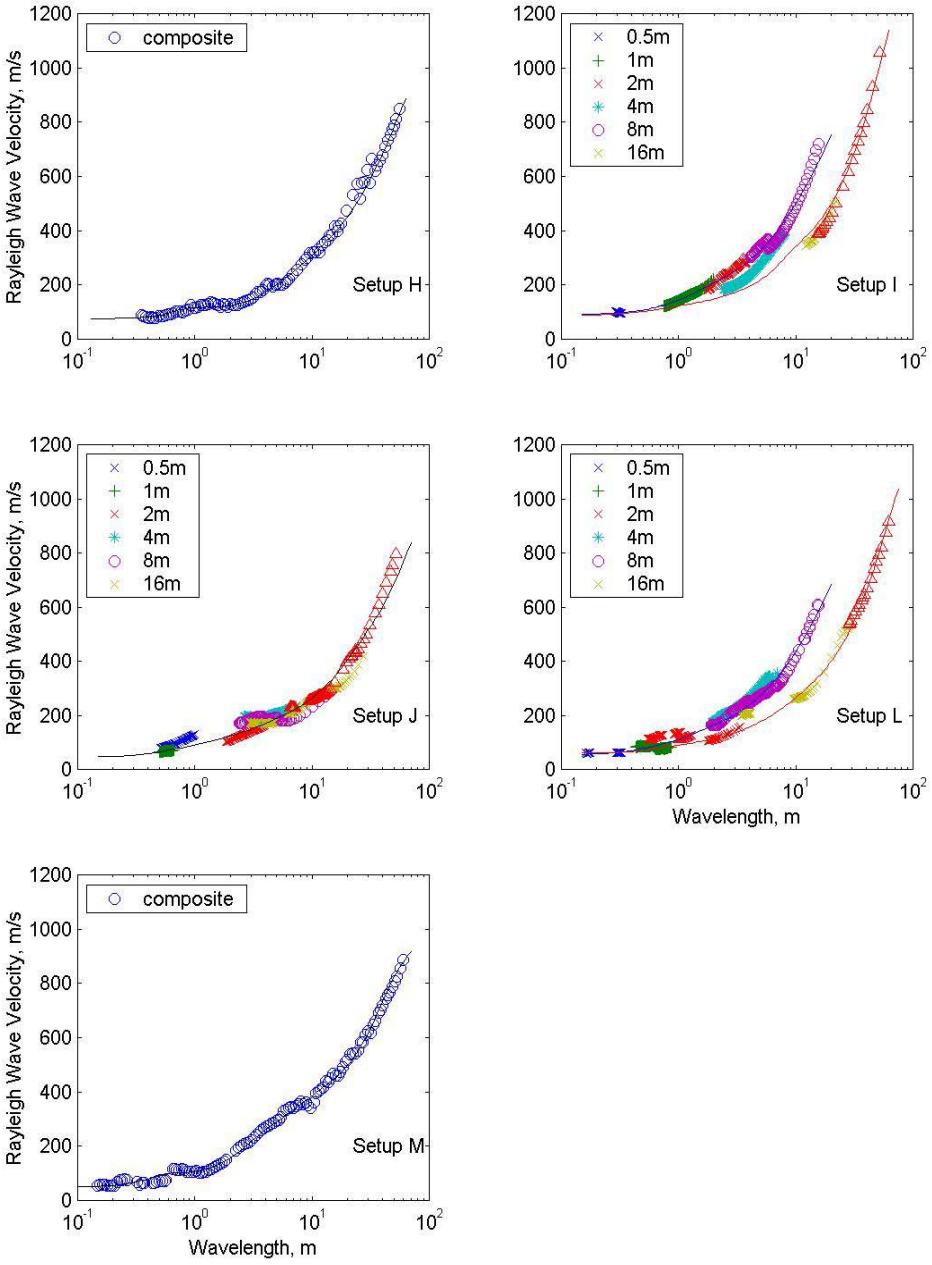

Figure 39. Experimental dispersion curves, with theoretical fits (solid line) for Vinton County site. Different symbols represent SASW measurements at different receiver spacings.

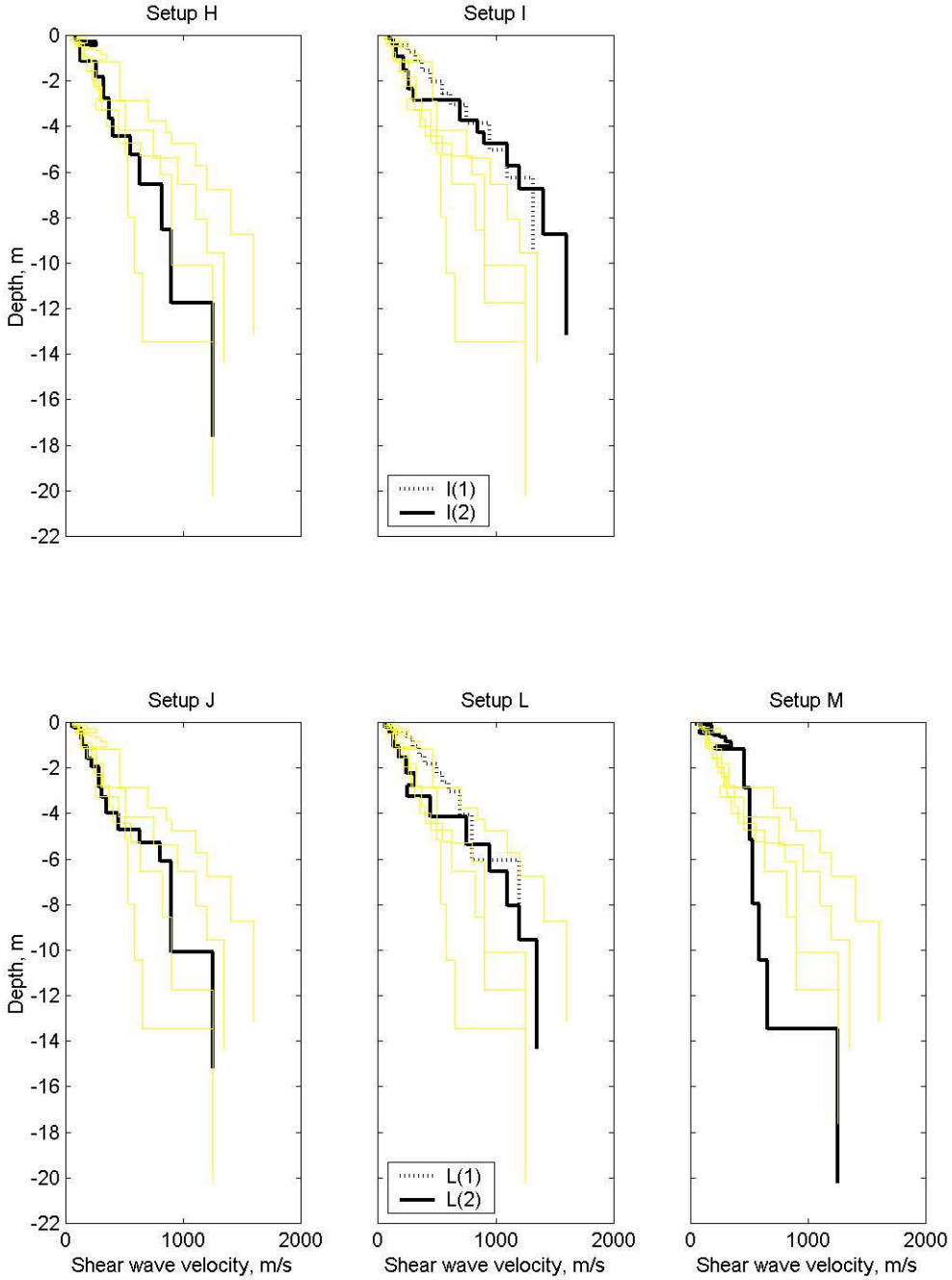

Figure 40. Shear wave velocity profiles for Vinton County site. All profiles are shown, with indicated setup highlighted.

wave velocities determined from SASW measurements ranged from 50 m/s, which is appropriate for soft soil, to an imposed maximum of 2200 m/s. The upper-bound shear wave velocity was selected by considering the maximum P-wave velocity measured at the site (2,950 m/s) and a minimum Poisson's ratio that can be considered reasonable for rock (0.1; Goodman, 1980, Table 6.1). Shear wave velocities at depth are low for Setup M, and high for Setups I and L. Recall that Setup M was collocated with a known cavity. The shear wave velocity profile for this location has a distinctly different shape from others generated at the site.

Two sets of constant offset measurements were collected. Setup K was situated along a 210 m (700 ft) array on the north shoulder with 6.0 m offset and 8.0 m receiver spacing, starting at Sta. 4 and ending at Sta. 74. Source energy was applied using both the sledgehammer and the EWG. Setup N was situated along the centerline of the median with 4.5 m (15 ft) offset and 9 m (30 ft) receiver spacing, starting at Sta. 17 and ending at Sta. 63.5. Source energy was supplied with the EWG. The testing geometry, which was slightly different from that used on the other arrays, was selected for convenience, to take advantage of the flags from the other geophysical surveys.

The unwrapped phase data from the two constant offset measurement arrays are shown in Figures. 41 and 42. The interpreted anomalies are listed in Table 2, and illustrated in Figure 43. For comparison, anomalies indicated in SASW measurements (discussed earlier) in the same vicinity are also provided in Table 2.

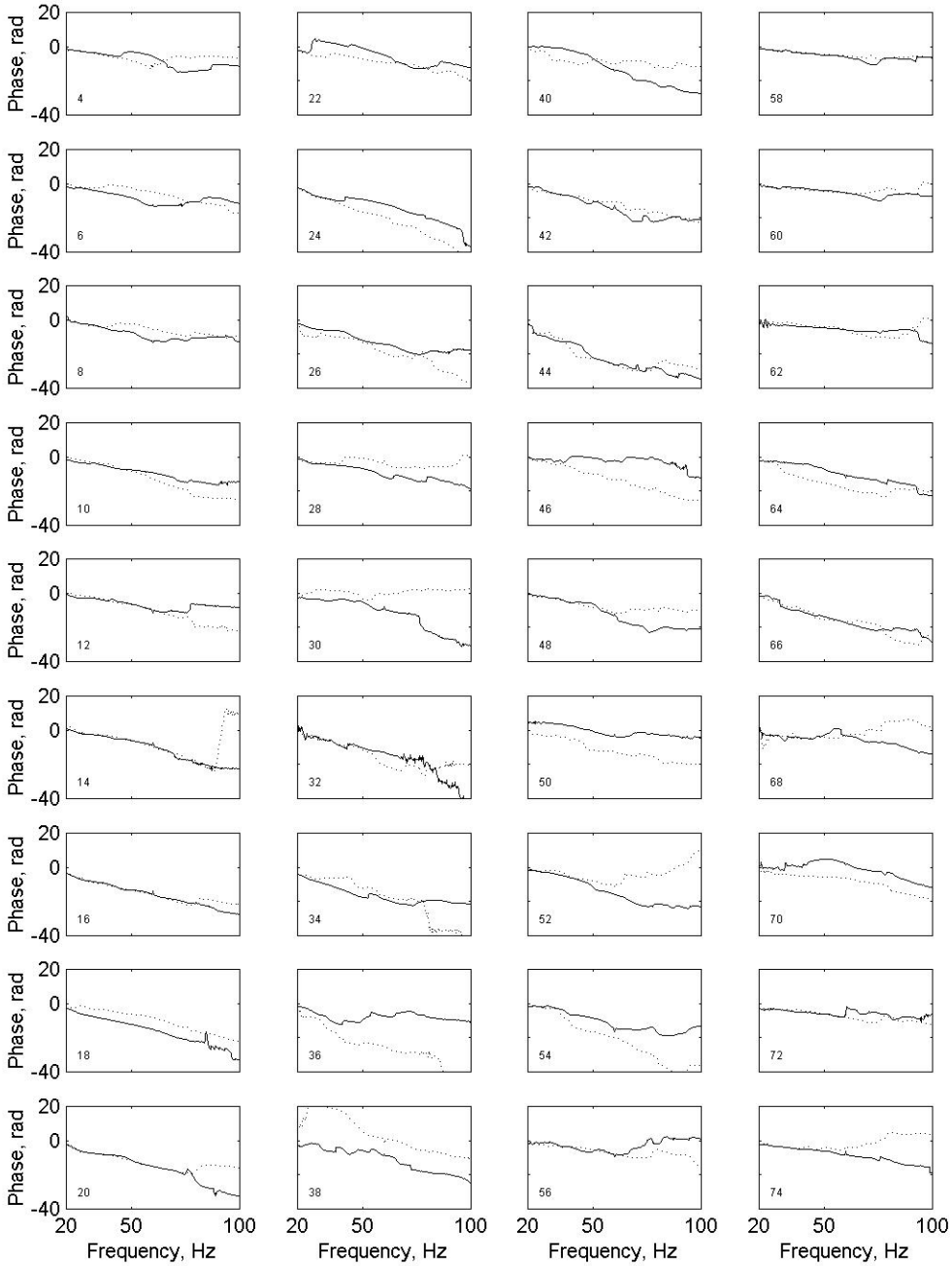

Figure 41. Forward (solid) and reverse (dashed) constant-offset measurements on the shoulder at Vinton County Site (Setup K).

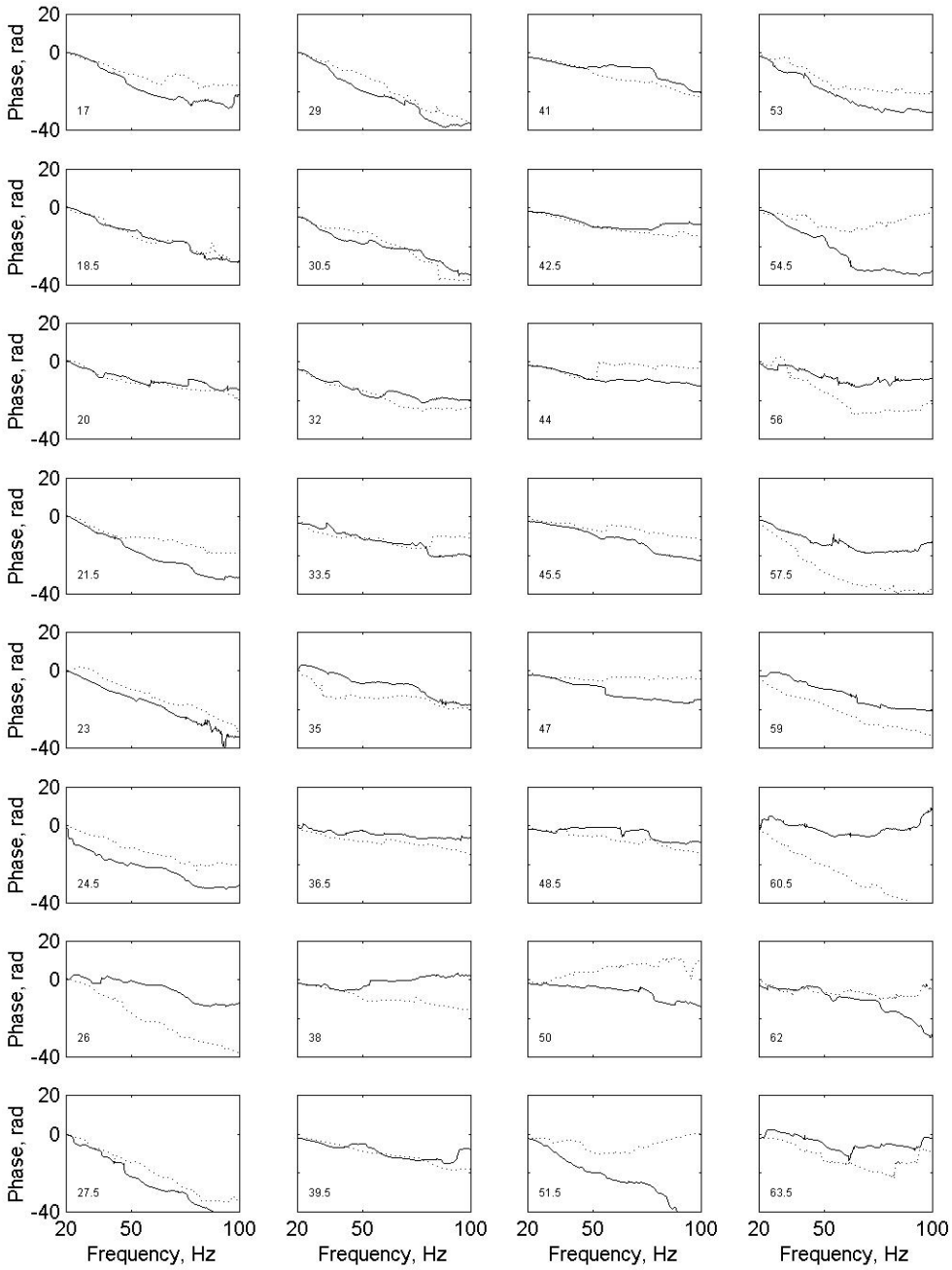

Figure 42. Forward (solid) and reverse (dashed) constant-offset measurements on the median at Vinton County Site (Setup N). Station numbers are indicated.

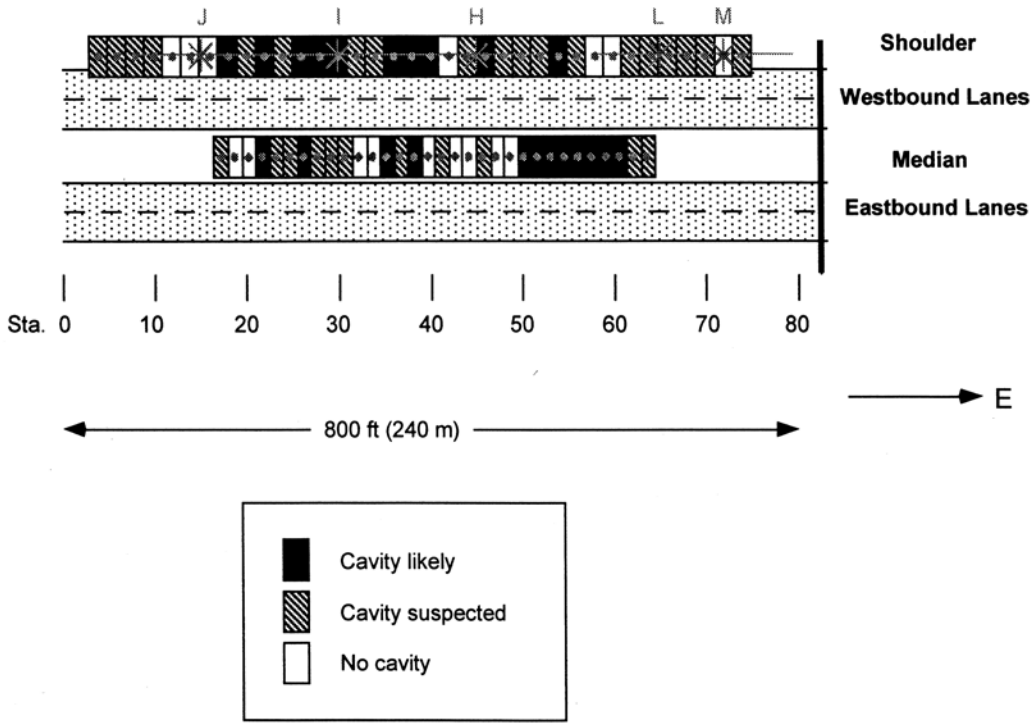

Figure 43. Suspected anomalies indicated by constant-offset measurements for Vinton County site.

The pattern of suspected anomalies showed a distribution of cavities that might be expected for a room-and-pillar mine. The shear wave velocity profile located over the known cavity (Setup M, Sta. 72) did indicate reduced stiffness with respect to other locations along the test section. Profiling data did not indicate a cavity at that station, but adjoining measurements were interpreted to have suspected cavities.

Aside from anomalies seen in the resistivity surface wave data there is no geophysical evidence to suggest the possibility of future collapse. We recommend drilling be performed at this site, specifically, if there is a concern over the apparent mining feature.

Table 2. Seismic anomalies determined by surface wave measurements. Rankings are 0 for none, 1 for slight, and 2 for significant. . [Profiling was advanced in two station increments. The three SASW surveys were centered at the stations with table entries.]

Vinton County Site									
Shoulder						**Median**			
Station No.	**Anomaly** *Ranking*		**Stn. No.**	**Anomaly Ranking**		**Stn. No.**	**Anomaly Ranking**	**Stn. No.**	**Anomaly Ranking**
	Profiling Setup K	SASW		Profiling *Setup N*	SASW		Profiling Setup N		Profiling Setup N
4	*1*		40	*2*		17	*1*	44	*0*
6	*1*		42	*0*		18.5	*0*	45.5	*1*
8	*1*		44	*1*	*1*	20	*0*	47	*0*
10	*1*		46	*2*		21.5	*2*	48.5	*0*
12	*0*		48	*1*		23	*1*	50	*2*
14	*0*	*1*	50	*1*		24.5	*1*	51.5	*2*
16	*0*		52	*1*		26	*2*	53	*2*
18	*2*		54	*2*		27.5	*1*	54.5	*2*
20	*1*		56	*1*		29	*1*	56	*2*
22	*2*		58	*0*		30.5	*1*	57.5	*2*
24	*1*		60	*0*		32	*0*	59	*2*
26	*2*		62	*1*		33.5	*0*	60.5	*2*
28	*2*		64	*1*	*2*	35	*2*	62	*1*
30	*2*	*2*	66	*1*		36.5	*1*	63.5	*1*
32	*1*		68	*1*		38	*2*		
34	*1*		70	*1*		39.5	*0*		
36	*2*		72	*0*	*2*	41	*1*		
38	*2*		74	*1*		42.5	*0*		

C. Perry County Site – Phase II

a. Introduction

The survey lines in Jackson and Vinton Counties were relatively short. A much longer site was selected in Perry County, Ohio, for the Phase II studies. The site was recommended by ODOT because subsurface mines were known in the area and old mine maps were available. The stretch of highway was relatively straight and had wide areas on the east side for safely conducting the field data acquisition. The results of Phase I were used to choose seismic refraction and resistivity as the most effective techniques. We recommended to ODOT that surface wave profiling be added to the other techniques being employed at the site but this was not included due to budgetary constraints. The experience gained in Phase I was used to design the data acquisition plan for this phase.

b. Site Location and Mining History

The site, located in Monroe Township, Perry County, Ohio, is approximately 19 miles north of Athens (Figure 1). Surveys were conducted along the east side of State Route 13. The entire length of the line is approximately 4.5 kilometers. The village of Corning lies approximately in the middle of the line.

The first reported production of coal in Ohio was in 1800. This was 3 years prior to its entrance as the 17th state of the union. The first known production in Perry Co., Ohio was in 1816 and as of 1993 over 395,321 tons of coal have been removed from Perry Co. From 1800 to1993 the cumulative production of coal in Ohio was 218,954,437 tons, making Ohio 4th in production (Crowell, 1995). Coal was mined entirely by hand until 1876, when the first coal-cutting machine was put into operation. The primary method of underground mining was room and pillar. In this process, coal is mined in rooms separated at regular intervals by roof-supporting pillars. Towards the completion of mining operation, the pillars were often further removed, increasing the potential for collapse.

c. Geology of the Site

Perry County lies within glaciated and unglaciated portions of the Appalachian Plateau. Glaciation is restricted to the northwestern region of the county leaving the eastern and southern regions primarily unglaciated. However, isolated patches of glacial outwash or colluvium may be found in the southeastern portions of the county where the test site is located.

Bedrock dips to the east-southeast, exposing Mississippian rock in the western parts of the county and Pennsylvanian rocks elsewhere. Since the study site lies within the southeastern region of the county only descriptions of Pennsylvanian rocks will be given. There are potentially two major Pennsylvanian formations found at this site, the Conemaugh and the Allegheny. Figure 44 is a generalized stratigraphic section of the Conemaugh (lower) and Allegheny Formations. The Conemaugh has little economic importance as the coal found within this formation is commonly bony or shaly and less than one meter thick. The Allegheny formation is without question the most economically important formation in this region. The major coal beds found within the Allegheny formation are the Lower Kittanning (no.5), Middle Kittanning (no.6) and Upper Freeport (no.7). Of these three, the Middle Kittanning (no.6) is the most important one. The Middle Kittanning underlies the eastern and southeastern regions of Perry County and is not known to be less than 1 meter thick except in areas of the Jumbo Fault (Brant and DeLong 1960). Not a fault at all, the Jumbo Fault is a miner's term for areas where the Middle Kittanning coal is absent and replaced by sandstone, shale or limestone. Figure 45 is an isopach map of the Middle Kittanning also showing the extent of the Jumbo Fault. USGS and drilling logs from local oil and gas companies suggest that the Middle Kittanning (no.6), which was mined here, is approximately 12 to 18 meters below the surface along State Route 13 near the Village of Corning.

Figure 44. Generalized stratigraphic section of the Conemaugh (lower) and Allegheny Formations. (Modified from Brant and DeLong, 1960)

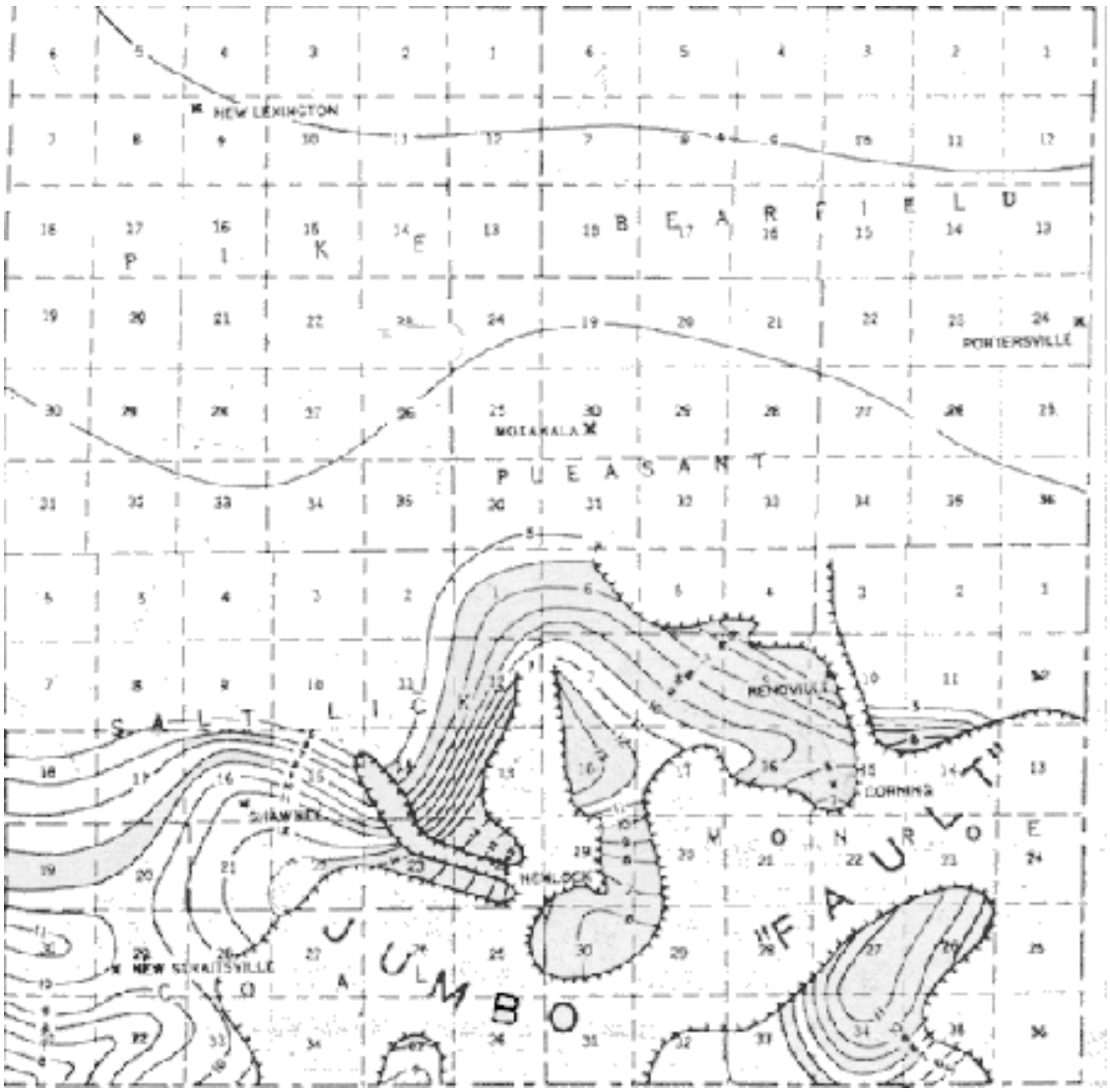

Figure 45. Isopach map showing the thickness of the Middle Kittaning Coal and the Jumbo Fault where this coal is absent (after Brant and DeLong, 1960).

d. Methods and Acquisistion

Seismic Refraction

Field Procedures

The survey consisted of one line parallel to State Route 13, approximately 2 to 4 meters east of the roadway. P-wave data were collected along the entire length of the 4.5 km line but due to time constraints only 2.5 km of S-wave data were collected.

We used the standard in-line spread in which the energy source or shot point was placed along the same line as the geophones. Figure 46 shows the geophone and shotpoint geometry. Five shots were taken for every spread: One shot (A) 2 meters before the first flag, 3 interior shots (B, C, D) and a final shot (E) 2 meters beyond the last flag. The total length of each spread was 96 meters and to assure good data we overlapped each spread by one cable length or 24 meters.

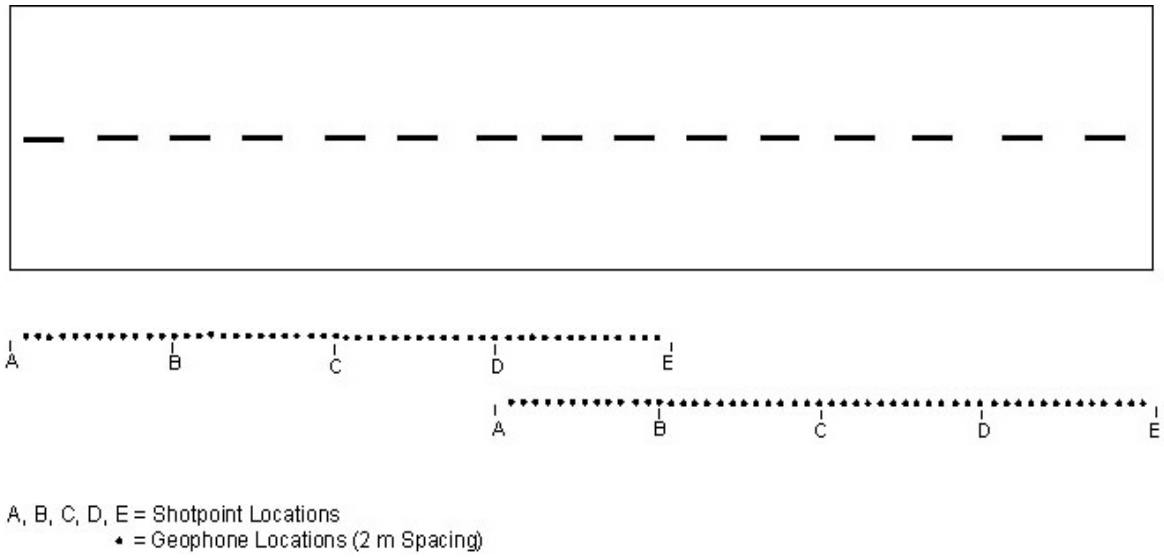

Figure 46. Geophone and shotpoint pattern for Perry County survey. One move-up is shown.

The survey was conducted using a 48-channel Strataview engineering seismograph with 30-hertz geophones at 2m-station spacing. Both P- and S-wave seismic refraction data were collected. The P-wave data were gathered using a Bison elastic wave generator (EWG) as the energy source. The S-wave data were gathered using a metal rectangular

box, which was then struck on each side 10 to 20 times using a 5.5-kg (12-lb) sledgehammer. Reversing the recording polarity and then striking the box on the opposite side can effectively cancel out the P-waves in the summed records, leaving only the S-waves.

Data Processing using SIP

The SIP software was again used to develop travel-time curves, depth models and obtain velocities for both the P- and S-wave surveys. We created 2-layer models and thus two lines with differing slopes were used in our graphs. Figure 47 is an example travel-time curve derived from one shot in the P-wave data set. Travel-time curves for both P- and S-waves are included in Appendices F and G. From a set of travel-time curves one may determine rock layer velocities and depth to interface (bedrock). For later interpretation we will be focusing on depth to bedrock or more specifically lateral changes in depth to bedrock that may be useful for detecting the presence of a void or collapse. In the event of a void collapse, overlying unconsolidated material will fill in the void space. In the depth model created from the travel-time curves an anomalously low bedrock elevation may indicate the presence of this collapse. This anomaly could be the result of collapse but may also be due to slower velocities resulting from fracturing.

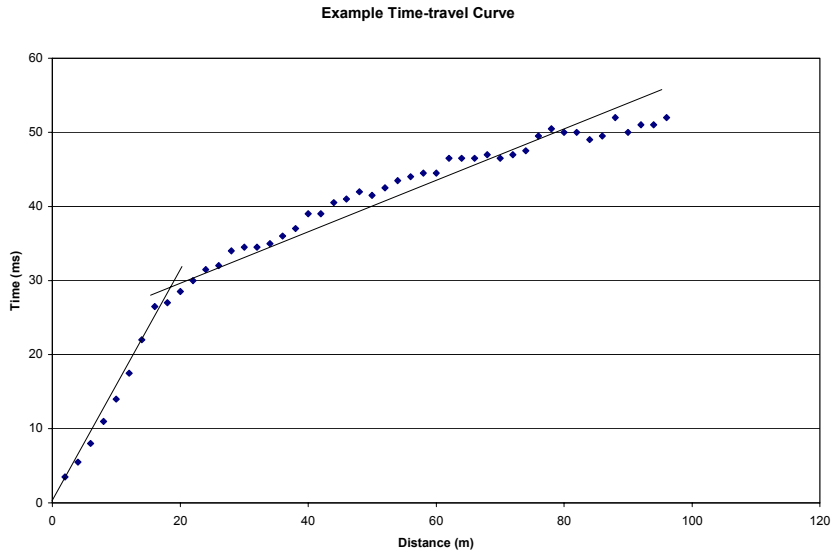

Figure 47. Typical time-travel curve for sesmic refraction.

Results

Using the SIP program we chose the first breaks for each shot, created travel-time curves assigning a layer number to each first arrival and finally created cross-sectional depth models. Each depth model consists of 5 spreads with 20 shots and is approximately 400 m in length. Because the maximum vertical depth for the models is only 20-30 meters and the horizontal length is 400 m, vertical exaggeration is necessary for plotting the results. This must be taken into consideration during the interpretation process because vertical exaggeration will enhance the appearance of lateral changes in bedrock depth. Cross-sectional depth models for both P- and S-waves are found in Appendices H and I.

P-waves

Analysis of the seismic P-wave refraction data resulted in a 2-layer depth model for the entire length of the survey. No refraction wave arrivals from deeper layers were observed so a thickness of layer 2 cannot be calculated. The layer-2, P-wave velocities range from 2100 to 3000 m/s. Layer 1 ranges in thickness from 1 to 16 meters and has a P-wave velocity ranging from 596 m/s to 1100 m/s. This layer is believed to be the combination of colluvium and unconsolidated road fill used in the construction of State Route 13. Layer 2 is believed to be bedrock of the Allegheny Formation, which could be sandstone, limestone or shale along various sections of the survey.

Due to the undulating nature of the bedrock surface in the models, it is difficult to discern bedrock anomalies caused by mining from those found over areas that are considered unmined. Based on P-wave models, however, four exploratory drilling sites were chosen as potential collapse zones or uncharted mining zones. These sites are given in Table 3.

There were two sites (sites 1 and 3) that were chosen based on apparent irregular bedrock topography shown in the cross-sectional depth models [Appendix H, Figures H3 (a) and H5 (a)]. Whether this irregularity is caused by bedrock undulation, fracturing or heterogeneous fill is unknown. According to the maps, site 3 corresponds to an

underlying mined zone. Site 1 displayed similar characteristics but the maps indicated no previous mining operations. At site 1 State Route 13 was built over an existing pond. The pond was either removed or filled in during construction of State Route 13. Variant velocities found within this zone may have been produced by heterogeneous fill, although seepage from the pond along fractures (natural or mine induced) and associated weathering in the underlying bedrock could produce the same effect.

Sites 2 and 4 were chosen because they displayed large spikes or increases in apparent bedrock depth, which correlated to nearby mines. Site 2, just north of the village of Corning, overlies at least two designated mining structures. One is a room or pathway connected to the Nelson Rodgers mine and the other is labeled as a *haulage entry* approximately 90 meters to the north. Mine number 11 and another haulage entry are also shown to be 100+ meters to the south of this site. No obvious P-wave anomalies are associated with either but an elongated low resistivity anomaly is found along the entire length of this site, which will be discussed in detail later. It is therefore plausible that other uncharted rooms or tunnels may connect these individual mining structures. Site 4 is also characterized by a bedrock low which overlies a mining zone apparently consisting of several rooms and pillars. This anomaly is smooth and less obvious but the correlation to the underlying mining zone can not be ignored.

Table 3: Recommended Exploratory Drilling Sites Based on P-wave Models

Site	ODOT Station Intervals (ft)	WSU Survey Location (m)	Approximate Depth (m)
1	208+36 – 213+28	1450-1600	15
2	242+81 – 246+09	2500-2600	10
3	259+21 – 265+77	3000-3200	8
4	271+68 – 274+63	3380-3470	10

S-waves

Analysis of the S-wave refraction data also resulted in a 2-layer model. In fact, the models almost mirrored those from the P-wave data set. Layer 1 ranges in thickness from 0 to 19 meters with S-wave velocities ranging from 272-445 m/s. Again this layer is believed to represent unconsolidated road fill and/or colluvium. With no observed third layer, a thickness for layer 2 could not be determined. The S-wave velocity of layer 2 ranges from 718-1335 m/s representing rock units from the Allegheny Formation.

The undulating peaks and valleys from the S-wave models seem to be more exaggerated than those of the P-wave models. This may be due to incompletely canceled P-waves, which often masked the S-wave arrivals making it difficult to accurately determine their time. This adds uncertainty to our models. For this reason the S-wave models were not used to determine site locations but rather as reinforcement to the results seen in the P-wave models. At each of the sites chosen from the P-wave data sets, S-wave models displayed similar characteristics but to an exaggerated extent.

Electrical Resistivity

The survey was conducted using a Sting/Swift R1 resistivity meter utilizing 28 electrodes driven into the ground at a 6-meter spacing. In dry conditions it was sometimes necessary to wet the ground around the spikes to assure a good current flow. The instrument was set to the dipole-dipole configuration. During the data acquisition several areas along the line were avoided due to the concern that conductive objects such as fences and guardrails would produce unreliable results. The areas of data acquisition versus areas avoided have been highlighted in Figure 48.

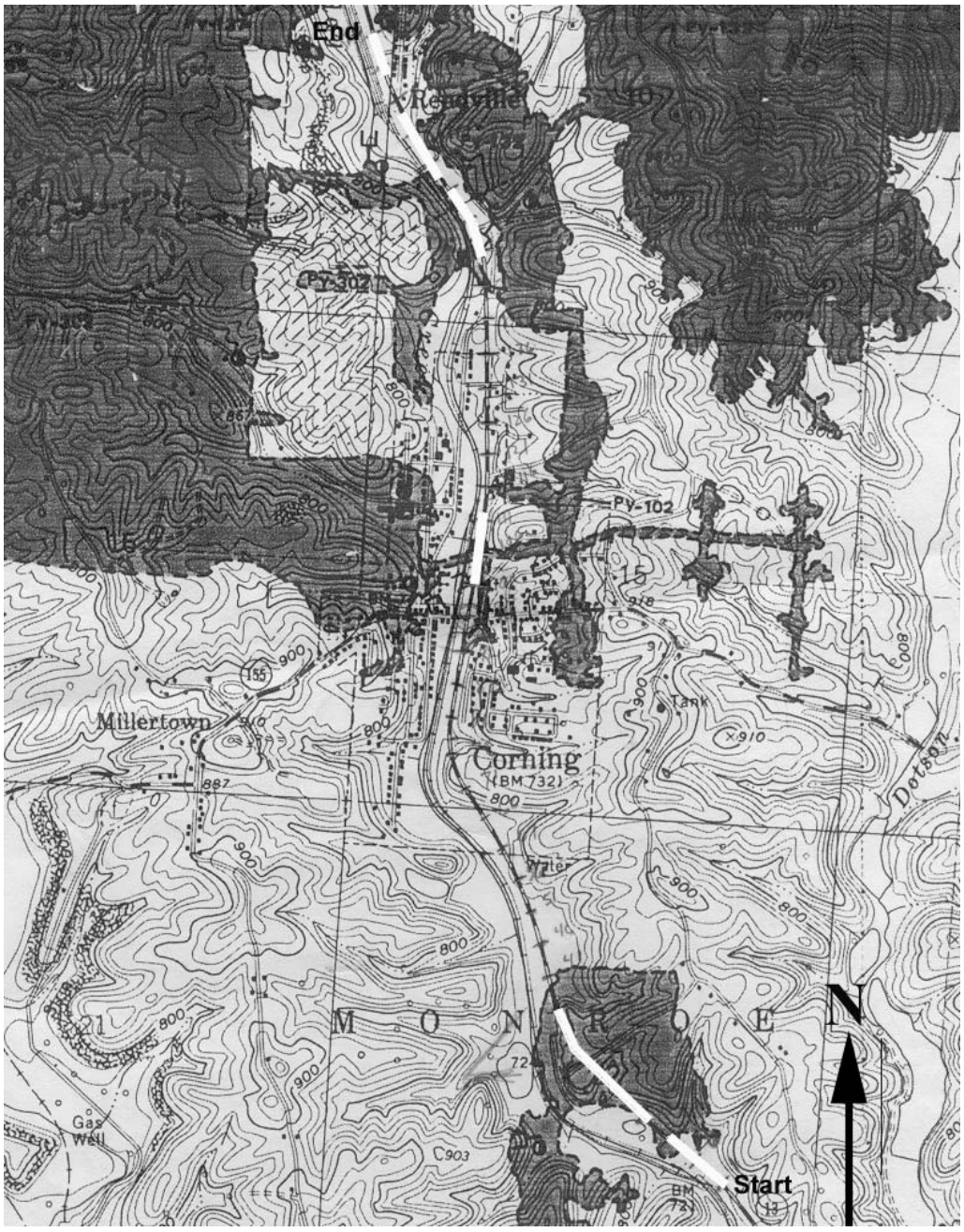

Figure 48. Site Map. White line indicates where resistivity data were collected. (Background abandoned mine map after DeLong, 1983)

As in Phase I the resisitivity data were interpreted using Res2Dinv 2-D inversion software. The inversion program uses datum points and rectangular blocks from what is known as the pseudosection to create the model via a least-squares optimization technique. The overall output from the program consists of three models seen in Figure 49: a measured apparent resistivity pseudosection, a calculated resistivity pseudosection

and an inverse model resistivity section. Each model uses a graded color scale to show various ranges of resistivity values. The final model or the inverse model resistivity section may differ depending on several user-defined parameters. The goal is to minimize the RMS error between the values of the modeled and measured pseudosections within the constraints of having a geologically reasonable model. It was necessary to establish maximum error above which data may be deemed unreliable. We set a goal of 10% but often could find no major changes in the models as the error percent dropped during the iteration process. In some cases it was impossible to get the error below even 30% despite editing bad data points.

Figure 49. Example of 2D resistivity imaging results.

The inversion process resulted in seven models, spanning the length of the survey. It is unfortunate, however, that several gaps exist within the data set due to nearby conductive objects such as guardrails or fences, which prevented the acquisition of reliable data. 2D resistivity models can be found in Appendix J.

Based on the mine maps supplied by ODOT, we were able to correlate areas of known mining operations to areas of low resistivity anomalies. The apparent resistivity values of the anomalies range from less than 0.43 Ω*m to 50 Ω*m. There were also zones of low resistivity that did not correspond to areas of known mining operations. This may be due to poor mine maps or to high quantities of clay found within the road fill or colluvium. Clay is a highly porous but poorly permeable material and thus can store a large volume of water. It has free ions on the mineral grain surfaces, which causes clay to act as a good electrical conductor.

Zones of higher resistivity ranging in value from 50 Ω*m to 400 Ω*m are believed to be those of bedrock and intact coal. Coal in its virgin state commonly has a resistivity of 100 Ω*m to 500 Ω*m depending on saturation, pore water resistivity, porosity and permeability. Sandstone and limestone can also be expected to have apparent resistivity values of 50 Ω*m up to 10^8 Ω*m.

Three drilling sites were selected based on the resistivity models. These are shown in Table 4. The first site, also labeled Site 2, is an elongated low resistivity zone from 6 to 8 meters deep and at least 216 m in length from survey location 2472 to 2688 m [Appendix J, Fig.J1 (c)]. This is the site that corresponds to Site 2 of the P-wave models mentioned in the refraction results. Low resistivity values, ranging from .43 Ω*m to 12 Ω*m, are located within and extending beyond the regions of the Nelson Rodgers mine and the haulage entry. According to engineering maps, there is a 4-inch to 6-inch cast iron pipe located 2 m under the centerline of the roadway along this segment, which likely causes a large decrease in overall resistivity there. Several local anomalies, however, overlay the effects of the pipe. For this reason and because of the correlation with P-wave models,

this a good drilling location. The second site (Site 5) can be broken down into two halves. The first half approximately 50 m in length and 9 m deep from survey location 3690 to 3738 m consist of three local anomalies ranging from 23 to 60 Ω*m. These extend north to the larger, deeper half of the site located from 3738 to 3840 m. Here the anomaly is approximately 100 m in length and again ranges from 23 to 60 Ω*m, averaging 30 Ω*m [Appendix J, Fig.J1 (d)]. Nothing from the mine maps or the refraction models corresponds with these anomalies or suggests a cause, and so exploratory drilling is recommended. A third site (Site 6) [Appendix J, Fig.J1 (a) and (b)] was also identified for ODOT to conduct exploratory borings. At this site, a significantly low resistivity zone, in the deeper part of the section, is present from survey location 192 to 684 m. It is uncertain whether this anomaly is continuous due to an extensive gap in the data set from survey location 264 to 366 m. However, a large discontinuous mined zone, as indicated by the mine maps, is present from survey location 150 to 840 m. But the most interesting feature of this model is the abrupt change in resistivity at survey location 198 m. This may represent the actual boundary between intact coal and mined coal.

Table 4: Recommended Exploratory Drilling Sites Based on Resistivity Models

Site	ODOT Station Intervals (ft)	Survey Location (m)	Approximate Depth (m)
2	241+88 – 248+97	2472 - 2688	10
5	281+85 – 286+77	3690 - 3840	8 –14
6	165+70.5 – 188+34.3	150 - 840	16+

e. Data Comparison

The P- and S-wave depth models and the resistivity models yielded a moderate to good correlation to mined versus unmined areas indicated by mine maps given to us by ODOT. In the P- and S-wave depth models, apparent erratic bedrock topography or sharp increases in bedrock depth, sometimes correlated well with known mining zones. P-

wave depth models proved to be more reasonable than those resulting from S-waves, which may be attributed to incompletely cancelled P-waves in the S-wave data sets. This made it difficult to pick first breaks and resulted in poorer models.

Some areas of low resistivity were shown to correlate well with known mining zones. However, in only one case did an anomaly from resistivity models correlate with an anomaly from refraction depth models. This site was complicated by a water line, located 2 meters below the centerline of the roadway, which may be decreasing the overall resistivity of the site. Part of the lack of correlation between the two methods can be attributed to resistivity data not being collected along the entirety of the line. Conductive grounded obstacles, such as guardrails or fences, caused these breaks in continuity because they would have likely contributed to unreliable data.
It should also be mentioned that neither method was capable of delineating all the mined zones shown on the maps. In fact, both the refraction models and resistivity models showed anomalous characteristics where no mine workings were indicated by the maps. Without the benefits of the drilling data, it is difficult to determine whether these anomalies are due to unmapped mines or other geologic features.

The main purpose of Phase II of the project was to use results of Phase I to develop better field techniques for locating voids under roadways or distinguishing competent rock from problem areas. We believe that seismic refraction and 2D-resistivity imaging techniques can be successful for these applications. In our opinion, no collapse hazards were identified at the Perry County site. We must emphasise, however, that without the ground truth obtained from drilling, it is difficult to assess the accuracy of our interpretation.

IV. Conclusions and Recommendations

This research project started in 1998 as a joint effort between Wright State University and the Ohio Department of Transportation. The objective was to develop a reconnaissance geophysical method for locating zones in coal mining regions, where a highway has the potential for collapse. The project consisted of two phases. During Phase I, several geophysical methods were tested at two sites along Ohio Route 32, one in Jackson County and the other in Vinton County. The goal was to determine the method or combination of methods best able to locate problem zones. We concluded that seismic refraction and 2D-resistivity imaging were the most promising techniques. Subsequently, during Phase II, seismic refraction and 2D-resistivity imaging were once again implemented. A 4.5-km section along State Route 13 in Perry County, Ohio was chosen as the test site. The goal of this phase was to determine if zones of potential problems could be identified.

Geologically the sites differed in lithologic composition and in bedrock depth. This is believed to be a significant factor contributing to the differing results among the studies. The Jackson County site, having bedrock as shallow as 0.5 meter, displayed the best results. This was especially true of the two most successful geophysical methods, seismic refraction and 2D-resistivity imaging. Both seismic refraction and 2D-resistivity were able to locate voids within the coal bed 2 to 4 meters below the surface. This was confirmed by drilling and subsequent excavation of the site. The Vinton County data acquired at the same time showed little evidence of collapse or problem areas. The depth to bedrock of this site was greater and more variable due to undulating topography, which required the use of road fill to accommodate a relativity horizontal roadway. Because of the evidence of active failure at the Jackson County site, less emphasis was given to the Vinton County site. Out of 5 previous drilling locations at the Vinton County site, near mapped subsurface mines, only one encountered a significant void. This combined with the lack of geophysical evidence to suggest a potential problem, has led us to believe that the probability of collapse in the near future is low. The Perry

County site also had highly variable bedrock depth. The upper unconsolidated layer ranged in thickness from 1 to 16 meters. This information was attained from the P-wave seismic refraction models, which we estimated to be accurate within $\pm$ 10%. As part of the project requirements, 6 drilling locations were identified for ODOT. Two of these sites had geophysical evidence that suggested there is potential rock breakdown or fracturing. One of these was located in the region of a mined area. Other sites were chosen because anomalies were seen at the locations of mined areas suggesting we may have been able to identify some of the mines where collapse has not taken place. Because of the environmental concerns related to releasing artesian water from abandoned mines, ODOT decided not to drill. Consequently, our interpretations were untested.

Both seismic refraction and 2D-resistivity imaging have certain limitations. One limitation common to both methods is the target depth. Both resolution and reliability of data decrease with depth. Another limitation of seismic refraction occurs when there is a high velocity layer located above the target. In this situation, pertinent information related to the target may be missed. Resistivity is limited by the presence of nearby conductive objects, which may result in unreliable data.

The results of any geophysical method are non-unique, that is, an anomaly observed by the method may be the result of the proposed target, but could also be produced by other unrelated geologic conditions. Geophysical techniques are used to locate zones of contrasting physical properties such as density or resistivity. These techniques have proven to be useful, however they must be used in conjunction with ground truthing methods such as drilling. The results of a geophysical survey can be used to rule out areas where problems do not exist, so that the focus may be on areas where problems do exist.

In light of the above discussion, concerning the present research studies, we have determined that geophysics can be successfully employed to locate problem areas within the subsurface. At the Jackson County site, where geologic conditions were conducive,

we were able to identify voids at depths of 2 to 4 meters below the surface using seismic refraction and 2D-resistivity imaging. For other more geologically complicated sites, such as the Vinton County and Perry County sites, further studies are needed to develop general field procedures for broad reconnaissance. The ideal site should contain evidence of collapse and there should also be detailed geologic records. It is also necessary that there are no environmental conditions that may prohibit drilling.

Consideration of the usefulness of the seismic refraction attenuation study and the limitations of the seismic refraction method, as it was applied in this study, suggests the need for a modified approach. The modified approach should take advantage of the sensitivity of upcoming seismic waves to mines and disturbed areas and be less dependent on variations in the near-surface rock layering. This concept, which is worth future research effort, is to try using seismic waves coming from greater depth (reflected or refracted waves) to analyze differences in arrival strengths (attenuation) and delay times due to shallow anomalous zones such as voids or collapsed mines. The proposed modified approach would require a longer horizontal source-receiver distance than was utilized in the research we reported here. The longer horizontal source-receiver distance would allow upcoming waves to originate deeper than the target horizon.

References

Brant, R.A., and Delong, R.M., 1960, Coal Resources of Ohio, Bulletin 58: Ohio Division of Geological Survey.

Burger, R.H., 1992, Exploration Geophysics of the Shallow Subsurface, Prentice Hall P T R, New Jersey.

Crowell, D. L., 1991, Drilling for Mine Subsidence Mitigation in 1990, Report on Ohio Minerals Industries: Ohio Division of Geological Survey, Annual Report, p. 5-11.

Crowell, D.L., 1995, History of the Coal-Mining Industry in Ohio, Bulletin 72: Ohio Division of Geological Survey.

DeLong, R. M., 1983, Abandoned Underground Mine Map Series (Corning, Ohio, Quad), Ohio Division of Geological Survey.

Goodman, R. E., 1980, Introduction to Rock Mechanics. John Wiley and Sons, p. 177.

Gucunski, N., V. Ganji, and M. H. Maher, 1996, Effects of obstacles on Rayleigh wave dispersion obtained from the SASW test, *Journal of the Soil Dynamics and Earthquake Engineering* Vol.15, No.4, pp. 223-231.

Loke, M.H., 1999, Geoelectrical Imaging 2D and 3D, Guide to RES2DINV ver.3.4 for Windows 3.1, 95 and NT.

Luke, B. A., and J. E. Brady, 1998, Application of seismic surface waves at a Pre-Columbian settlement in Honduras, *Archaeological Prospection*, Vol. 5, No. 3, pp. 139-157.

Luke, B. A., and D. S. Chase, 1997, Detecting caves using seismic surface waves: A feasibility study, *Proceedings of the Sixth Multidisciplinary Conference on Sinkholes and the Engineering and Environmental Impacts of Karst, Springfield, Missouri,* 6-9 April, 1997, pp. 419-424.

Munk, J, and R. A. Sheets, 1997, *Detection of Underground Voids in Ohio by Use of Geophysical Methods,* U.S. Geological Survey Water-Resources Investigations Report 97-4221, Columbus, Ohio, 1997.

Reynolds, J.M., 1997, *An Introduction to Applied and Environmental Geophysics*: John

Wiley and Sons, England.

Stokoe, K. H., II, S. G. Wright, J. A. Bay, and J. M. Roesset, 1994, Characterization of Geotechnical Sites by the SASW Method. In *Geophysical Characterization of Sites*, ed. R. D. Woods, Oxford and IBH, New Delhi, pp. 15-25.

Stout, Wilber, 1927, Geological Survey of Ohio, Fourth Series: Bulletin 31, p. 158-348.

Vrettos, C., and B. Prange, 1990, Evaluation of in situ effective shear modulus from dispersion measurements, *Journal of Geotechnical Engineering*, Vol. 116, No. 10, p. 1581-1586, with subsequent discussions by G. Gazetas (Vol. 118, No. 7, p. 1120-1122) and G. J. Rix (Vol. 118, No. 7, p. 1122-1125).

Appendix A: P Wave Travel Time Data, North and South Sides

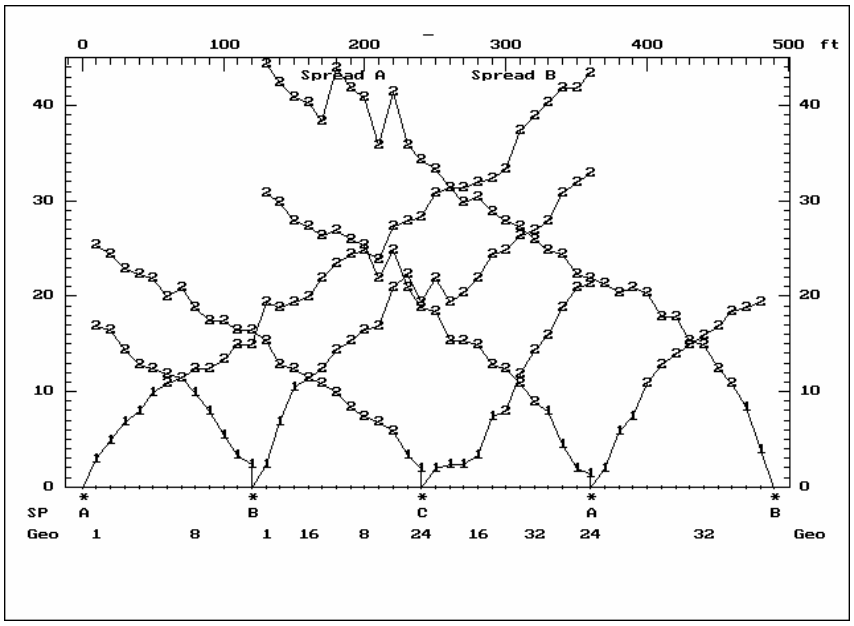

Figure A.1: P Wave Travel Time Curve, North Side.

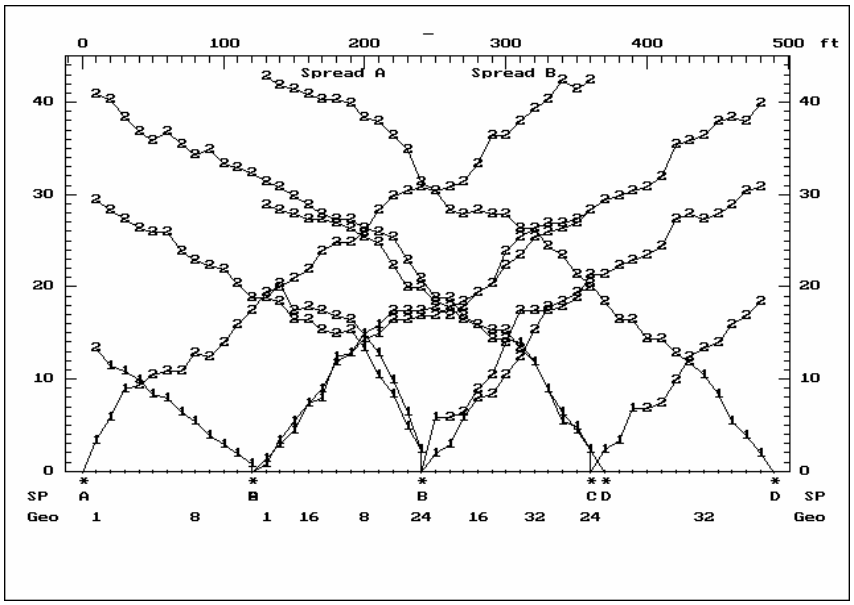

Figure A.2: P Wave Travel Time Curve, South Side.

Appendix B: P Wave Refraction Model

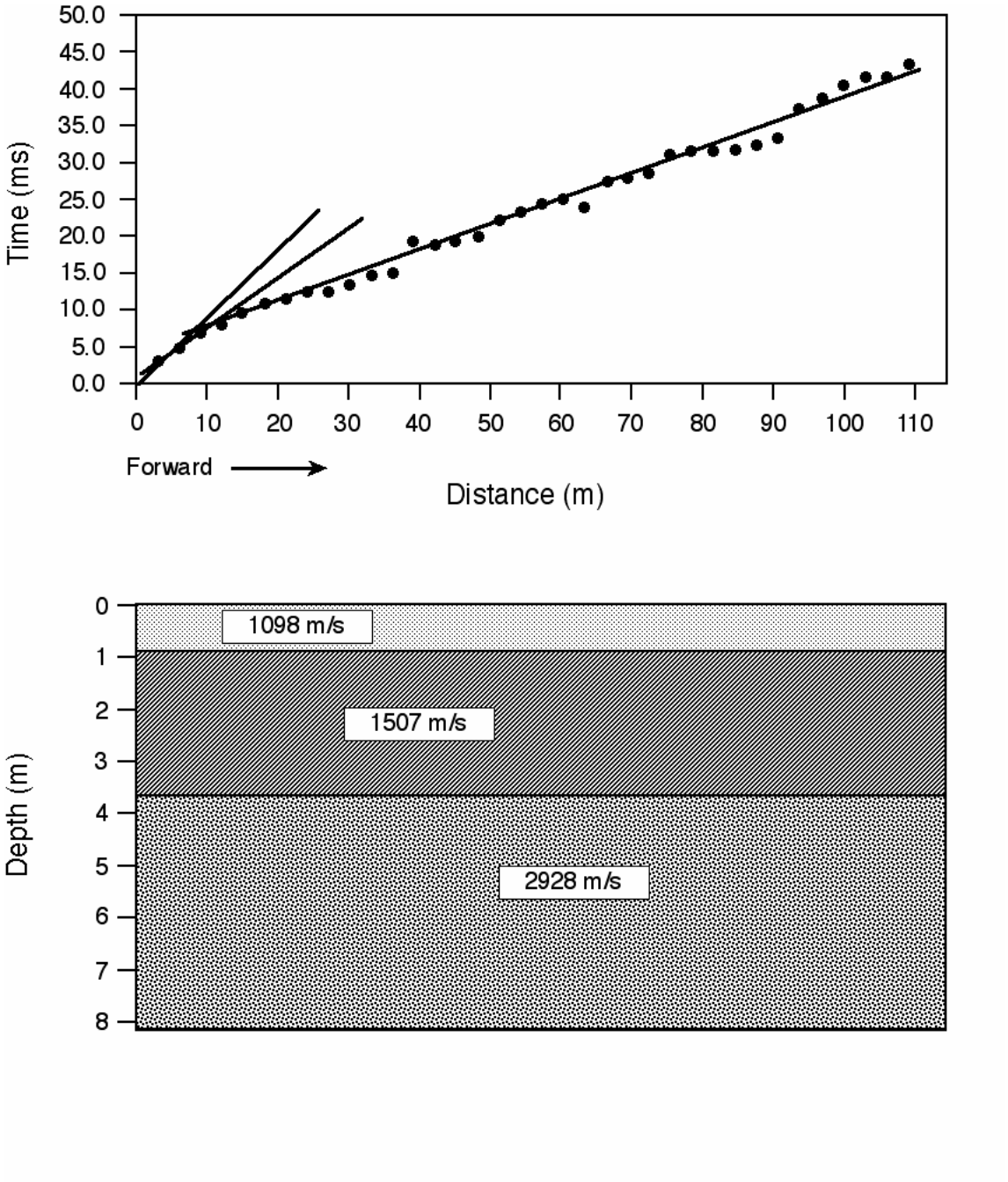

Figure B.1: P-wave refraction model, from Shot Point A, Spread A, north side

Appendix C: S Wave Travel Time Data, North and South Sides

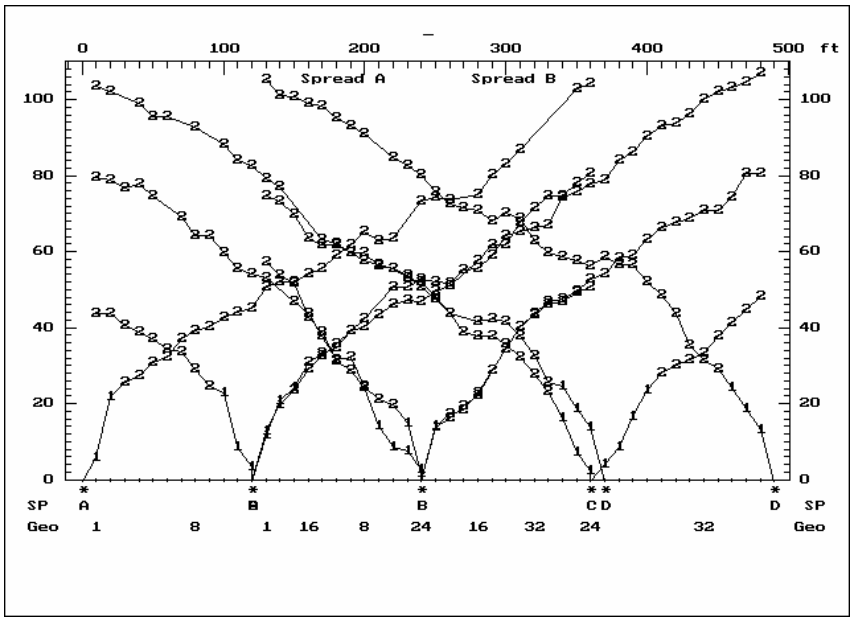

Figure C.1: S Wave Travel Time Curve, North Side.

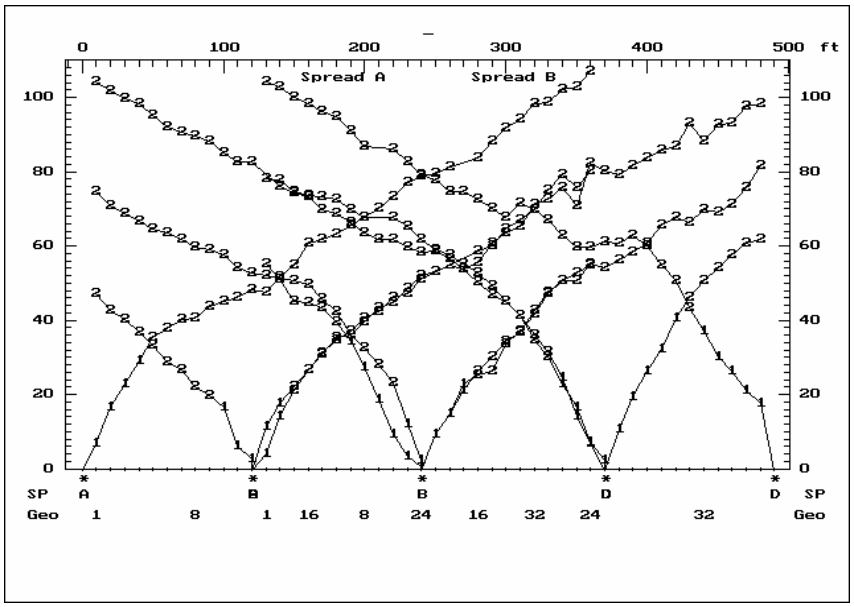

Figure C.2: S Wave Travel Time Curve, South Side.

Appendix D: S Wave Refraction Model

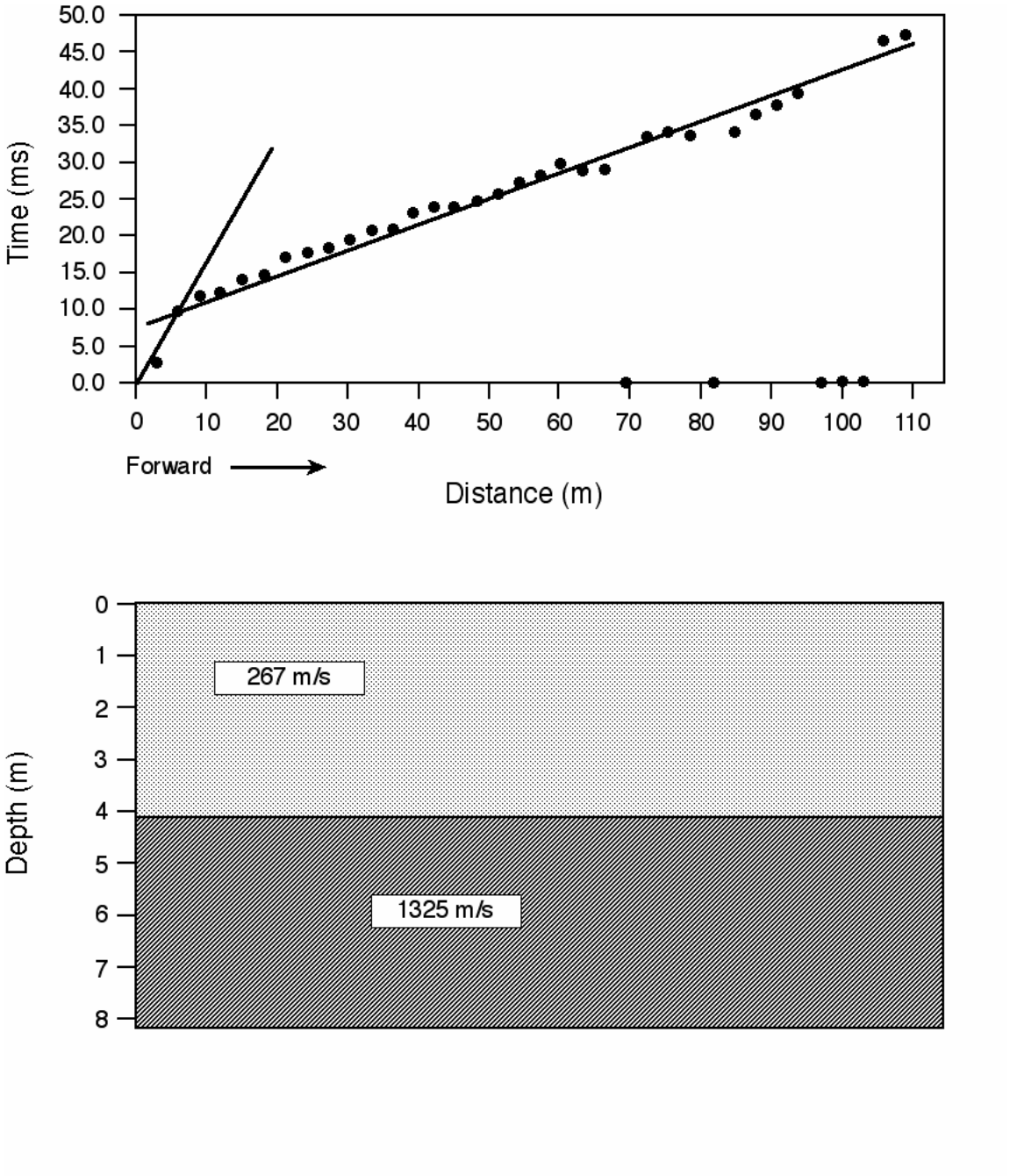

Figure D.1: S-wave refraction model, from Shot Point D, Spread A, north side.

Appendix E: Gravity Data Spreadsheets

Table E.1: Instrument Drift for Gravimeter

Station	Reading 1	Reading 2	Time 1	Time 2	Instrument Drift Between Bases (Dial Divisions/min)	Total Drift (Dial Divisions)
Base 1	3576.620	3576.620	10:16	10:17		
Base 2	3576.650	3576.650	11:18	11:18	-0.000483871	-0.030
Base 3	3576.650	3576.650	11:44	11:45	0	0.000
Base 4	3576.710	3576.710	12:45	12:46	-0.000983607	-0.060
Base 5	3576.700	3576.700	13:44	13:45	0.000169492	0.010
Base 6	3576.690	3576.690	14:47	14:47	0.00015873	0.010
Base 7	3576.680	3576.680	15:40	15:41	0.000188679	0.010

Table E.2: Gravity Data, North Side
Jackson County Site, Part 1

Station	Reading 1	Reading 2	Reading 3	Time	dt	Corrected Reading	Reading (mGal)	Elevation (m)	Free Air (mGal)	Bouguer (mGal)	Latitude Corection (mGal)	Bouguer Anomaly (mGal)	Smoothed Bouguer Anomaly (mGal)
Base	**3576.62**	**3576.62**		**10:17**	**0.0**	**3576.620**							
1	3576.82	3576.82		10:22	5.0	3576.818	3787.134	267.243	82.470	22.411	-7.32E-03	3847.187	3847.187
2	3576.82	3576.82		10:25	9.0	3576.816	3787.132	267.271	82.479	22.413	-7.32E-03	3847.191	3847.189
3	3576.81	3576.81		10:28	12.0	3576.804	3787.120	267.309	82.491	22.416	-7.32E-03	3847.187	3847.190
4	3576.81	3576.81		10:32	16.0	3576.802	3787.118	267.347	82.502	22.419	-7.32E-03	3847.194	3847.191
5	3576.80	3576.80		10:36	19.0	3576.791	3787.106	267.372	82.510	22.421	-7.32E-03	3847.187	3847.188
6	3576.80	3576.79	3576.79	10:39	22.0	3576.779	3787.094	267.409	82.521	22.424	-7.32E-03	3847.184	3847.183
7	3576.78	3576.78		10:42	26.0	3576.767	3787.081	267.439	82.531	22.427	-7.32E-03	3847.178	3847.180
8	3576.78	3576.78		10:45	29.0	3576.766	3787.080	267.468	82.540	22.429	-7.32E-03	3847.183	3847.180
9	3576.77	3576.77		10:48	32.0	3576.755	3787.068	267.506	82.551	22.433	-7.32E-03	3847.179	3847.179
10	3576.76	3576.76		10:51	34.0	3576.744	3787.056	267.534	82.560	22.435	-7.32E-03	3847.174	3847.176
11	3576.76	3576.76		10:54	37.0	3576.742	3787.055	267.552	82.566	22.436	-7.32E-03	3847.176	3847.177
12	3576.76	3576.76		10:57	40.0	3576.741	3787.053	267.580	82.574	22.439	-7.32E-03	3847.181	3847.178
13	3576.75	3576.75		11:01	44.0	3576.729	3787.040	267.610	82.583	22.441	-7.32E-03	3847.175	3847.178
14	3576.74	3576.75	3576.75	11:04	47.0	3576.727	3787.039	267.634	82.591	22.443	-7.32E-03	3847.179	3847.177
15	3576.74	3576.74		11:08	51.0	3576.715	3787.026	267.665	82.600	22.446	-7.32E-03	3847.173	3847.171
16	3576.72	3576.72	3576.72	11:11	54.0	3576.694	3787.003	267.703	82.612	22.449	-7.32E-03	3847.159	3847.158
17	3576.70	3576.70		11:15	58.0	3576.672	3786.980	267.721	82.618	22.451	-7.32E-03	3847.140	3847.146
Base	**3576.65**	**3576.65**		**11:18**	**0.0**	**3576.650**							
18	3576.70	3576.70		11:21	3.0	3576.670	3786.978	267.757	82.629	22.454	-7.32E-03	3847.146	3847.143
19	3576.69	3576.69		11:24	6.0	3576.660	3786.968	267.770	82.633	22.455	-7.32E-03	3847.138	3847.139
20	3576.68	3576.68		11:28	9.0	3576.650	3786.957	267.796	82.641	22.457	-7.32E-03	3847.134	3847.136
21	3576.68	3576.68		11:31	12.0	3576.650	3786.957	267.816	82.647	22.459	-7.32E-03	3847.138	3847.138
22	3576.68	3576.68		11:33	15.0	3576.650	3786.957	267.843	82.655	22.461	-7.32E-03	3847.144	3847.138
23	3576.66	3576.66		11:36	18.0	3576.630	3786.936	267.861	82.661	22.462	-7.32E-03	3847.127	3847.133
24	3576.66	3576.66		11:41	21.0	3576.630	3786.936	267.885	82.668	22.464	-7.32E-03	3847.132	3847.130
25/base	**3576.65**	**3576.65**		**11:45**	**0.0**	**3576.620**	**3786.925**	**267.914**	**82.677**	22.467	-7.32E-03	3847.128	3847.130

Table E.2: Gravity Data, North Side
Jackson County Site, Part 2

26	3576.65	3576.65		11:48	3.0	3576.617	3786.922	267.943	82.686	22.469	-7.32E-03	3847.132	3847.129
27	3576.64	3576.64		11:51	6.0	3576.604	3786.908	267.969	82.694	22.471	-7.32E-03	3847.124	3847.127
28	3576.63	3576.64	3576.64	11:54	10.0	3576.600	3786.904	268.003	82.705	22.474	-7.32E-03	3847.127	3847.125
29	3576.63	3576.63		11:57	13.0	3576.587	3786.891	268.032	82.714	22.477	-7.32E-03	3847.120	3847.120
30	3576.62	3576.62		12:00	15.0	3576.575	3786.878	268.059	82.722	22.479	-7.32E-03	3847.114	3847.115
31	3576.62	3576.62		12:03	18.0	3576.572	3786.875	268.076	82.727	22.480	-7.32E-03	3847.114	3847.112
32	3576.61	3576.61		12:06	21.0	3576.559	3786.861	268.107	82.737	22.483	-7.32E-03	3847.107	3847.122
33	3576.66	3576.66		12:13	28.0	3576.602	3786.907	268.125	82.742	22.485	-7.32E-03	3847.157	3847.143
34	3576.65	3576.65		12:16	31.0	3576.590	3786.893	268.147	82.749	22.486	-7.32E-03	3847.148	3847.148
35	3576.64	3576.64		12:19	35.0	3576.576	3786.878	268.173	82.757	22.489	-7.32E-03	3847.139	3847.144
36	3576.65	3576.65		12:23	38.0	3576.583	3786.886	268.181	82.760	22.489	-7.32E-03	3847.149	3847.146
37	3576.64	3576.64		12:25	40.0	3576.571	3786.873	268.235	82.776	22.494	-7.32E-03	3847.148	3847.147
38	3576.63	3576.63		12:29	44.0	3576.557	3786.858	268.273	82.788	22.497	-7.32E-03	3847.142	3847.144
39	3576.62	3576.63	3576.63	12:32	48.0	3576.553	3786.854	268.301	82.797	22.499	-7.32E-03	3847.144	3847.142
40	3576.62	3576.62		12:36	51.0	3576.540	3786.840	268.341	82.809	22.503	-7.32E-03	3847.139	3847.138
41	3576.61	3576.61		12:39	54.0	3576.527	3786.827	268.359	82.815	22.504	-7.32E-03	3847.130	3847.134
42	3576.61	3576.61		12:42	57.0	3576.524	3786.824	268.399	82.827	22.507	-7.32E-03	3847.136	3847.135
Base	**3576.71**	**3576.71**		**12:46**	**0.0**	**3576.620**							
43	3576.61	3576.61		12:51	5.0	3576.521	3786.820	268.431	82.837	22.510	-7.32E-03	3847.140	3847.140
44	3576.61	3576.61		12:55	9.0	3576.522	3786.821	268.461	82.846	22.513	-7.32E-03	3847.147	3847.145
45	3576.60	3576.60		12:58	12.0	3576.512	3786.811	268.495	82.857	22.516	-7.32E-03	3847.145	3847.144
46	3576.59	3576.59		13:01	15.0	3576.503	3786.801	268.519	82.864	22.518	-7.32E-03	3847.140	3847.140
47	3576.58	3576.58		13:05	19.0	3576.493	3786.791	268.550	82.873	22.520	-7.32E-03	3847.137	3847.135
48	3576.56	3576.56		13:08	22.0	3576.474	3786.770	268.590	82.886	22.524	-7.32E-03	3847.125	3847.125

Appendix F: P-wave Travel-Time Curves

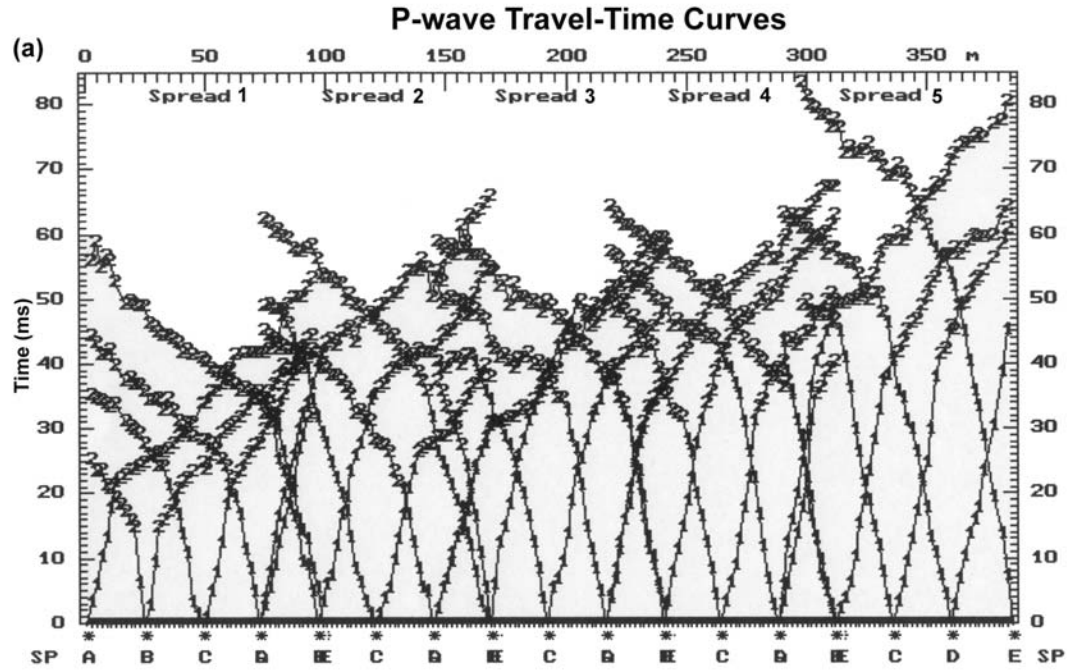
P-wave Travel-Time Curves
(a)
0 50 100 150 200 250 300 350 m
Spread 1
Spread 2
Spread 3
Spread 4
Spread 5
Time (ms)
0 10 20 30 40 50 60 70 80
SP A B C D E C D E C D E C D E C D E SP

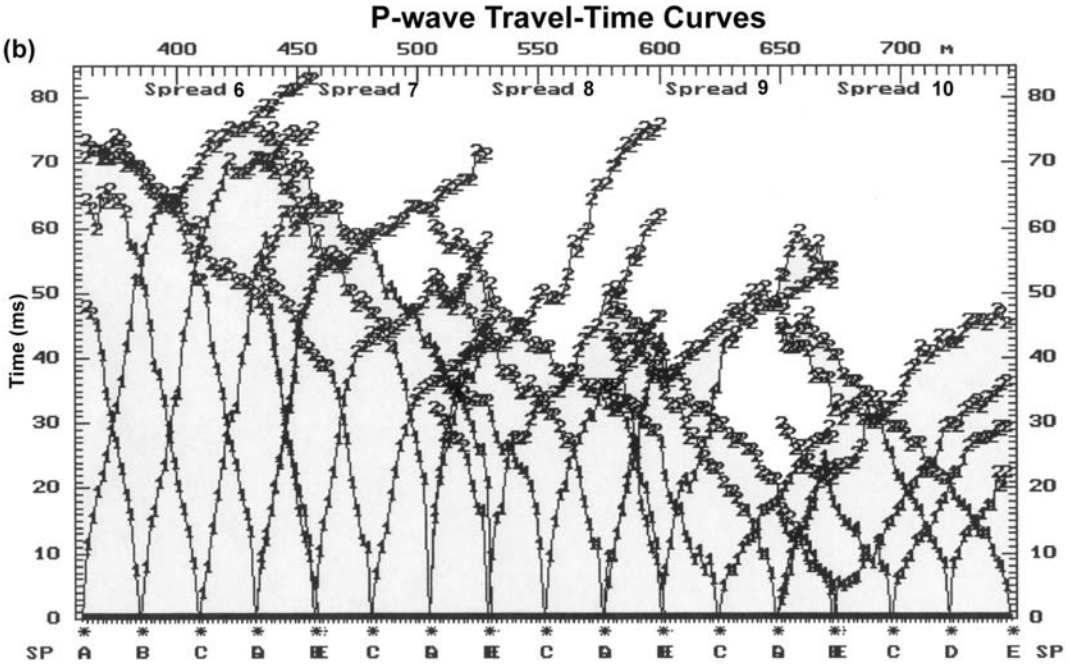
P-wave Travel-Time Curves
(b)
400 450 500 550 600 650 700 m
Spread 6
Spread 7
Spread 8
Spread 9
Spread 10
Time (ms)
0 10 20 30 40 50 60 70 80
SP A B C D E C D E C D E C D E C D E SP

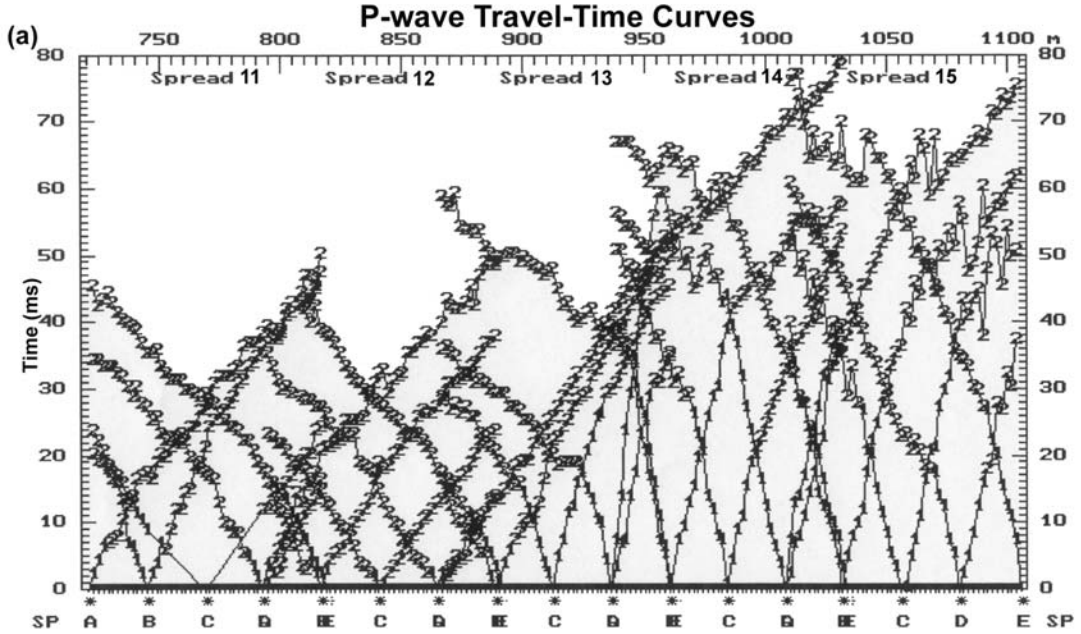
(a)
P-wave Travel-Time Curves
750 800 850 900 950 1000 1050 1100 m
Spread 11
Spread 12
Spread 13
Spread 14
Spread 15
Time (ms)
0 10 20 30 40 50 60 70 80
SP A B C D E C D E C D E C D E C D E SP

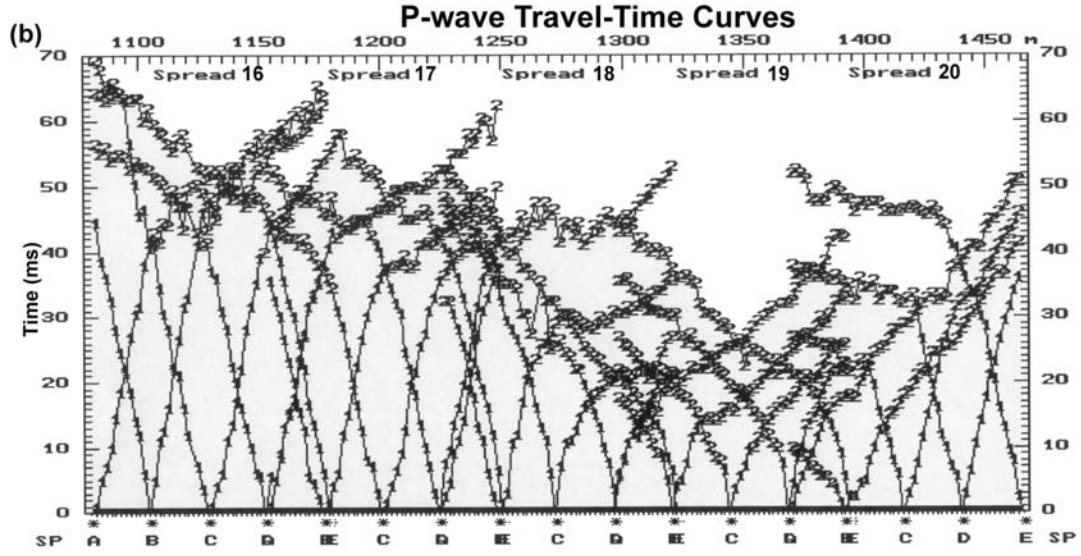
(b)
P-wave Travel-Time Curves
1100 1150 1200 1250 1300 1350 1400 1450 m
Spread 16
Spread 17
Spread 18
Spread 19
Spread 20
Time (ms)
0 10 20 30 40 50 60 70
SP A B C D E C D E C D E C D E C D E SP

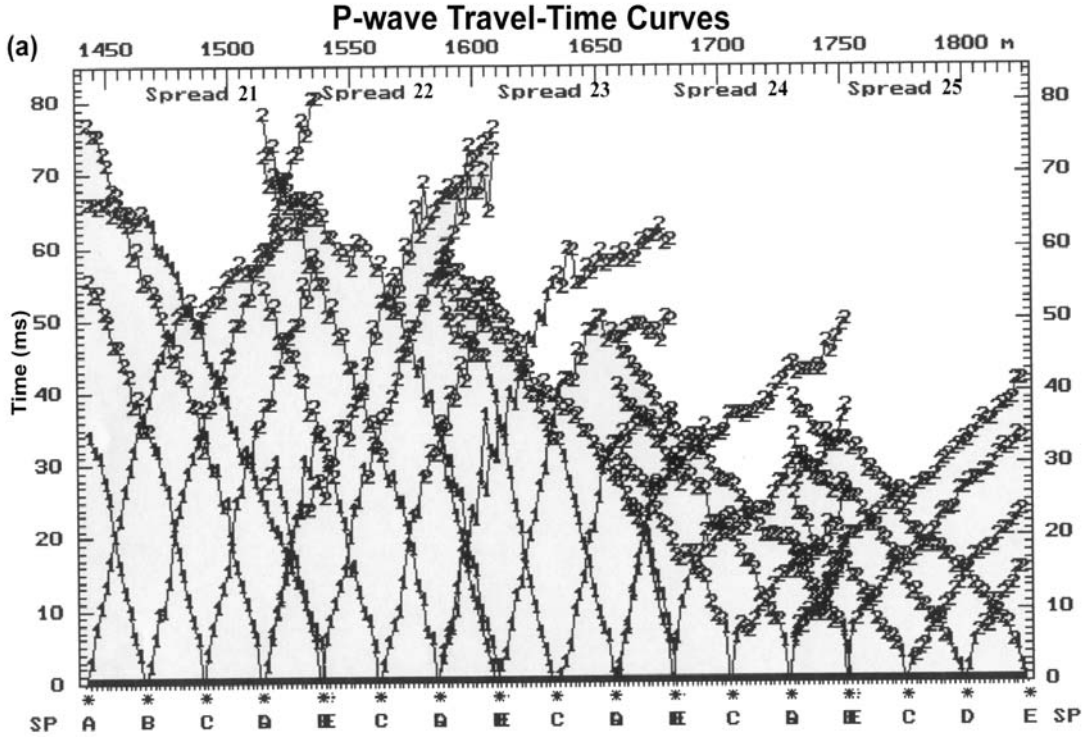
P-wave Travel-Time Curves
(a)
1450 1500 1550 1600 1650 1700 1750 1800 m
Spread 21
Spread 22
Spread 23
Spread 24
Spread 25
Time (ms)
0 10 20 30 40 50 60 70 80
SP A B C D E C D E C D E C D E C D E SP

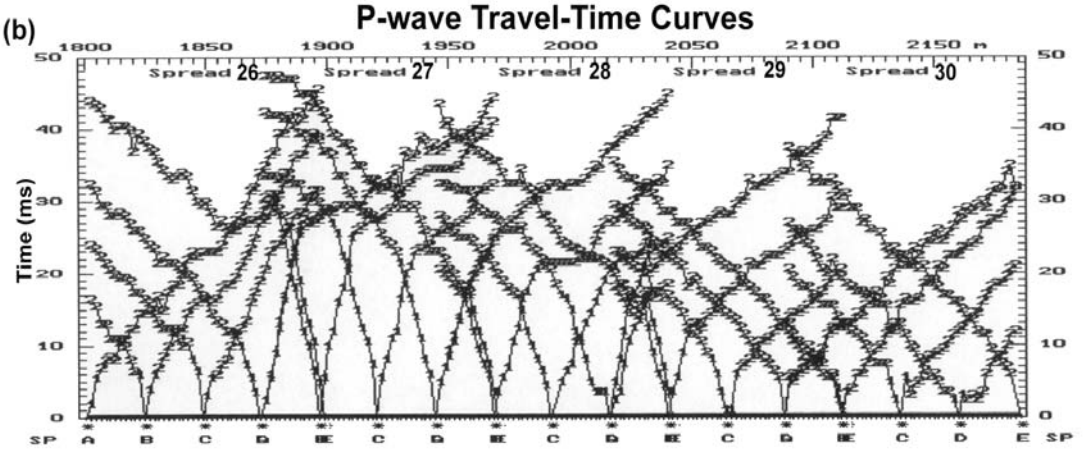
P-wave Travel-Time Curves
(b)
1800 1850 1900 1950 2000 2050 2100 2150 m
Spread 26
Spread 27
Spread 28
Spread 29
Spread 30
Time (ms)
0 10 20 30 40 50
SP A B C D E C D E C D E C D E C D E SP

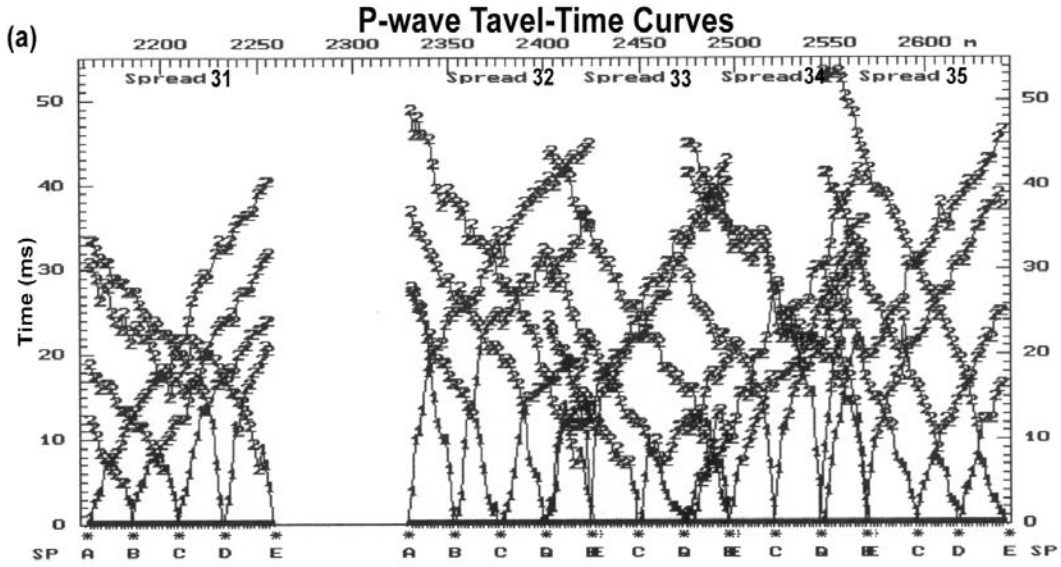
(a)
P-wave Tavel-Time Curves
2200 2250 2300 2350 2400 2450 2500 2550 2600 m
Spread 31
Spread 32
Spread 33
Spread 34
Spread 35
Time (ms)
0 10 20 30 40 50
SP A B C D E A B C D E C D E C D E C D E SP

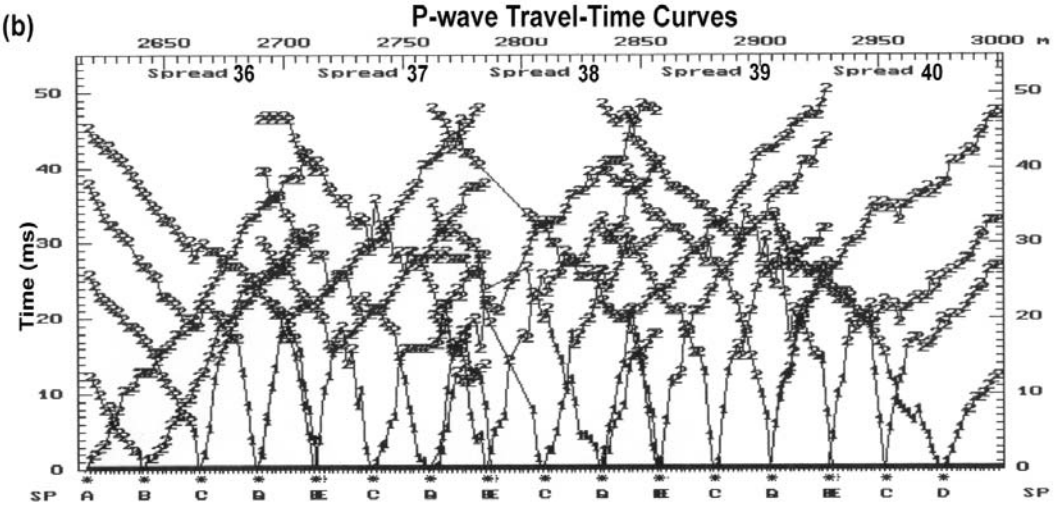
(b)
P-wave Travel-Time Curves
2650 2700 2750 2800 2850 2900 2950 3000 m
Spread 36
Spread 37
Spread 38
Spread 39
Spread 40
Time (ms)
0 10 20 30 40 50
SP A B C D E C D E C D E C D E C D SP

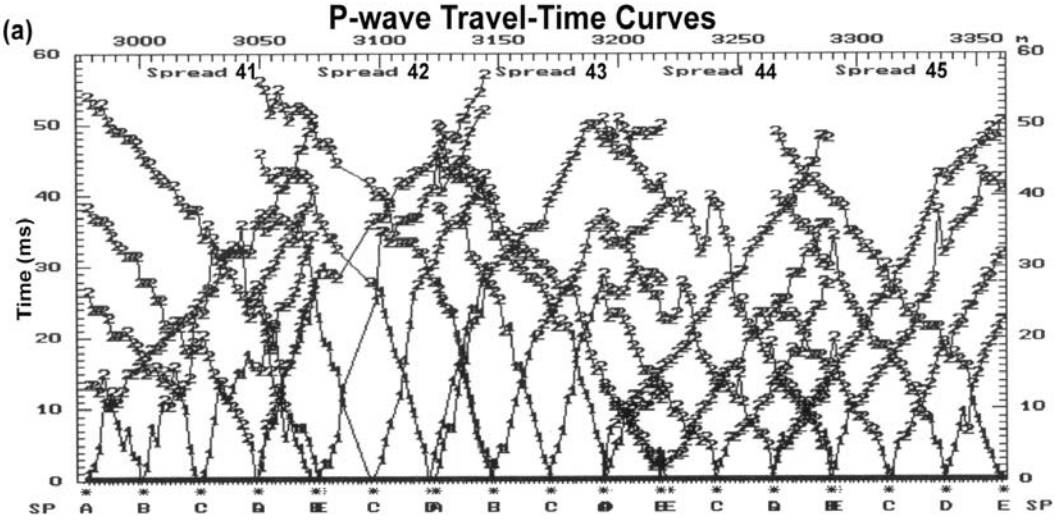
(a)
P-wave Travel-Time Curves
3000
3050
3100
3150
3200
3250
3300
3350 m
Spread 41
Spread 42
Spread 43
Spread 44
Spread 45
Time (ms)
0
10
20
30
40
50
60
SP A B C D E C D B C D E C D E C D E SP

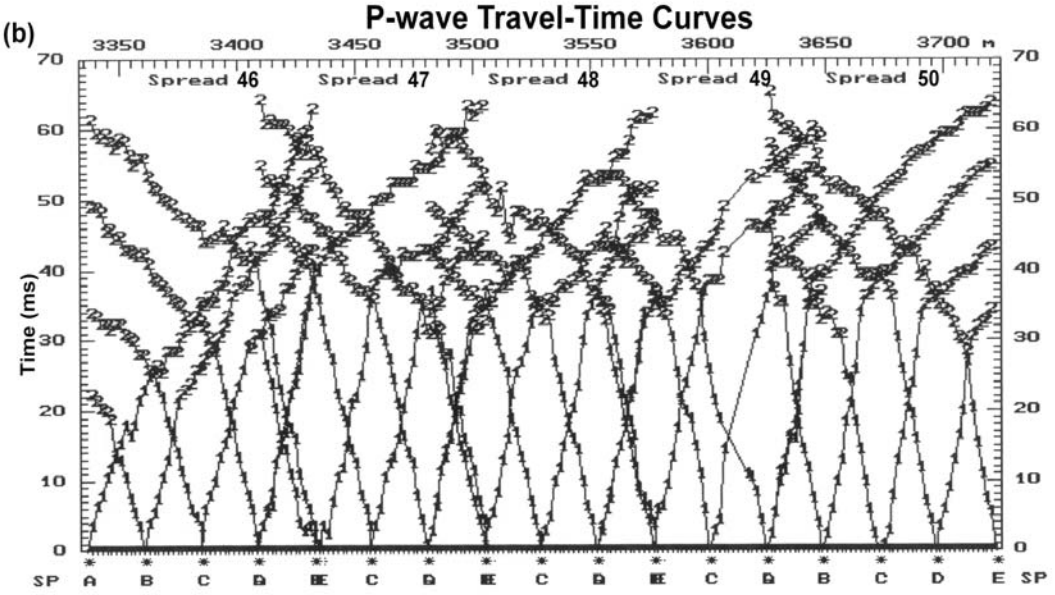
(b)
P-wave Travel-Time Curves
3350
3400
3450
3500
3550
3600
3650
3700 m
Spread 46
Spread 47
Spread 48
Spread 49
Spread 50
Time (ms)
0
10
20
30
40
50
60
70
SP A B C D E C D E C D E C D B C D E SP

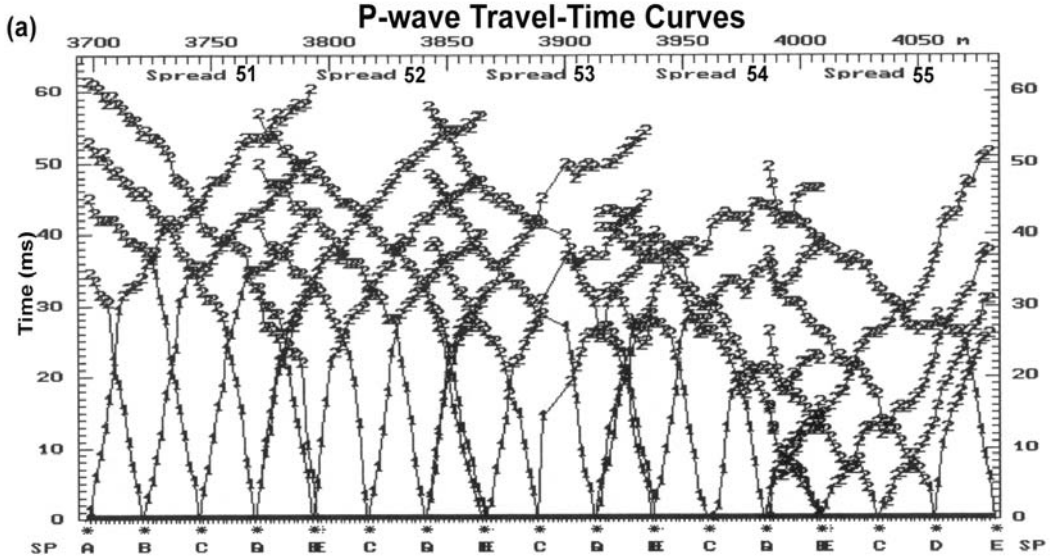
(a)
P-wave Travel-Time Curves
3700
3750
3800
3850
3900
3950
4000
4050 m
Spread 51
Spread 52
Spread 53
Spread 54
Spread 55
Time (ms)
0
10
20
30
40
50
60
SP
A
B
C
D
E
SP

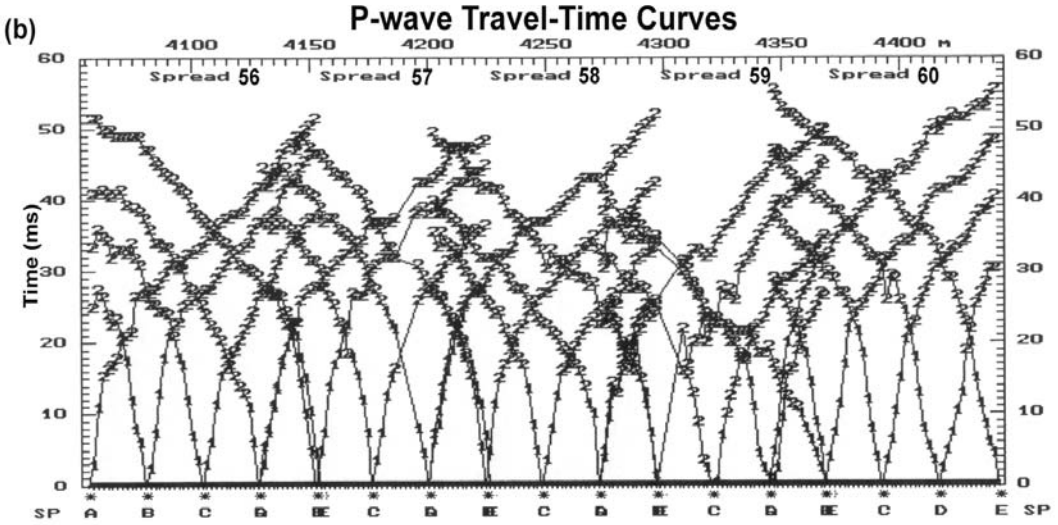
(b)
P-wave Travel-Time Curves
4100
4150
4200
4250
4300
4350
4400 m
Spread 56
Spread 57
Spread 58
Spread 59
Spread 60
Time (ms)
0
10
20
30
40
50
60
SP
A
B
C
D
E
SP

Appendix G: S-wave Travel-Time Curves

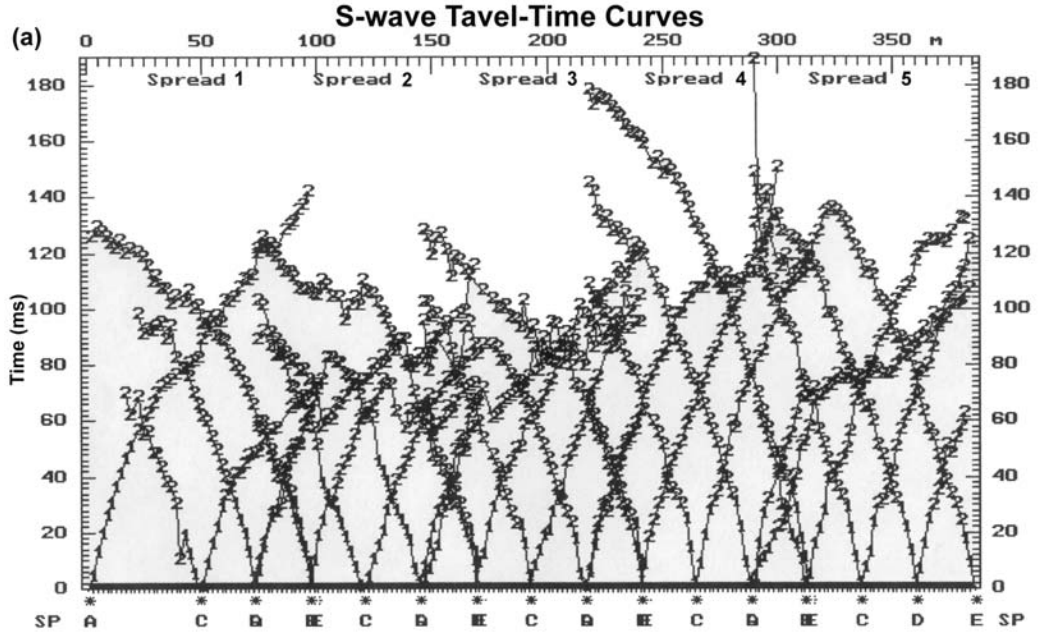
S-wave Tavel-Time Curves
(a)
0 50 100 150 200 250 300 350 m
Spread 1
Spread 2
Spread 3
Spread 4
Spread 5
Time (ms)
0 20 40 60 80 100 120 140 160 180
SP A C D E C D E C D E C D E C D E SP

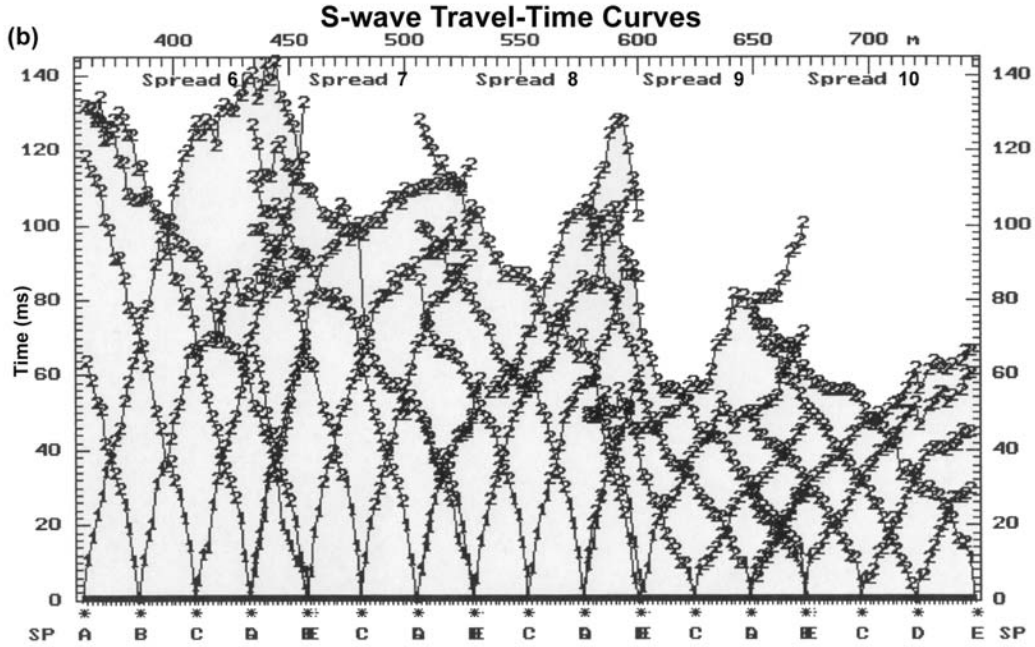
S-wave Travel-Time Curves
(b)
400 450 500 550 600 650 700 m
Spread 6
Spread 7
Spread 8
Spread 9
Spread 10
Time (ms)
0 20 40 60 80 100 120 140
SP A B C D E C D E C D E C D E C D E SP

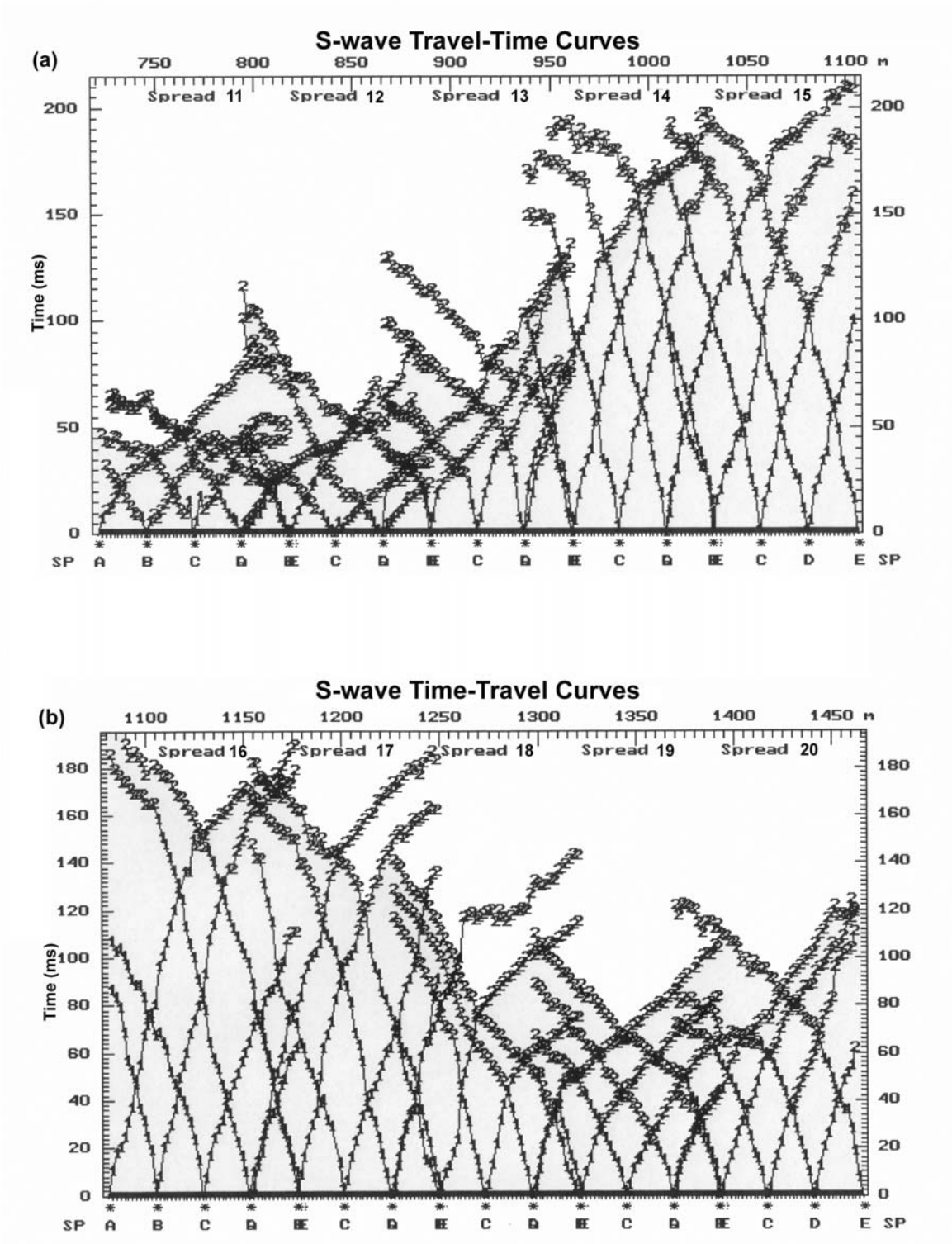
S-wave Travel-Time Curves
(a)
750 800 850 900 950 1000 1050 1100 m
Spread 11
Spread 12
Spread 13
Spread 14
Spread 15
Time (ms)
0 50 100 150 200
SP A B C D E C D E C D E C D E C D E SP
S-wave Time-Travel Curves
(b)
1100 1150 1200 1250 1300 1350 1400 1450 m
Spread 16
Spread 17
Spread 18
Spread 19
Spread 20
Time (ms)
0 20 40 60 80 100 120 140 160 180
SP A B C D E C D E C D E C D E C D E SP

Appendix H: P-wave Cross-Sectional Depth Models

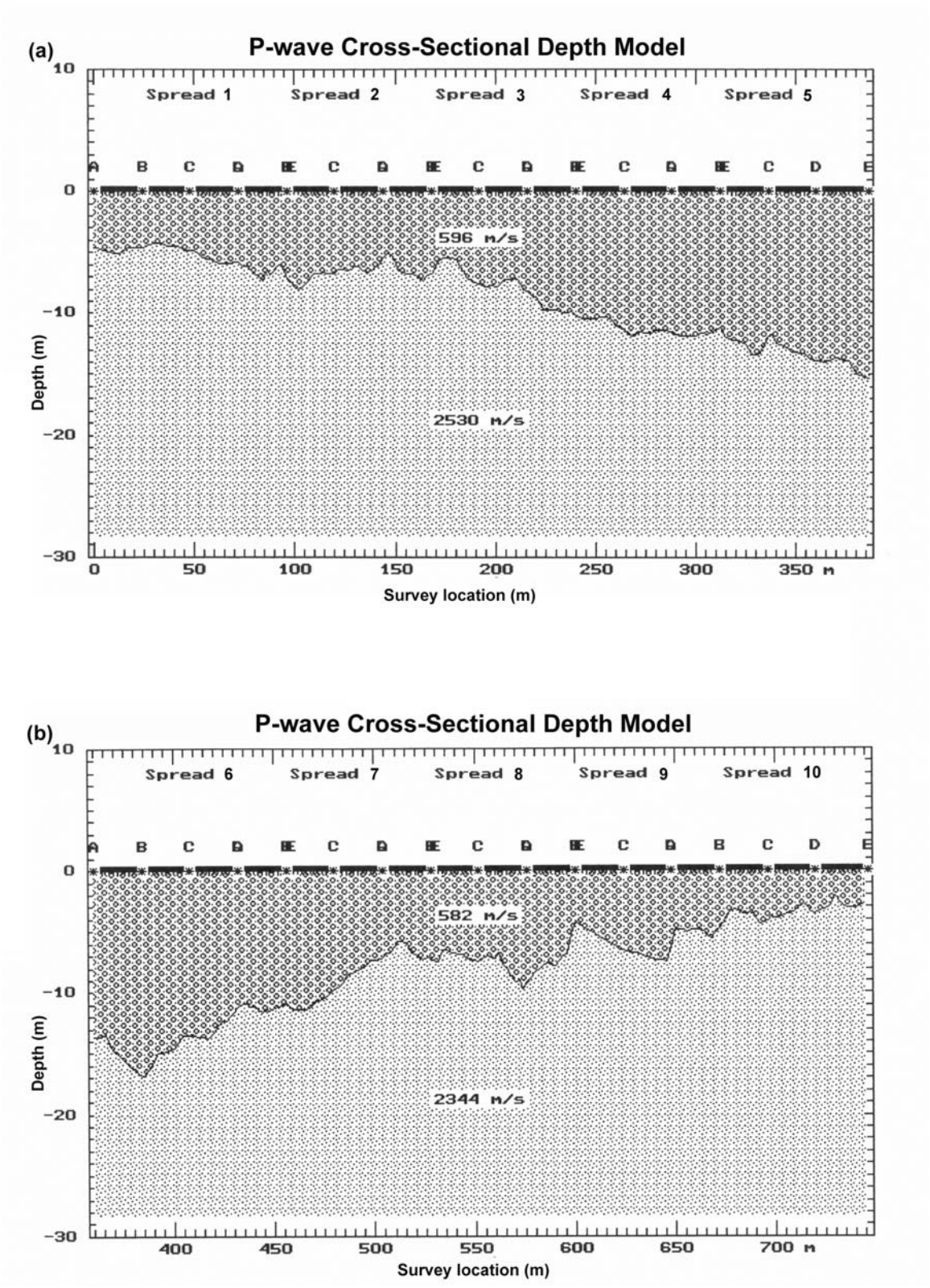
(a)
P-wave Cross-Sectional Depth Model
Spread 1
Spread 2
Spread 3
Spread 4
Spread 5
596 m/s
2530 m/s
Depth (m)
Survey location (m)
(b)
P-wave Cross-Sectional Depth Model
Spread 6
Spread 7
Spread 8
Spread 9
Spread 10
582 m/s
2344 m/s
Depth (m)
Survey location (m)

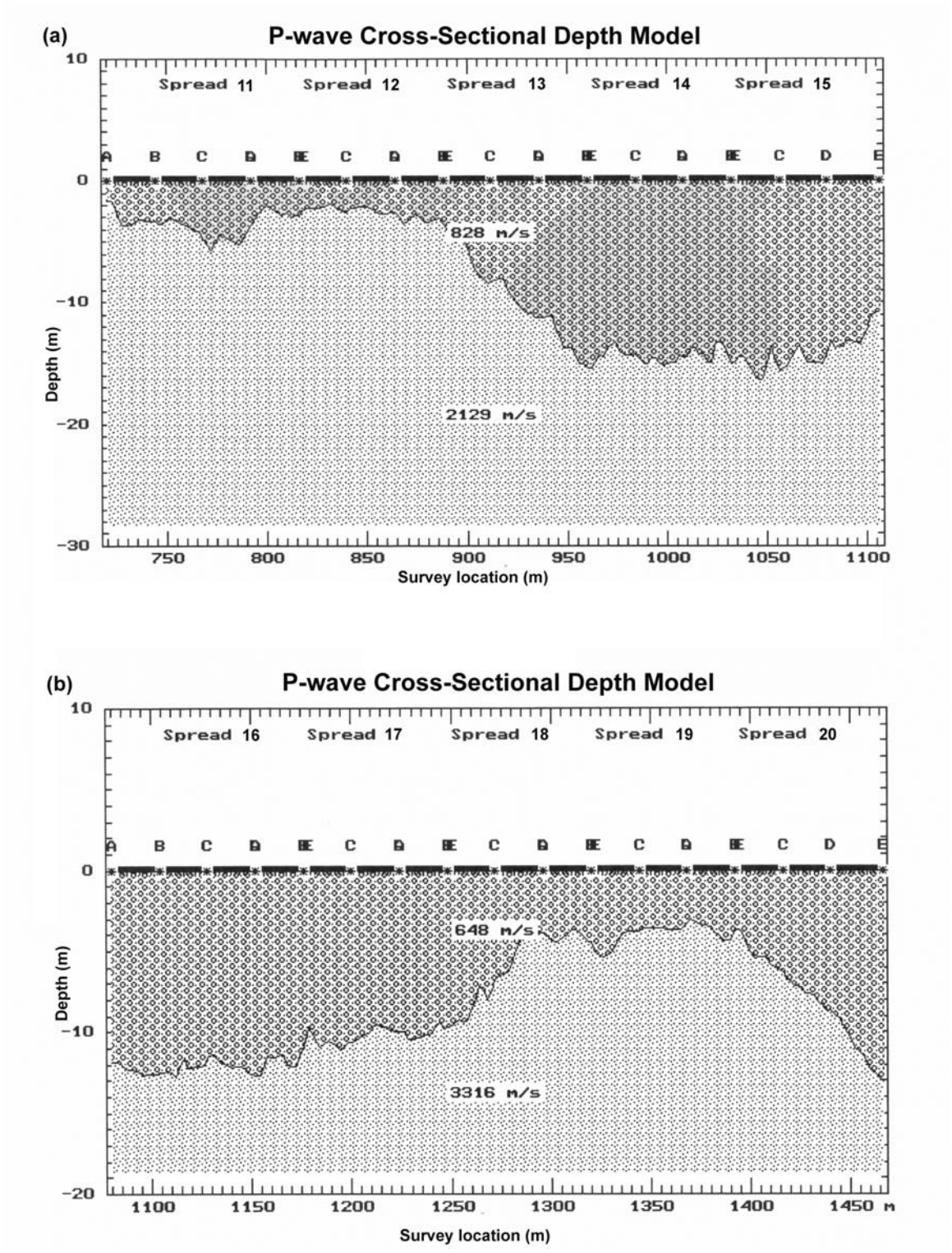
(a)
P-wave Cross-Sectional Depth Model
Spread 11
Spread 12
Spread 13
Spread 14
Spread 15
828 m/s
2129 m/s
Depth (m)
Survey location (m)
(b)
P-wave Cross-Sectional Depth Model
Spread 16
Spread 17
Spread 18
Spread 19
Spread 20
648 m/s
3316 m/s
Depth (m)
Survey location (m)

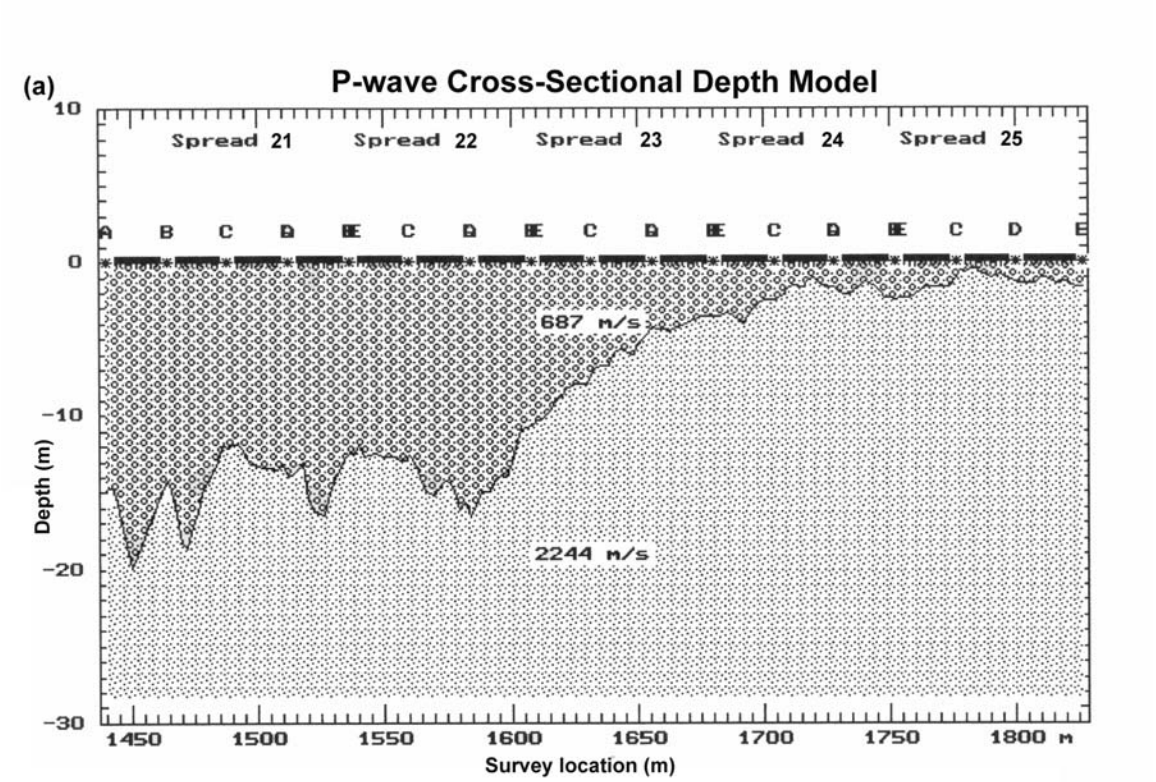
(a)
P-wave Cross-Sectional Depth Model
Spread 21
Spread 22
Spread 23
Spread 24
Spread 25
A B C D E C D E C D E C D E C D E
687 m/s
2244 m/s
Depth (m)
10
0
-10
-20
-30
1450
1500
1550
1600
1650
1700
1750
1800 m
Survey location (m)

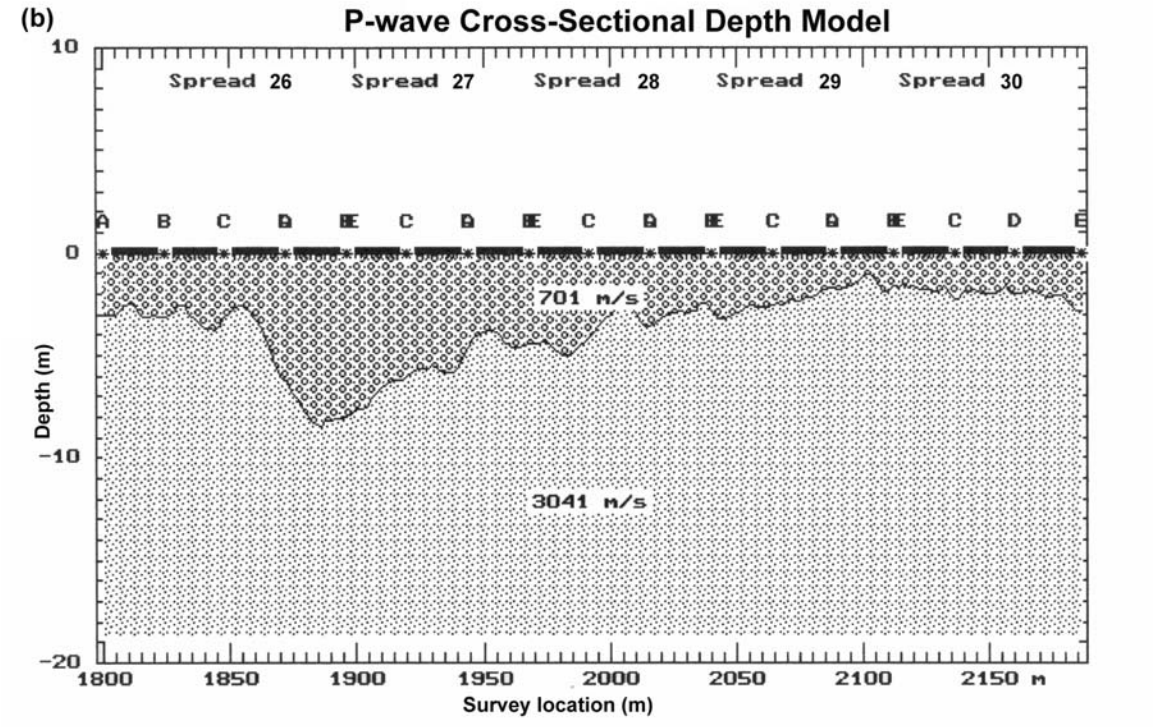
(b)
P-wave Cross-Sectional Depth Model
Spread 26
Spread 27
Spread 28
Spread 29
Spread 30
A B C D E C D E C D E C D E C D E
701 m/s
3041 m/s
Depth (m)
10
0
-10
-20
1800
1850
1900
1950
2000
2050
2100
2150 m
Survey location (m)

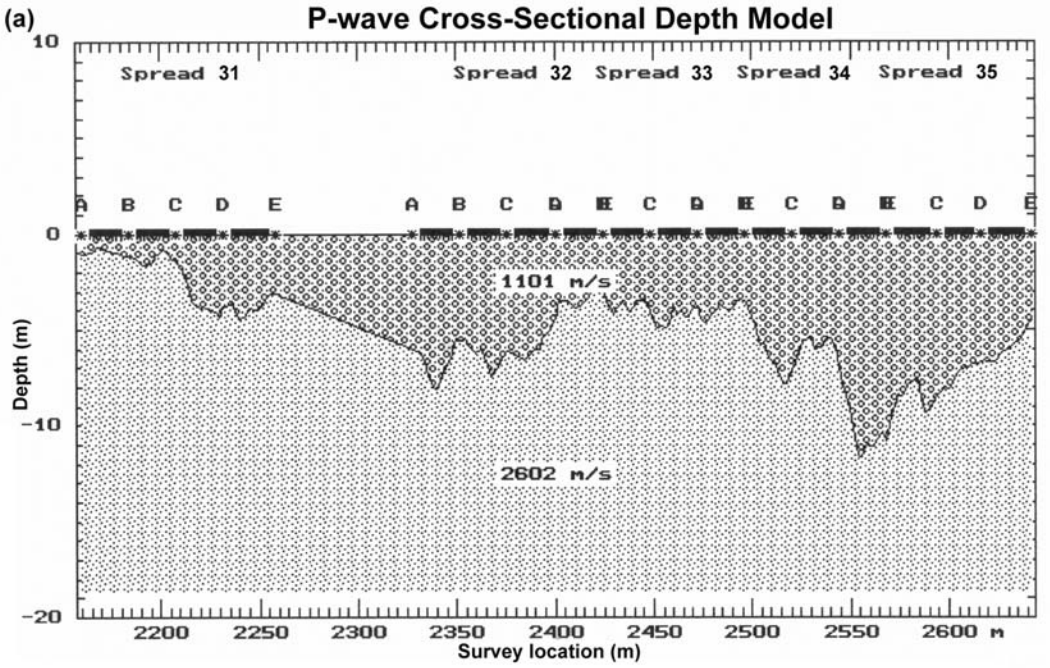
(a)
P-wave Cross-Sectional Depth Model
Spread 31
Spread 32
Spread 33
Spread 34
Spread 35
1101 m/s
2602 m/s
Depth (m)
Survey location (m)

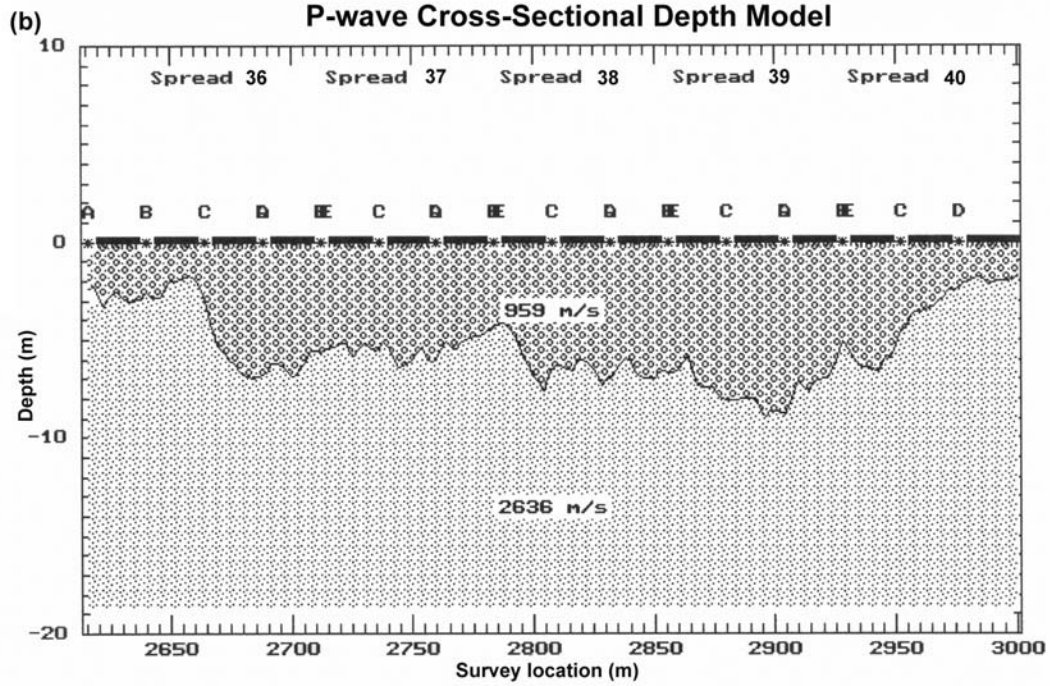
(b)
P-wave Cross-Sectional Depth Model
Spread 36
Spread 37
Spread 38
Spread 39
Spread 40
959 m/s
2636 m/s
Depth (m)
Survey location (m)

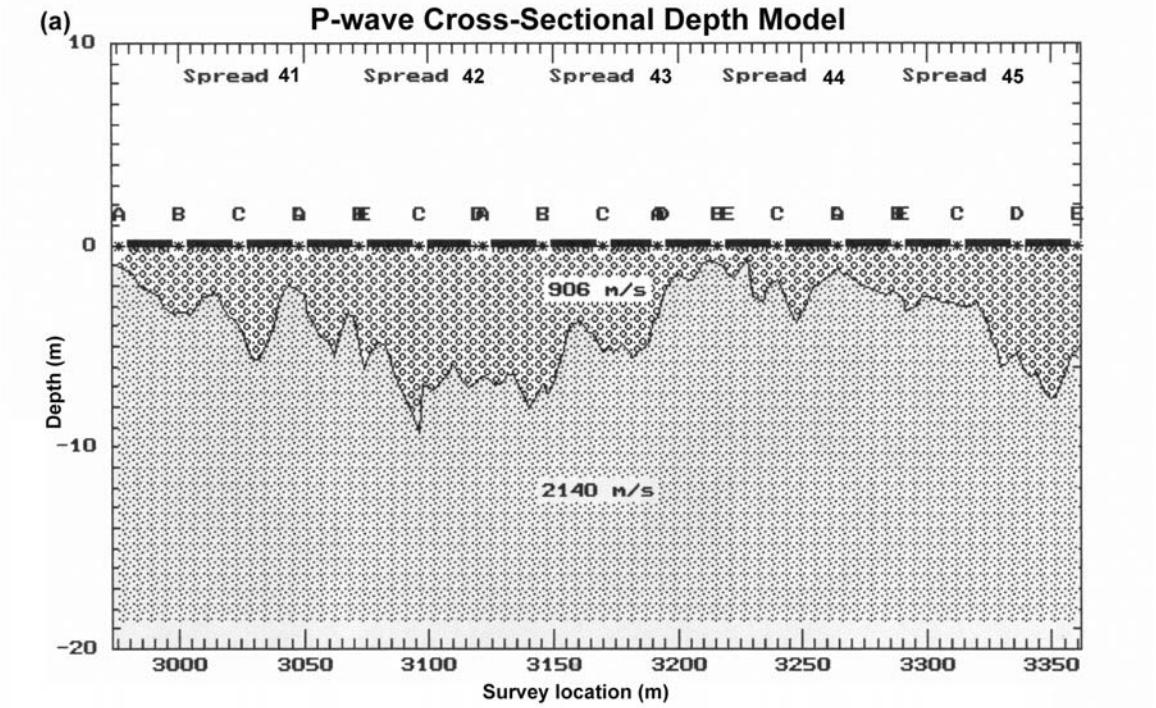
(a)
P-wave Cross-Sectional Depth Model
Spread 41
Spread 42
Spread 43
Spread 44
Spread 45
906 m/s
2140 m/s
Depth (m)
10
0
-10
-20
3000
3050
3100
3150
3200
3250
3300
3350
Survey location (m)

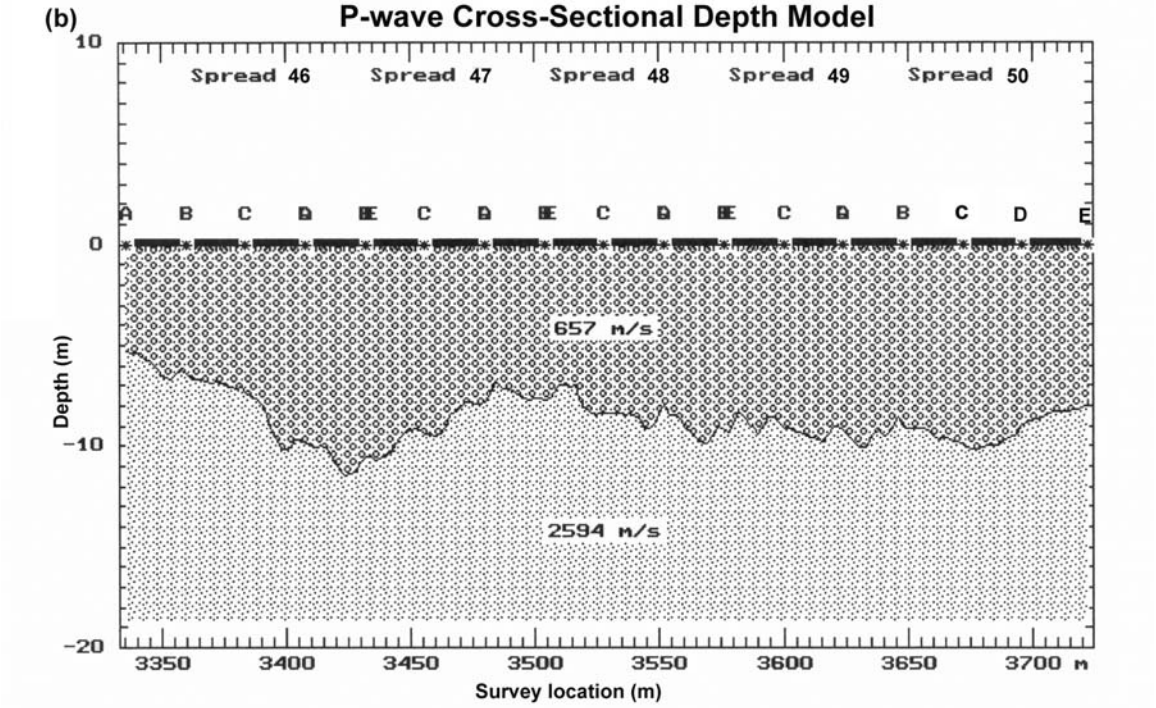
(b)
P-wave Cross-Sectional Depth Model
Spread 46
Spread 47
Spread 48
Spread 49
Spread 50
657 m/s
2594 m/s
Depth (m)
10
0
-10
-20
3350
3400
3450
3500
3550
3600
3650
3700 m
Survey location (m)

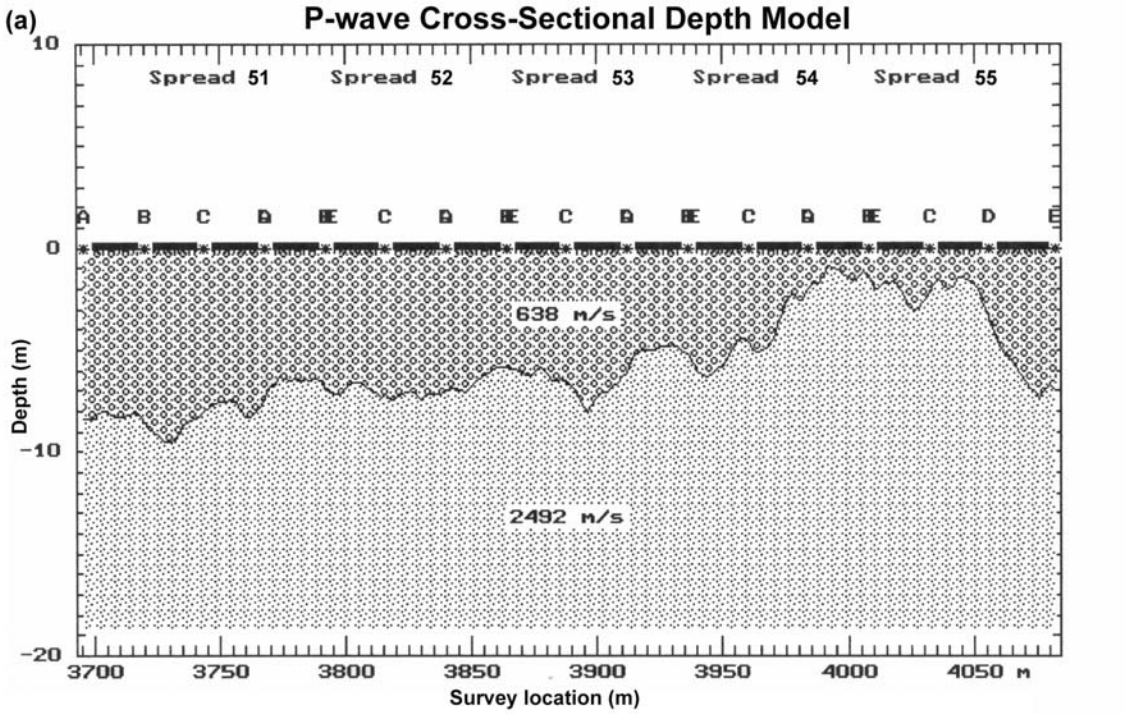
(a)
P-wave Cross-Sectional Depth Model
Spread 51
Spread 52
Spread 53
Spread 54
Spread 55
638 m/s
2492 m/s
Depth (m)
Survey location (m)

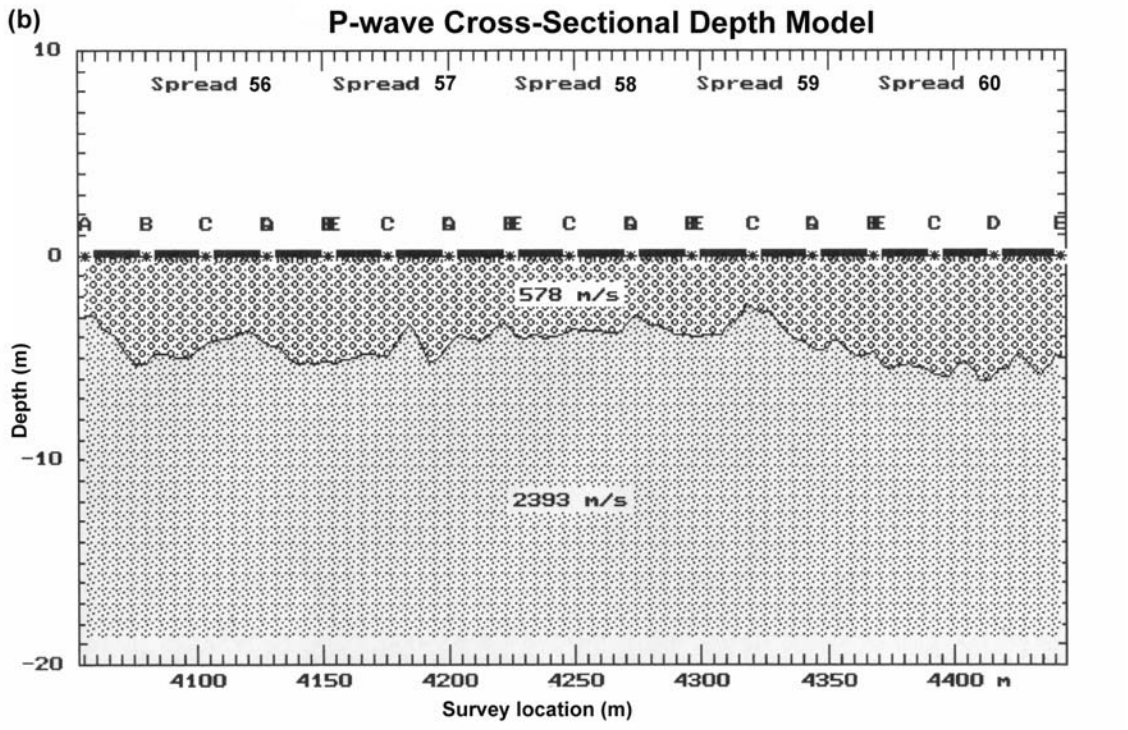
(b)
P-wave Cross-Sectional Depth Model
Spread 56
Spread 57
Spread 58
Spread 59
Spread 60
578 m/s
2393 m/s
Depth (m)
Survey location (m)

Appendix I: S-wave Cross-Sectional Depth Models

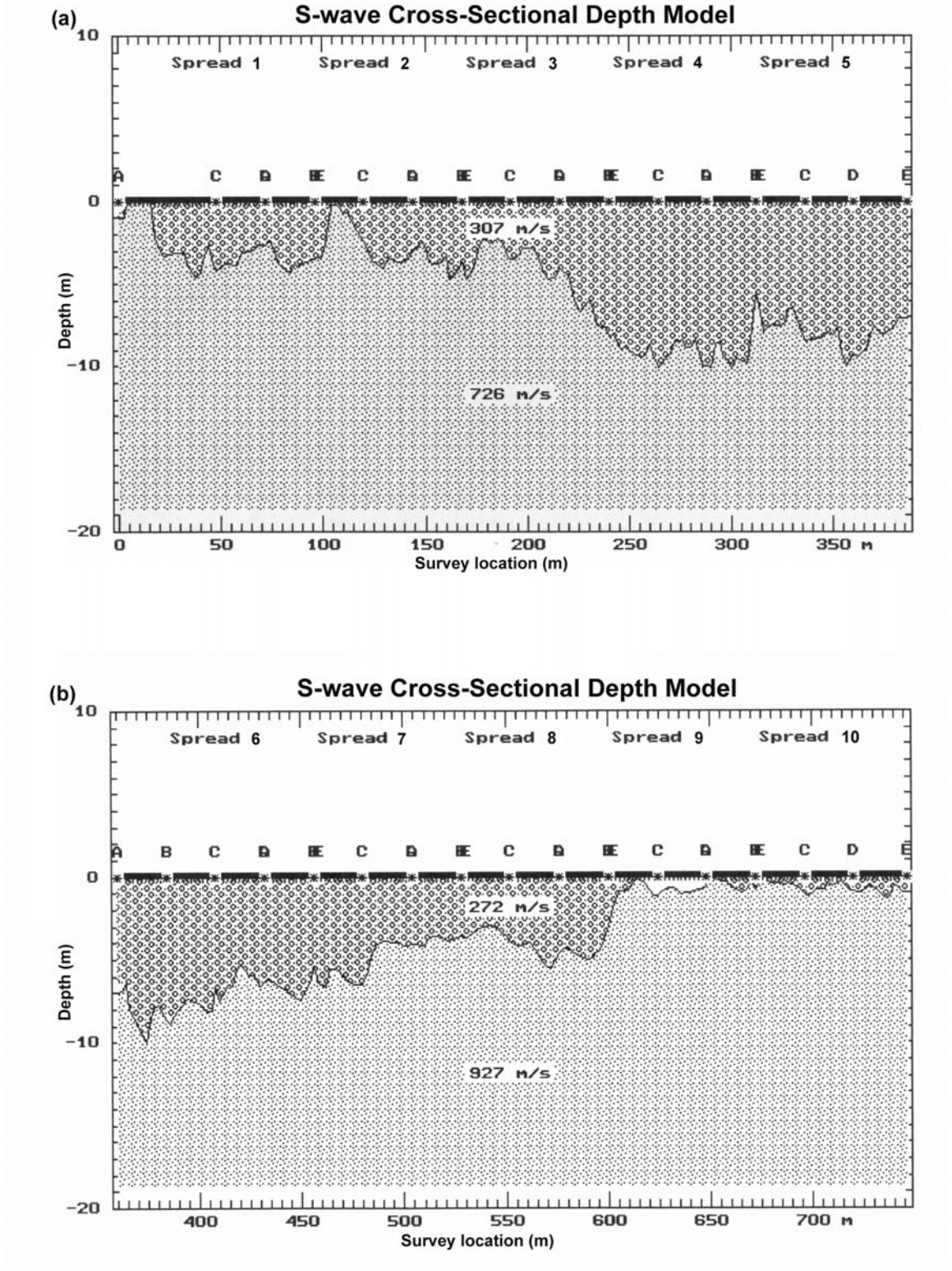
(a)
S-wave Cross-Sectional Depth Model
Spread 1
Spread 2
Spread 3
Spread 4
Spread 5
307 m/s
726 m/s
Depth (m)
Survey location (m)
(b)
S-wave Cross-Sectional Depth Model
Spread 6
Spread 7
Spread 8
Spread 9
Spread 10
272 m/s
927 m/s
Depth (m)
Survey location (m)

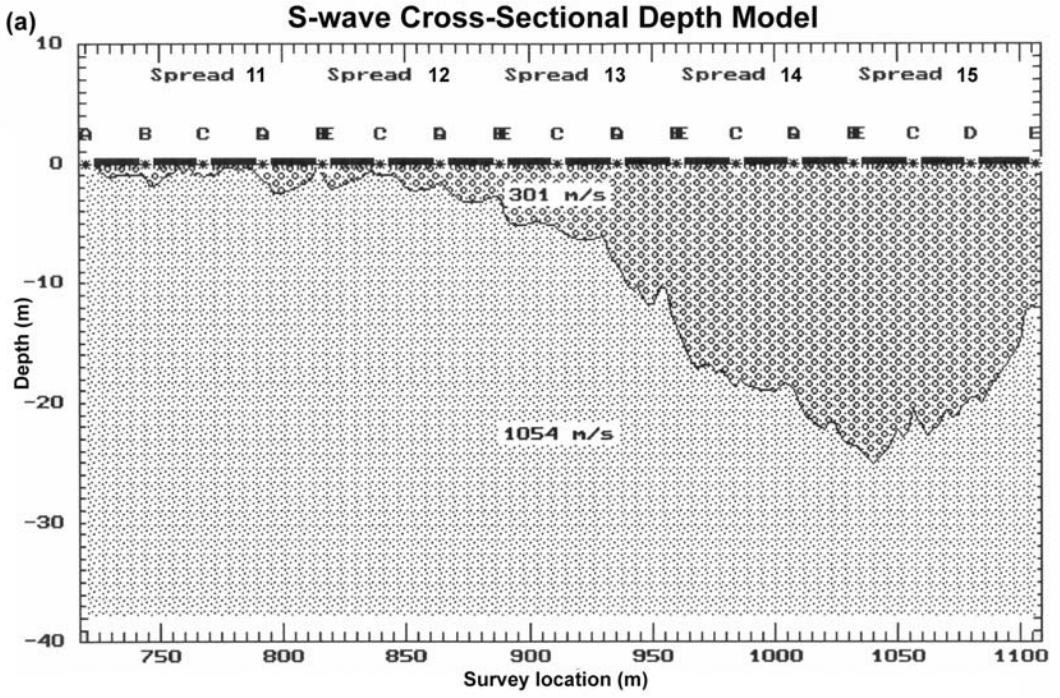
(a)
S-wave Cross-Sectional Depth Model
Spread 11
Spread 12
Spread 13
Spread 14
Spread 15
A B C D E C D E C D E C D E C D E
301 m/s
1054 m/s
Depth (m)
10
0
-10
-20
-30
-40
750
800
850
900
950
1000
1050
1100
Survey location (m)

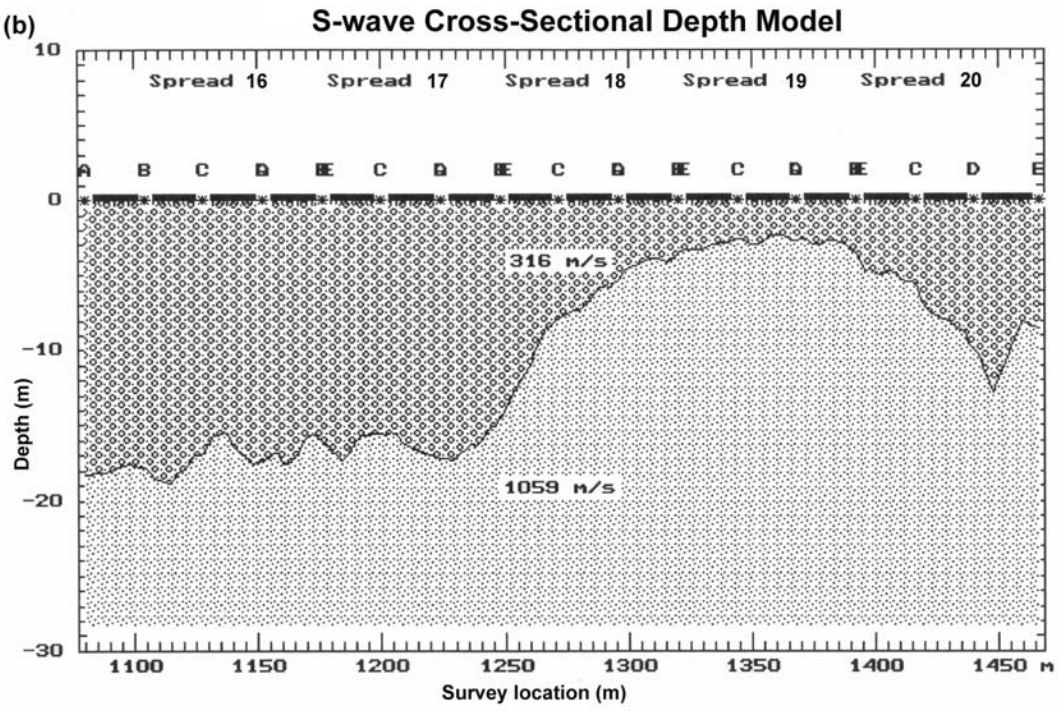
(b)
S-wave Cross-Sectional Depth Model
Spread 16
Spread 17
Spread 18
Spread 19
Spread 20
A B C D E C D E C D E C D E C D E
316 m/s
1059 m/s
Depth (m)
10
0
-10
-20
-30
1100
1150
1200
1250
1300
1350
1400
1450 m
Survey location (m)

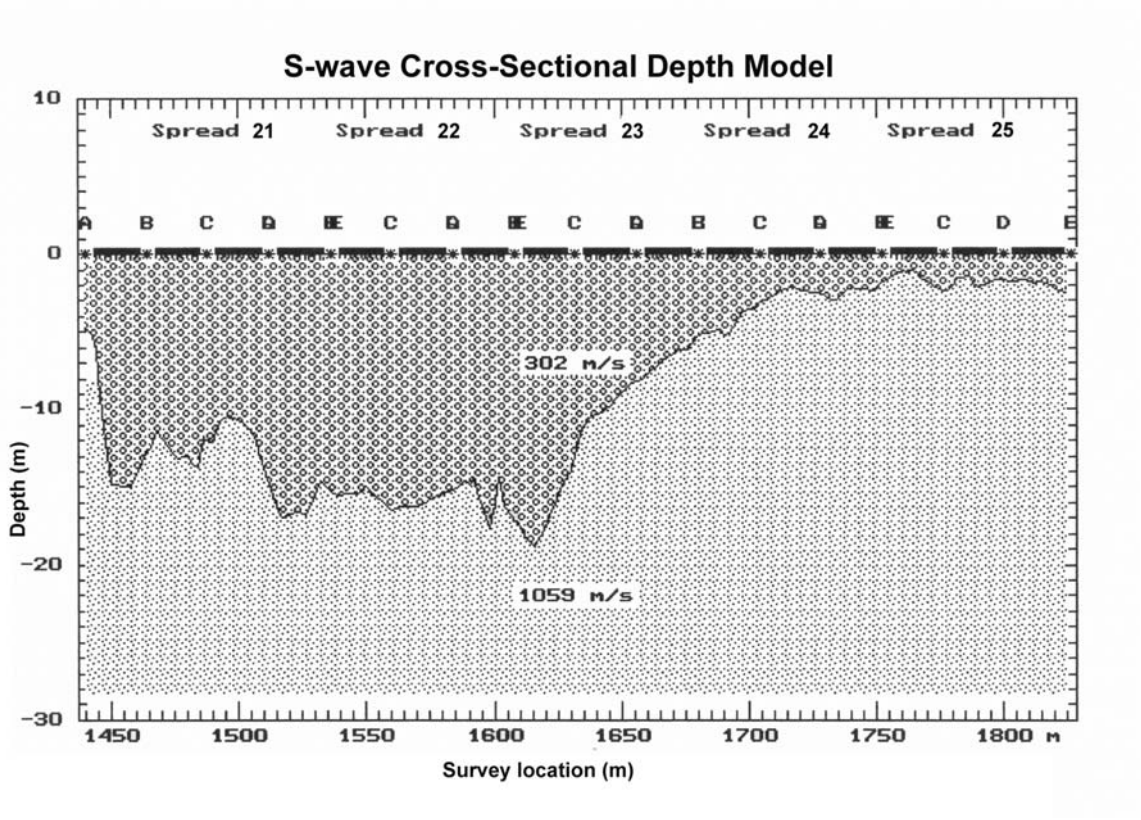
S-wave Cross-Sectional Depth Model
Spread 21
Spread 22
Spread 23
Spread 24
Spread 25
A B C D E C D E C D B C D E C D E
10
0
-10
-20
-30
Depth (m)
302 m/s
1059 m/s
1450
1500
1550
1600
1650
1700
1750
1800 m
Survey location (m)

Appendix J: 2D Resistivity Models

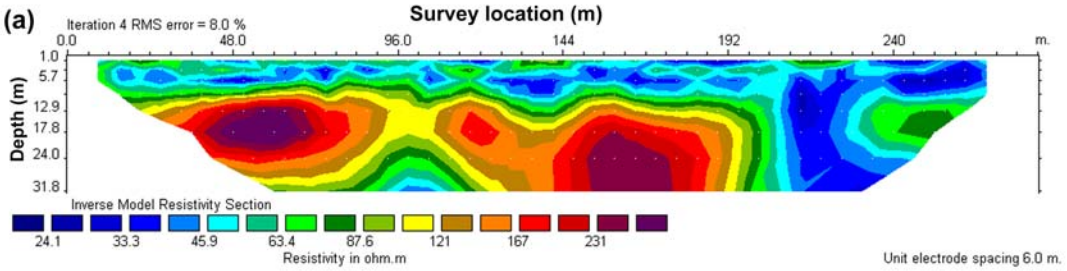
(a)
Iteration 4 RMS error = 8.0 %
Survey location (m)
0.0
48.0
96.0
144
192
240
m.
Depth (m)
1.0
5.7
12.9
17.8
24.0
31.8
Inverse Model Resistivity Section
24.1
33.3
45.9
63.4
87.6
121
167
231
Resistivity in ohm.m
Unit electrode spacing 6.0 m.

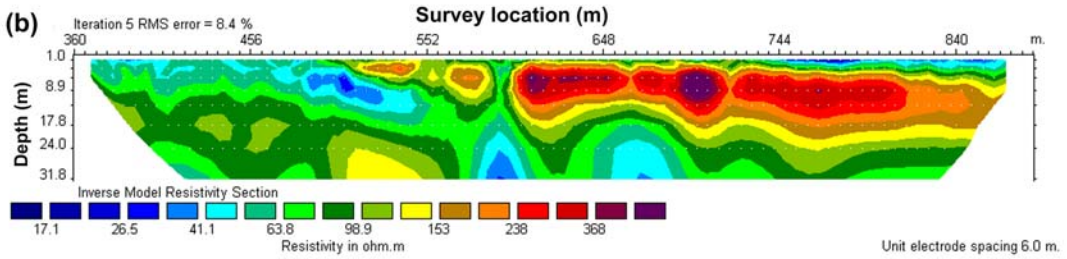
(b)
Iteration 5 RMS error = 8.4 %
Survey location (m)
360
456
552
648
744
840
m.
Depth (m)
1.0
8.9
17.8
24.0
31.8
Inverse Model Resistivity Section
17.1
26.5
41.1
63.8
98.9
153
238
368
Resistivity in ohm.m
Unit electrode spacing 6.0 m.

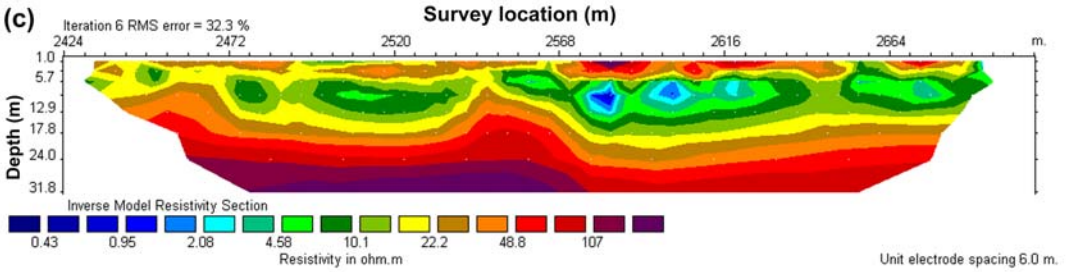
(c)
Iteration 6 RMS error = 32.3 %
Survey location (m)
2424
2472
2520
2568
2616
2664
m.
Depth (m)
1.0
5.7
12.9
17.8
24.0
31.8
Inverse Model Resistivity Section
0.43
0.95
2.08
4.58
10.1
22.2
48.8
107
Resistivity in ohm.m
Unit electrode spacing 6.0 m.

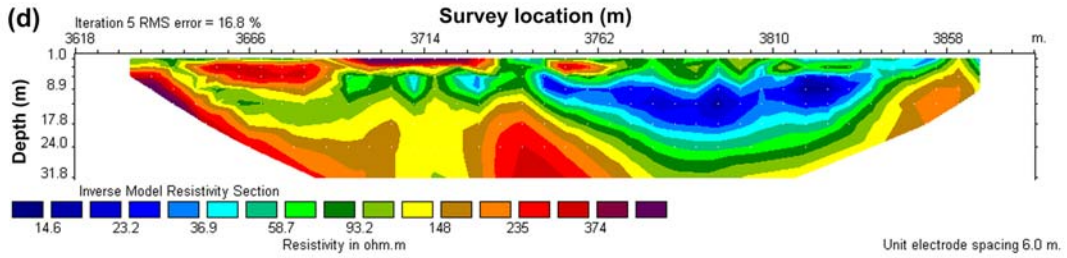
(d)
Iteration 5 RMS error = 16.8 %
Survey location (m)
3618
3666
3714
3762
3810
3858
m.
Depth (m)
1.0
8.9
17.8
24.0
31.8
Inverse Model Resistivity Section
14.6
23.2
36.9
58.7
93.2
148
235
374
Resistivity in ohm.m
Unit electrode spacing 6.0 m.

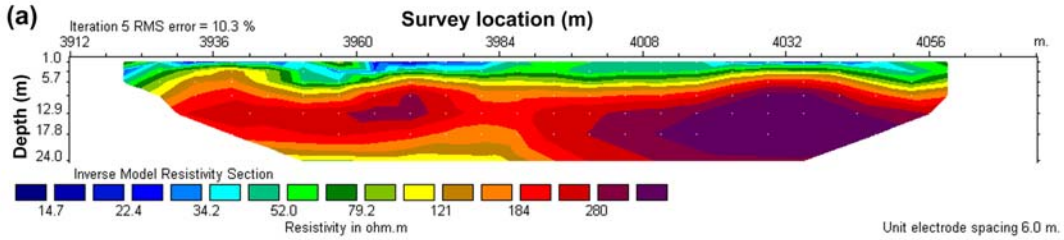
(a)
Iteration 5 RMS error = 10.3 %
Survey location (m)
3912
3936
3960
3984
4008
4032
4056
m.
Depth (m)
1.0
5.7
12.9
17.8
24.0
Inverse Model Resistivity Section
14.7
22.4
34.2
52.0
79.2
121
184
280
Resistivity in ohm.m
Unit electrode spacing 6.0 m.

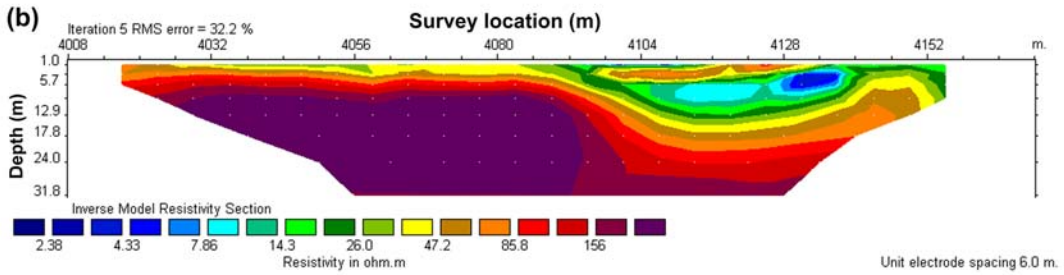
(b)
Iteration 5 RMS error = 32.2 %
Survey location (m)
4008
4032
4056
4080
4104
4128
4152
m.
Depth (m)
1.0
5.7
12.9
17.8
24.0
31.8
Inverse Model Resistivity Section
2.38
4.33
7.86
14.3
26.0
47.2
85.8
156
Resistivity in ohm.m
Unit electrode spacing 6.0 m.

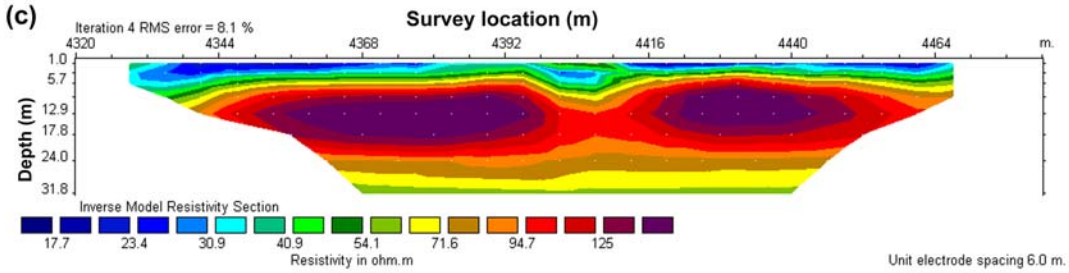
(c)
Iteration 4 RMS error = 8.1 %
Survey location (m)
4320
4344
4368
4392
4416
4440
4464
m.
Depth (m)
1.0
5.7
12.9
17.8
24.0
31.8
Inverse Model Resistivity Section
17.7
23.4
30.9
40.9
54.1
71.6
94.7
125
Resistivity in ohm.m
Unit electrode spacing 6.0 m.